



### 저작자표시-비영리-동일조건변경허락 2.0 대한민국

이용자는 아래의 조건을 따르는 경우에 한하여 자유롭게

- 이 저작물을 복제, 배포, 전송, 전시, 공연 및 방송할 수 있습니다.
- 이차적 저작물을 작성할 수 있습니다.

다음과 같은 조건을 따라야 합니다:



저작자표시. 귀하는 원저작자를 표시하여야 합니다.



비영리. 귀하는 이 저작물을 영리 목적으로 이용할 수 없습니다.



동일조건변경허락. 귀하가 이 저작물을 개작, 변형 또는 가공했을 경우에는, 이 저작물과 동일한 이용허락조건하에서만 배포할 수 있습니다.

- 귀하는, 이 저작물의 재이용이나 배포의 경우, 이 저작물에 적용된 이용허락조건을 명확하게 나타내어야 합니다.
- 저작권자로부터 별도의 허가를 받으면 이러한 조건들은 적용되지 않습니다.

저작권법에 따른 이용자의 권리는 위의 내용에 의하여 영향을 받지 않습니다.

이것은 [이용허락규약\(Legal Code\)](#)을 이해하기 쉽게 요약한 것입니다.

[Disclaimer](#)

**Thesis for a Ph. D. Degree**

**Retrieving Aerosol Optical Thickness  
and Altitude of Asian Dust  
from AIRS Measurements**

AIRS 관측자료를 이용한  
황사의 광학두께 및 고도 산출

**February 2013**

**School of Earth and Environmental Sciences  
Graduate School  
Seoul National University**

**Hyojin Han**

# Retrieving Aerosol Optical Thickness and Altitude of Asian Dust from AIRS Measurements

AIRS 관측자료를 이용한  
황사의 광학 두께 및 고도 산출

지도교수 손 병 주

이 논문을 이학박사 학위논문으로 제출함  
2012년 10월

서울대학교 대학원  
지구환경과학부  
한 효 진

한효진의 이학박사 학위논문을 인준함  
2012년 12월

위원장	_____	(인)
부위원장	_____	(인)
위원	_____	(인)
위원	_____	(인)
위원	_____	(인)

**Retrieving Aerosol Optical Thickness  
and Altitude of Asian Dust  
from AIRS Measurements**

**By  
Hyojin Han**

**A Dissertation submitted to the Faculty of the  
Graduate School of the Seoul National University  
in partial fulfillment of the requirements  
for the Degree of Doctor of Philosophy**

**Degree Awarded:  
February 2013**

**Advisory committee:**

**Professor Rokjin J. Park, Chair  
Professor Byung-Ju Sohn, Advisor  
Professor Kwang-Mog Lee  
Doctor Hung-Lung Huang  
Doctor Do-Hyeong Kim**

이학박사학위논문

**AIRS 관측자료를 이용한  
황사의 광학두께 및 고도 산출**

Retrieving Aerosol Optical Thickness and  
Altitude of Asian Dust  
from AIRS Measurements

2013년 2월

서울대학교 대학원  
지구환경과학부  
한효진

## Abstract

Aerosol optical thickness (AOT) and effective height ( $z_{\text{dust}}$ ) of Asian dust were retrieved from infrared (IR) hyperspectral measurements. In order to examine how accurately dust properties can be retrieved from satellite-borne IR hyperspectral measurements, we first employed a statistical artificial neural network (ANN) method to retrieve the pixel-level AOT and  $z_{\text{dust}}$  for Asian dust. This was done by relating the Atmospheric Infrared Sounder (AIRS) brightness temperatures for 234 channels, surface elevation, and relative air mass to target parameters (here, AOT and  $z_{\text{dust}}$ ) through an ANN model. Target data collocated with AIRS brightness temperature (TBs) were from the Moderate Resolution Imaging Spectroradiometer (MODIS)-derived AOT and the Cloud Aerosol Lidar Infrared Pathfinder Satellite Observation (CALIPSO)-derived  $z_{\text{dust}}$ . Results show a correlation coefficient of 0.84 and mean bias of 0.03 for AOT, and a correlation coefficient of 0.79 and mean bias of -0.01 km for  $z_{\text{dust}}$ , suggesting that dust retrievals from IR hyperspectral measurements are comparable to MODIS-derived AOTs and CALIPSO-estimated dust heights.

The potential applicability of IR hyperspectral measurements to dust monitoring, demonstrated and substantiated by the ANN results, brings in a possibility of developing a physical retrieval algorithm for Asian dust. In doing so, the fast Radiative Transfer for Television Infrared Observation Satellite (TIROS) Operational Vertical Sounder (RTTOV) model (version 9.3) was implemented with an updated dust-size distribution and surface emissivity for better simulating the dust effect on top of atmosphere radiances. Also included

were the refractive indices giving better Asian-dust simulation results, in comparison to AIRS-measured TBs. Adopting a one-dimensional variational (1DVAR) approach embedded with the implemented RTTOV model, a physical model has been developed for retrievals of Asian dust AOT and effective height. Results show that AIRS-derived IR AOTs are well correlated with the MODIS visible (VIS) AOTs, with correlation coefficients of 0.77–0.96. Effective dust heights also agree well with dust heights derived from CALIPSO backscattered reflectivity profiles. In conclusion, AOT and the effective height of Asian dust can be retrieved from IR hyperspectral measurements with accuracies comparable to MODIS AOT and CALIPSO dust height. Since those parameters can be retrieved on a two-dimensional basis in both day and night, IR hyperspectral sounder measurements can significantly improve dust forecasting through dust monitoring and data assimilation.

**Keyword:** Asian dust, IR hyperspectral, AIRS, MODIS, CALIPSO, Aerosol optical thick, Dust height, Artificial neural network, Radiative transfer model, RTTOVO, Physical retrieval algorithm

**Student Number:** 2004-20598

# Table of Contents

<b>Abstract</b> .....	<b>i</b>
<b>Table of Contents</b> .....	<b>iii</b>
<b>List of Figures</b> .....	<b>vi</b>
<b>List of Tables</b> .....	<b>xiv</b>
<b>1. Introduction</b> .....	<b>1</b>
<b>2. Review of previous IR-based dust retrievals</b> .....	<b>5</b>
<b>3. IR hyperspectral measurements</b> .....	<b>16</b>
<b>4. Examining dust signal in the AIRS hyperspectral measurements</b> .....	<b>24</b>
<b>4.1 Sensitivity of IR TB to dust amount and height</b> .....	<b>24</b>
<b>4.2 Construction of training data sets for ANN model</b> .....	<b>28</b>
<b>4.2.1 Detecting FOVS containing dust</b> .....	<b>32</b>
<b>4.2.2 Construction of collocated AIRS vs. MODIS data</b> .....	<b>35</b>
<b>4.2.3 Construction of collocated CALIPSO vs. AIRS data</b> .....	<b>36</b>
<b>4.3 ANN model development</b> .....	<b>39</b>
<b>4.4 Validation</b> .....	<b>46</b>

4.5 Case studies .....	49
4.5.1 March 1–2, 2008 case .....	50
4.5.2 April 17, 2009 case .....	55
4.5.3 April 23, 2009 case .....	59
<b>5. Simulation of dust impact on AIRS spectrum .....</b>	<b>63</b>
<b>5.1 Dust modeling for radiative transfer calculation .....</b>	<b>64</b>
<b>5.2. Radiative transfer modeling .....</b>	<b>65</b>
5.2.1 Radiative transfer model .....	66
5.2.2 Dust modeling and improved Lorentz-Mie calculation .....	67
5.2.3 Surface emissivity .....	75
<b>5.3 AIRS spectral radiance simulations .....</b>	<b>76</b>
<b>5.4. Comparisons with observations .....</b>	<b>77</b>
<b>6. Dust retrieval using a physical method .....</b>	<b>90</b>
6.1 Retrieval algorithm .....	90
6.2 Channel selection .....	92
6.3 Meteorological model .....	95

<b>6.4 Results</b> .....	97
<b>6.4.1 February 29, 2008 case</b> .....	97
<b>6.4.2 March 1, 2008 case</b> .....	99
<b>6.4.3 May 11, 2011 case</b> .....	102
<b>6.4.4 April 23, 2009 case</b> .....	104
<b>6.4.5 April 24, 2009 case</b> .....	107
<b>6.4.6 Evolutionary feature of April 23–24, 2009 dust event</b> .....	112
<b>6.4.7 April 23 and 24, 2009 cases with initial guess fields from ANN retrievals</b> .....	116
<b>6.4.8 Statistical summary</b> .....	124
<b>7. Summary and conclusions</b> .....	126
<b>References</b> .....	132
<b>국문초록</b> .....	145

## List of Figures

- Figure 1. The particle size dependence of the thermal IR emissivity spectrum of pure quartz for 75–250  $\mu\text{m}$  (solid line) and 0–75  $\mu\text{m}$  (dashed line) particle size ranges. The larger particle size is similar to fine beach sand. The MODIS 8.6, 11, and 12  $\mu\text{m}$  bands are shown in vertical bars. [Wald et al., 1998]..... 11
- Figure 2. Simulation of the trispectral diagram for condition representative of dust overlying a desert with different spectral emissivities. [Ackerman, 1997] ..... 12
- Figure 3. Schematic diagram showing how two band thermal IR transmission through meteorological and dust clouds differs. [Gu et al., 2003]..... 13
- Figure 4. Combined trispectral diagram of BTDs for ‘heavy dust’ pixels for all considered regions. Numbers from 1 to 7 indicate the regions cover dust outbreaks originating from all main dust sources of the world (1: Mauritania, Morocco, Algeria, and Bodele Depression; 2: Libyan Desert; 3: Nubian Desert; 4: Iranian Desert; 5: Thar Desert; 6: Gobi and Taklimakan regions; 7: dust from Australian Desert). [Darmenov and Sokolik 2005] ..... 14
- Figure 5. TBs observed by the high-resolution sensor for clear sky (blue line) and for light and moderate dust loadings. Red, brown, and green curves are for Mixtures 1, 2 and 3, respectively (Mixture 1: 50% quartz and 50% clays; Mixture 2: 20% quartz and 80% clays; and Mixture 3: 80% quartz and 20%

clays). [Sokolik, 2002].....	15
Figure 6. AIRS scan geometry and the relative alignment of the AIRS/AMSU/HSB footprints. [Aumann et al., 2003] .....	21
Figure 7. AIRS Noise Equivalent Temperature Difference (NE $\Delta$ T) at 250 K measured in orbit.....	22
Figure 8. Simulated AIRS upwelling spectrum in TB. The simulation is performed using ‘Mid-latitude summer atmospheric profile’ and constant surface emissivity of 1.0. ....	23
Figure 9. (a) Simulated IR TBs with various AOT and (b) differences between TBs simulated under clear-sky and mineral dust condition.....	26
Figure 10. Same as Figure 9 except for various dust heights. ....	27
Figure 11. Selected AIRS 234 channels used for the ANN model development in this study. Dots in green, red, yellow, and blue represent selected channels over CO <sub>2</sub> , WIN, O <sub>3</sub> , and WV bands, respectively.....	31
Figure 12. Imaginary part (absorptive component) of ice and dust refractive indices. The Volz Saharan dust data is used for this plot. The circles show the locations of the AIRS channels used for the DDA. Note that dust has a peak absorption at about 10 $\mu$ m (1000 cm <sup>-1</sup> ) while ice has a peak absorption at longer wavelengths (about 12 $\mu$ m or 800 cm <sup>-1</sup> ). This spectral separation can allow IR instruments to discriminate between the presence of ice or	

dust in a FOV. Ozone also has peak absorption in the 1000–1080 $\text{cm}^{-1}$ region. [DeSouza-Machado et al., 2010] .....	34
Figure 13. Structure of the ANN model showing 236 inputs (234 AIRS TBs, topography ( $z_{\text{sfc}}$ ), and relative airmass of the sensor ( $1/\mu$ )), a single hidden layer with 5 neurons, and the target outputs (AOT and dust height ( $z_{\text{dust}}$ )).	43
Figure 14. Correlation coefficients and RMSEs (a) between AIRS-derived and MODIS-estimated AOTs, and (b) between AIRS-derived and CALIPO-measured dust height. Solid and dashed lines are for correlation and RMSE, respectively. WIN, $\text{CO}_2$ , WV, and $\text{O}_3$ on the abscissa represent inputs of AIRS TBs at window, $\text{CO}_2$ , water vapor, $\text{O}_3$ bands, respectively. And $z_{\text{sfc}}$ : land surface topography, $1/\mu$ : relative airmass from the surface to the sensor, $\text{BTD}_{11-12}$ : brightness temperature difference between 11 $\mu\text{m}$ and 12 $\mu\text{m}$ . Inputs are arranged in a cumulative fashion. ....	44
Figure 15. Two dimensional histogram of (a) MODIS-derived vs. ANN-retrieved AOTs for February–May 2008, and (b) CALIPSO-derived $z_{\text{dust}}$ vs. ANN-retrieved $z_{\text{dust}}$ for January–December 2009 in a 0.1 bin size. ....	48
Figure 16. (a)–(b) MODIS true color images, (c)–(e) AOTs retrieved from AIRS measurements using the ANN model, and (f)–(g) MODIS-derived AOTs during 1 – 2 March 2008.....	53
Figure 17. (a) Geographical locations of the two skyradiometer sites (Xinglong and Gwangju) of AERONET. Time series of AOTs observed by	

skyradiometers (a) at Xinglong on March 1, 2008 and (b) at Gwangju on March 2, 2008 are shown as closed circle. The AIRS-estimated AOTs for each site are plotted with red cross marks in (b) and (c). .....	54
Figure 18. (a) MODIS true color image, (b) AOT retrieved from AIRS measurements, and (c) MODIS-derived AOT on April 17, 2009 over the Taklimakan Desert area.....	57
Figure 19. (a) Two-dimensional distributions of dust heights retrieved from AIRS measurements, and (b) vertical view of CALIOP-measured total attenuated backscatter at 532 nm on April 17, 2009 over the Taklimaken Desert area, along the CALIPSO track [red line in (a)]. The backscatter in unit of $\text{km}^{-1} \text{sr}^{-1}$ are multiplied by 1000, and values smaller than $5.0 \times 10^{-3} \text{km}^{-1} \text{sr}^{-1}$ are masked out in (b). .....	58
Figure 20. Same as Figure 18, except for the dust outbreak on April 23, 2009 over the Gobi Desert. ....	61
Figure 21. Same as Figure 19, except for the dust outbreak on April 23, 2009 over the Gobi Desert. ....	62
Figure 22. (a) Size distributions of Asian dust retrieved from sky radiometer measurements at Dunhuang, China (thin solid lines), and the mean size distribution (white dashed line). (b) Mean size distribution from the sky radiometer measurements (thick dashed line), three modes for mineral dust components from OPAC (nucleus mode: Nuc, accumulation mode: Acc,	

and coarse mode: Coa), and the best fit for the mean size distribution (thick solid line). .....	72
Figure 23. (a) Real and (b) imaginary parts of the refractive indices for OPAC mineral aerosol component (solid line), Volz dust-like aerosol (dashed-dot line), and HITRAN quartz (dashed line). The vertical dashed lines depict the spectral locations of four channels (ch770; 11 $\mu\text{m}$ , ch 565; 12 $\mu\text{m}$ , ch 1247; 8.9 $\mu\text{m}$ , ch 2330; 3.8 $\mu\text{m}$ ) used for the BTD calculation. ....	73
Figure 24. Extinction coefficients for the mineral aerosol component of OPAC (solid line), dust-like aerosol of Volz (dashed-dot line), and HITRAN quartz (dashed line) over the IR region. The coefficients are calculated with the given Asian dust size distribution of Figure 22. ....	74
Figure 25. Scatter plots of simulated and measured AIRS $T_{\text{BS}}$ for (a) 11 $\mu\text{m}$ (ch 770), (b) 12 $\mu\text{m}$ (ch 565), (c) 8.9 $\mu\text{m}$ (ch 1247), and (d) 3.8 $\mu\text{m}$ (ch 2330) with associated statistics. The $T_{\text{BS}}$ are simulated with OPAC mineral aerosol refractive index and with OPAC mineral coarse mode size distribution. Dashed lines represent best fit regression lines. ....	85
Figure 26. Scatter plots for simulated and measured (a) $\text{BTD}_{11-12}$ , (b) $\text{BTD}_{8.9-11}$ , and (c) $\text{BTD}_{3.8-11}$ . The $T_{\text{BS}}$ are simulated with OPAC mineral aerosol refractive index and with OPAC mineral coarse mode size distribution. The default land surface emissivity of 0.98 is used. ....	86
Figure 27. As Figure 26, except for the use of UW/CIMSS surface emissivity	

data.....	86
Figure 28. Mean bias (simulated $T_B$ minus measured $T_B$ ) for dust with CALIPSO AOT532 > 0.5 for IR spectral bands (a) 750–1150 $\text{cm}^{-1}$ and (b) 2400–2700 $\text{cm}^{-1}$ . The $T_B$ s are simulated with three refractive indices (OPAC: OPAC mineral aerosol component; Volz: Volz dust-like; HITRAN: quartz from HITRAN database) and with different dust-size distributions (AD: Asian dust size distribution; TR: mineral-transported in OPAC; CO: mineral coarse mode in OPAC). Surface emissivities over the land are specified by UW/CIMSS surface emissivity data. The vertical red lines indicate the four channels (ch 770; 11 $\mu\text{m}$ , ch 565; 12 $\mu\text{m}$ , ch 1247; 8.9 $\mu\text{m}$ , ch 2330; 3.8 $\mu\text{m}$ ) used for the BTD comparison. ....	87
Figure 29. As Figure 26, except for the use of the Volz dust-like refractive index, the given Asian dust size distribution, and the UW/CIMSS surface emissivity data. ....	89
Figure 30. An example of skin temperature distribution obtained from RDAPS dataset showing the model domain. ....	96
Figure 31. (a) MODIS true color image, (b) Scatterplot for AIRS IR AOT and MODIS VIS AOT, (c) IR AOT retrieved from AIRS measurements, and (d) MODIS-derived AOT on February 29, 2008. ....	98
Figure 32. (a) MODIS true color image, (b) IR AOT retrieved from AIRS measurements, and (c) MODIS-derived AOT on March 1, 2008. ....	100

Figure 33. Scatterplots for AIRS IR AOT and MODIS VIS AOT over (a) land and (b) ocean on March 1, 2008. ....	101
Figure 34. (a) MODIS true color image, (b) Scatterplot for AIRS IR AOT and MODIS VIS AOT, (c) IR AOT retrieved from AIRS measurements, and (d) MODIS-derived AOT on May 11, 2011. ....	103
Figure 35. (a) MODIS true color image, (b) scatterplot for AIRS IR AOT and MODIS VIS AOT, (c) IR AOT retrieved from AIRS measurements, and (d) MODIS-derived AOT on April 23, 2009. ....	105
Figure 36. (a) Two-dimensional distributions of dust heights retrieved from AIRS measurements, and (b) vertical view of CALIOP-measured total attenuated backscatter at 532 nm on April 23, 2009 over the Gobi Desert area, along the CALIPSO track [red line in (a)]. The backscatter in units of $\text{km}^{-1} \text{sr}^{-1}$ is multiplied by 1000, and values smaller than $5.0 \times 10^{-3} \text{ km}^{-1} \text{sr}^{-1}$ are masked out in (b). ....	106
Figure 37. (a) MODIS true color image, (b) IR AOT retrieved from AIRS measurements, and (c) MODIS-derived AOT on April 24, 2009. ....	109
Figure 38. Scatterplots for AIRS IR AOT and MODIS VIS AOT over (a) land and (b) ocean on April 24, 2009. ....	110
Figure 39(a) Two-dimensional distributions of effective dust heights retrieved from AIRS measurements and (b) vertical view of CALIOP-measured total attenuated backscatter at 532 nm along the CALIPSO track [red line in (a)]	

on April 24, 2009. ....	111
Figure 40. (a)–(b) MODIS true color images, (c)–(e) AOTs retrieved from AIRS measurements, and (f)–(g) MODIS-derived AOTs during April 23–24, 2008. ....	114
Figure 41. (a)–(b) MODIS true color images, (c)–(e) $z_{\text{dust}}$ retrieved from AIRS measurements, and (f)–(h) vertical view of CALIOP-measured total attenuated backscatter at 532 nm during April 23–24, 2008, along the CALIPSO track [red line in (c)–(e)]. The backscatter in unit of $\text{km}^{-1} \text{sr}^{-1}$ are multiplied by 1000, and values smaller than $5.0 \times 10^{-3} \text{km}^{-1} \text{sr}^{-1}$ are masked out in (f)–(h).....	115
Figure 42. Same as Figure 35, except for use of the ANN-retrieved initial-guess field. ....	119
Figure 43. Same as Figure 36, except for use of the ANN-retrieved initial-guess field. ....	120
Figure 44. Same as Figure 37, except for use of the ANN-retrieved initial-guess field. ....	121
Figure 45. Same as Figure 38, except for use of the ANN-retrieved initial-guess field. ....	122
Figure 46. Same as Figure 39, except for use of the ANN-retrieved initial-guess field. ....	123

## List of Tables

Table 1. AIRS Dust Flag Detection <sup>a</sup> .....	38
Table 2. Inputs used for the Artificial Neural Network models.....	45
Table 3. RMSEs of the simulated versus measured $T_{BS}$ for AIRS-CALIPSO dust pixels if $CALIPSO\ AOT_{532} > 0.5$ (total 2350 cases). $T_{BS}$ are simulated with three refractive indices (OPAC: OPAC mineral aerosol component; Volz: Volz dust-like; HITRAN: quartz from HITRAN database) and with different dust size distributions (AD: Asian dust size distribution; TR: mineral-transported in OPAC; CO: mineral coarse mode in OPAC). .....	88
Table 4. AIRS selected channels number, wavenumber, wavelength, and surface transmittance simulated using the tropical atmospheric profile in RTTOV 9.3.....	94
Table 5. Correlation coefficient (R), linear regression slopes and offsets for AIRS IR AOT and collocated MODIS AOT. ....	115

## **1. Introduction**

There has been growing concern about mineral dusts originating in China and Mongolia (referred to as Asian dusts) because such dusts are transported to densely populated areas in East Asia and can have a significant negative influence on human activity. Occurrences of dust events have become more frequent in Korea and Japan in recent years [Kurosaki and Mikami, 2003; Kim, 2008], likely associated with an expansion of the arid area over eastern Mongolia [Park and Sohn, 2010; Lee and Sohn, 2011]. In order to reduce expected negative impacts on health and socioeconomic factors using an early warning system, accurate monitoring of the evolution of Asian dust after its outbreak is essential.

In the recent decades, large-scale experiments and surface networks for aerosol, cloud, and radiation measurements have been built in Asia [Holben et al., 2001; Ramanathan and Crutzen, 2003; D.-H. Kim et al., 2004; Mikami et al., 2006; Z. Li et al., 2007; Nakajima et al., 2007] to understand the optical properties of various aerosols, including Asian dust. Although in situ measurements of Asian dust help us understand its climate implications and possible impact on human beings, limitations caused by point measurements keep us from applying them to dust monitoring and forecasting. Consequently, a more effective observational instrument is indispensable for Asian dust monitoring over wider areas, including uninhabited regions and oceans.

While in situ ground measurements represent limited areas surrounding observation sites, satellite observations certainly improve such limitations by

providing an efficient tool for monitoring evolutionary features of dust: they allow extensive areal coverage and the ability to quantitatively measure dust's optical properties. With the advent of satellite technology, dust monitoring relies more on satellite measurements. Techniques utilizing ultraviolet (UV) and visible (VIS) measurements have been successfully developed [e.g., Torres et al., 1998; Wald et al., 1998; Hsu et al., 2000; Sinyuk et al., 2003; Hsu et al., 2004; Remer et al., 2005], albeit only for daytime retrieval. Increasing daytime temporal coverage seems to improve dust-monitoring performance, and it would be beneficial if nighttime dust estimates were available. However, with no UV/VIS light available at night, an increase in temporal/spatial coverage, especially during nighttime, should rely on passive infrared (IR) or active light sources.

Some successes in detecting dust from satellite-based IR measurements have been reported [Ackerman, 1989; Ackerman, 1997; Legrand et al., 2001; Sokolik, 2002; J. Li et al., 2007]. For instance, the brightness temperature (TB) difference between thermal split window channels has long been used as an index representing the magnitude of dust loading [Ackerman, 1997; Legrand et al., 2001; Darmenov and Sokolik, 2005; Brindley and Russel, 2006; Merchant et al., 2006], although its accuracy has been questioned [e.g., Sohn et al., 2013]. Furthermore, quantitative physical parameters could be more beneficial than an ambiguous dust index if measurements are possible during the nighttime.

The use of hyperspectral IR measurements may provide such retrieval capability, since thousands of channels across the IR spectrum implicitly carry

information about IR emissions from surface and atmospheric gases and about radiative interactions with dust particles. Indeed, recent studies have demonstrated that high-spectral-resolution IR sounders are able to retrieve dust height and IR aerosol optical thickness (AOT) [Pierangelo et al., 2004; DeSouza-Machado et al., 2010; Peyridieu et al., 2010; Yao et al., 2012]. Despite the successful use of hyperspectral IR measurements to retrieve dust properties, previous efforts have been limited to monthly retrieval over oceans [Pierangelo et al., 2004; Peyridieu et al., 2010] or to case studies [DeSouza-Machado et al., 2010; Yao et al., 2012]. Thus, there is a need for more in-depth studies of general retrieval accuracy and of the possibility of using this information for dust monitoring or forecasting.

Recognizing the potential use of hyperspectral IR measurements for retrieving dust amount and height regardless of the time of day, this study focuses on retrieving the AOT and vertical height of Asian dust from the IR hyperspectral measurements. To meet these objectives, we first examine the degree of accuracy that can be achieved in AOT and dust height retrievals from hyperspectral IR measurements, by developing a statistical algorithm with the use of remotely sensed Atmospheric Infrared Sounder (AIRS) measurements. After examining the retrieval capability of IR hyperspectral measurements, we attempt to retrieve AOTs and dust heights from AIRS sounder measurements using a one-dimensional variational (1DVAR) method. Considering that the physical retrieval of aerosol properties from satellite measurements requires an understanding of the underlying radiative transfer, a better description of dust

optical properties and accurate radiative transfer modeling are prerequisite for aerosol retrieval. Accordingly, we simulate dust-affected IR spectra to understand the impact of various optical and physical properties for Asian dust and surface emissivity, and then offer the dust properties showing the best agreement with observations by comparing them to the AIRS measurements. Finally, based on the dust modeling, AOTs at thermal IR wavelengths and dust heights are derived from the physical retrieval algorithm. To validate the retrievals, the AIRS-derived AOTs are compared with those from the Moderate Resolution Imaging Spectroradiometer (MODIS) measurements, and the retrieved effective dust heights are compared against the extinction backscatter profiles obtained from the Cloud-Aerosol Lidar with Orthogonal Polarization (CALIOP) measurements. If successful, it is certain that temporal coverage of the dust obtained, as well as its height for both day and night, will provide valuable information for better monitoring the evolutionary features of dust aerosols.

## 2. Review of previous IR-based dust retrievals

Previous studies have demonstrated that dust aerosols induces detectable radiation signature over an IR spectrum by satellite sensors, supporting the capability of the IR spectrum to retrieve mineral dust properties from space. Upwelling thermal IR radiation emitted from the surface is selectively scattered and/or absorbed by airborne particles, and the total attenuation depends on optical property and vertical distribution of suspended particles in the atmospheric column. Some successes in detecting dust from IR observations were reported, based on a priori information on the optical properties of the dust. Here we review documented IR-based dust retrieval methods.

Ackerman [1997] has investigated the possible use of IR observations at around 8.5, 11, and 12  $\mu\text{m}$  for the dust detection. The detection algorithm is based on brightness temperature difference (BTD) among three channels, i.e., TB11-BT12 ( $\text{BTD}_{11-12}$ ) and BT8-BT11 ( $\text{BTD}_{8-11}$ ). Theoretical basis of the BTD approach is presented by simulated TBs of dust layer over a desert (Figure 1). The simulation shows that the dust optical depth initially increases with  $\text{BTD}_{11-12}$  and  $\text{BTD}_{8-11}$ . However, as the AOT continues to increase, the  $\text{BTD}_{11-12}$  and  $\text{BTD}_{8-11}$  decreases. Along with the simulation, BTDs observed by the High-Resolution Infrared Radiation Sounder/2 (HIRS/2) and the Advanced Very High Resolution Radiometer (AVHRR) for dust storms are also shown in Figure 2, indicating that the dust observations are in agreements with the simulations. Taking theoretical calculation and observation into account, it is demonstrated

that these three IR channels are useful for detecting dust aerosols.

Capability of IR spectrum for dust detection over high-albedo surfaces was presented by Wald et al. [1998], while the UV and VIS spectra are not available over bright surfaces such as desert or arid regions. IR emissivity spectra of quartz particles for two diameter ranges representing airborne dust (0–75  $\mu\text{m}$ ) and desert surface dust (75–250  $\mu\text{m}$ ) are shown in Figure 1. It is found that the emissivity spectra of quartz particles with different sizes can be significantly distinguished even though they have the same components, and thus IR spectra can be used to detect dust aerosols suspended over surface sand. Moreover, the difference between surface and airborne dust particles show a larger signal in the 8.5  $\mu\text{m}$  band rather than in the split window bands (11  $\mu\text{m}$  and 12  $\mu\text{m}$ ). Based on the particle size dependence of the thermal IR emissivity spectrum of silicate minerals, bispectral IR method for monitoring dust aerosols over desert was described using TBs observed by MODIS channels at 8.6 and 11  $\mu\text{m}$  [Wald et al., 1998].

The two channel BTD method using two split window channels has been commonly used to detect dust aerosols because of its availability from geostationary satellites. Silicate particles in the size range of 1–15  $\mu\text{m}$  in diameter cause a negative  $\text{BTD}_{11-12}$  with the longer wavelength channel recording a higher TB [Prata, 1989]. The mineral dust aerosols can be discriminated from clouds by using the dual IR bands observed by satellite, as ice or liquid water particles preferentially absorb radiances at longer wavelength (12  $\mu\text{m}$ ) than shorter wavelength (11  $\mu\text{m}$ ) while dust is the opposite

(Figure 3). The  $BTD_{11-12}$  dust detection method has been mainly used to obtain an ambiguous dust index rather than quantitative monitoring. The Korea Meteorological Administration (KMA) operationally detects dust pixels using the Dual Channel Difference (DCD) method, regarding a pixel whose  $BTD_{11-12}$  value less than -1.1 K as a dust loaded pixel.

The Infrared Difference Dust Index (IDDI) is an algorithm designed for dust detection in arid regions such as the Sahel and Sahara using a single Meteosat window channel (10.5–12.5  $\mu\text{m}$ ) measurements [Legrand et al., 2001]. It is based on the atmospheric response of dust. Under the dust condition, the thermal IR radiance measured at the satellite altitude is smaller than surface upwelling radiance due to the ground surface cooling in the shortwave region and the colder attenuation by absorption when passing through the dust layer than the emission from dust. Simply, the IDDI is defined as a depression of thermal IR radiance due to the dust layer in the atmosphere and is expressed as:

$$IDDI = TB - T_{sfc} \quad (1)$$

with  $TB$  and  $T_{sfc}$  being the measured TB from the satellite and surface temperature. This surface temperature is given through a maximum TB within 10 days with an assumption that the period is large enough to reasonably ensure the occurrence of at least one cloudless and dustless day for each pixel.

Dust index based on IR window radiometric measurements has been commonly used for dust monitoring because of its simple process of distinguishing dust pixels from others. Despite the simplicity, there exist various shortcomings. Most of dust detection methods provide an ambiguous

dust index, not physical quantitative parameters, and even their threshold values are influenced by environmental situations. Darmenov and Sokolik [2005] investigated a regional signature of dust aerosols in  $BTD_{11-12}$  and  $BTD_{8.5-11}$ . MODIS TBs at three IR channels centered at 8.55, 11.03, and 12.02  $\mu\text{m}$  observed over oceans were examined for the presence of dust plumes that originate from the main dust sources located in East and South Asia, Middle East, Northern Africa, and Australia. Figure 4 summarizes the mean BTM and standard deviations calculated for “heavy dust” cases along with clear sky cases. The BTM values under dust conditions show specific features depending on the particular region. The analysis demonstrated that automated discrimination between cloudy and dusty pixels based on the split window or the tri-spectral approach with fixed threshold(s) may not be reliable. The limitation of dust detection methods using IR measurements is mainly caused by the strong sensitivity of IR to surface and atmospheric conditions. Therefore, it is desirable to use advanced IR sensors that may be able to separate dust signals from environmental ones.

Based on radiative transfer simulation studies in high spectral resolution spectrum, Sokolik [2002] noted that dust causes a ‘negative slope’ over the  $820\text{--}920\text{ cm}^{-1}$  ( $10.87\text{--}12.2\ \mu\text{m}$ ) band, which separates the IR radiation effect of dust from that of clouds and atmospheric gases (Figure 5). The magnitude of the negative slope is not too sensitive to dust composition and thus can be used to retrieve the dust optical depth in this spectral region. In contrast, the region about  $1099\text{--}1220\text{ cm}^{-1}$  ( $8.2\text{--}9.1\ \mu\text{m}$ ) is quite sensitive to

dust composition and can provide important limits on dust mixtures. However, the radiative signatures of dust are apparent only over the high resolution spectra. Thus dust can be detected by narrowband satellite sensors, but for the quantitative characterization of dust properties higher spectral resolution is required. The potential of high spectral resolution remote sensing in providing compositional information is especially important since no other means of remote sensing from space are capable of providing such data [Sokolik, 2002].

Since recently available thousands channels over the IR spectrum provide enough spectral resolution to resolve the information on the environmental condition and dust distribution, it may be possible to retrieve quantitative parameters of dust aerosols. Recent studies have proved the retrieval capacity for the quantitative measures of dust aerosol parameters. Monthly mean dust AOT at 10  $\mu\text{m}$  and mean altitude are simultaneously retrieved over the tropics ( $30^{\circ}\text{S}$ – $30^{\circ}\text{N}$ ) from multi-year AIRS observations covering the period January 2003 to September 2009 [Peyridieu et al., 2010]. The method developed relies on the construction of look-up-tables computed for a large selection of atmospheric situations, the Thermodynamic Initial Guess Retrieval (TIGR). Retrieved AIRS AOTs were compared with MODIS VIS AOTs, and results showed a good agreement during the main dust season, in particular for the tropical North Atlantic and the north-western Indian Ocean. AIRS-retrieved dust layer mean altitudes were compared to the Cloud Aerosol Lidar Infrared Pathfinder Satellite Observation (CALIPSO) aerosol mean layer altitude for the period June 2006 to June 2009. Results for the region of the

north tropical Atlantic downwind of the Sahara showed a good agreement between two products.

With AIRS thermal IR radiance data and a fast IR scattering radiative transfer model (The AIRS Radiative Transfer Algorithm model, AIRS-RTA), DeSouza-Machado et al. [2010] physically retrieve the Sahara dust AOT and dust top height over both ocean and land. The algorithm uses atmospheric states initialized from the nearest  $0.25^\circ$  grid point in the European Centre for Medium-Range Weather Forecasts (ECMWF) 3-hour forecast data fields. The retrieved optical depths were compared against those retrieved using VIS and UV instruments on the A-Train, while dust layer heights are evaluated against lidar data. AOTs from AIRS correlate well with those from other instruments over ocean with a correlation coefficient greater than 0.9. AIRS-derived dust top heights compare favorably with CALIPSO data.

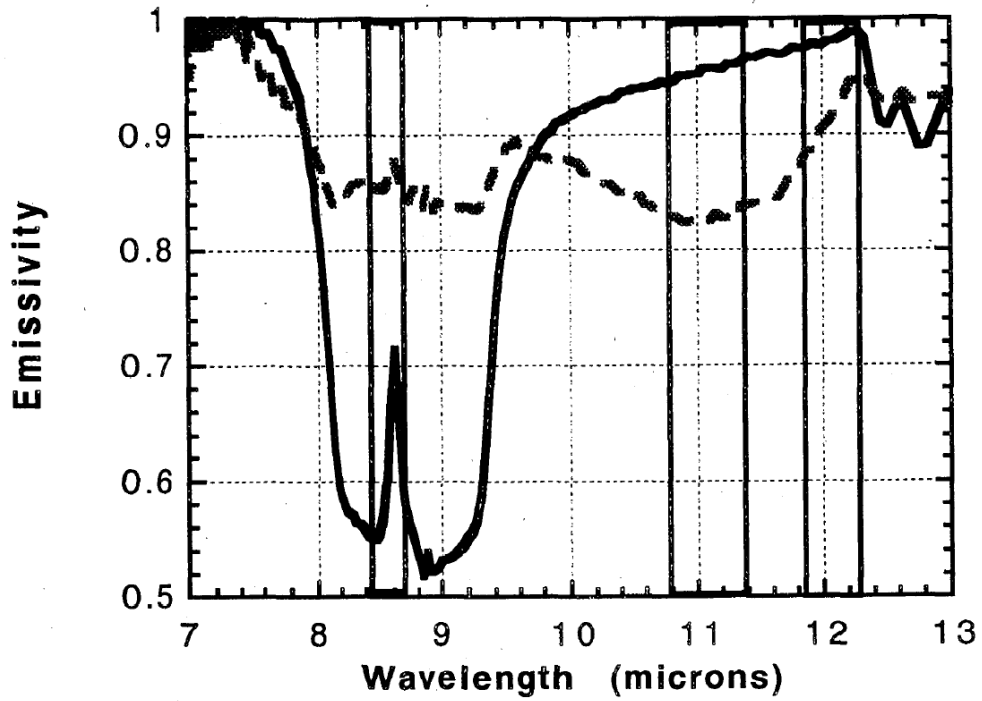


Figure 1. The particle size dependence of the thermal IR emissivity spectrum of pure quartz for 75–250  $\mu\text{m}$  (solid line) and 0–75  $\mu\text{m}$  (dashed line) particle size ranges. The larger particle size is similar to fine beach sand. The MODIS 8.6, 11, and 12  $\mu\text{m}$  bands are shown in vertical bars. [Wald et al., 1998]

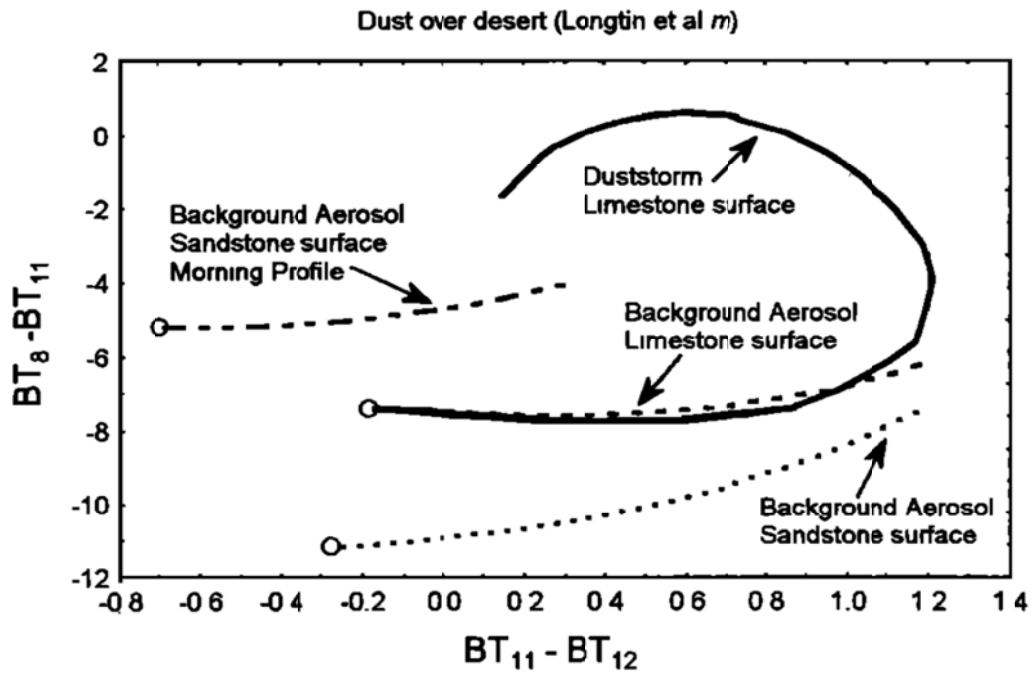


Figure 2. Simulation of the trispectral diagram for condition representative of dust overlying a desert with different spectral emissivities. [Ackerman, 1997]

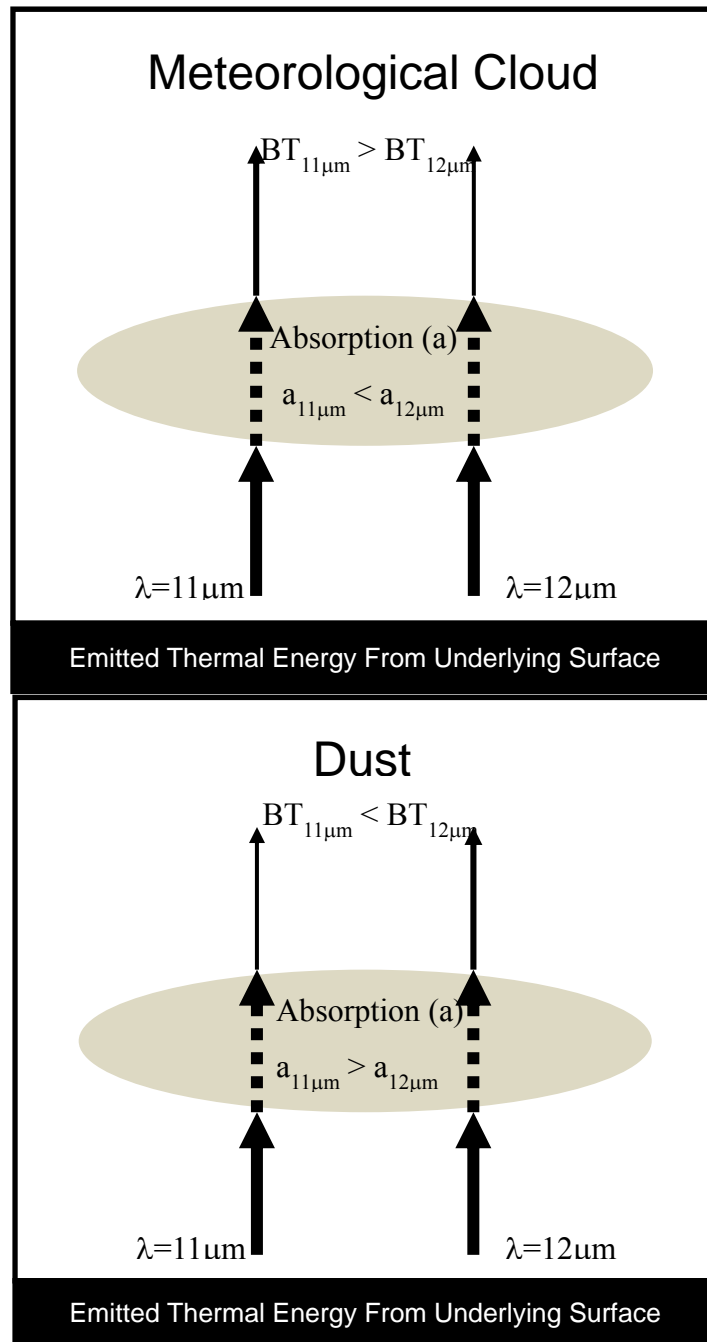


Figure 3. Schematic diagram showing how two band thermal IR transmission through meteorological and dust clouds differs. [Gu et al., 2003]

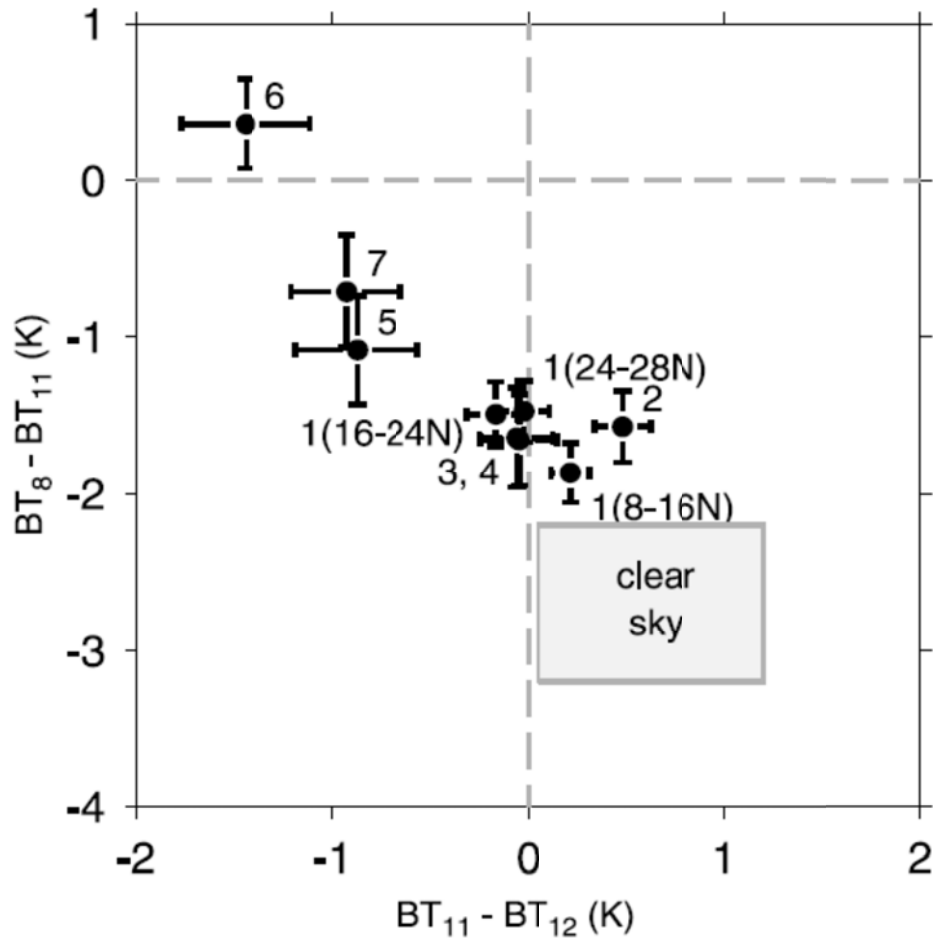


Figure 4. Combined trispectral diagram of BTDs for ‘heavy dust’ pixels for all considered regions. Numbers from 1 to 7 indicate the regions cover dust outbreaks originating from all main dust sources of the world (1: Mauritania, Morocco, Algeria, and Bodele Depression; 2: Libyan Desert; 3: Nubian Desert; 4: Iranian Desert; 5: Thar Desert; 6: Gobi and Taklimakan regions; 7: dust from Australian Desert). [Darmenov and Sokolik 2005]

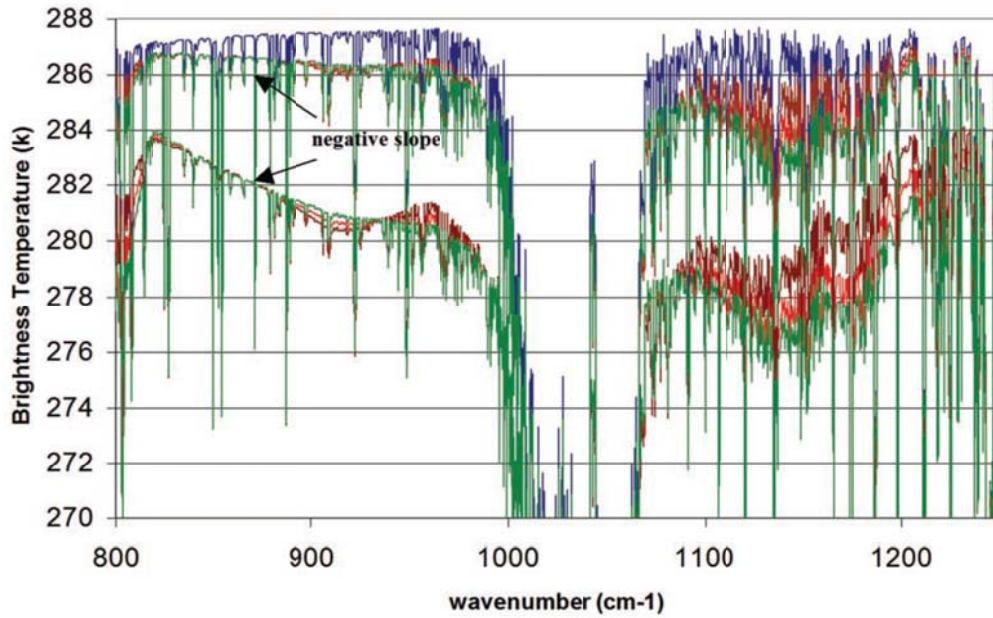


Figure 5. TBs observed by the high-resolution sensor for clear sky (blue line) and for light and moderate dust loadings. Red, brown, and green curves are for Mixtures 1, 2 and 3, respectively (Mixture 1: 50% quartz and 50% clays; Mixture 2: 20% quartz and 80% clays; and Mixture 3: 80% quartz and 20% clays). [Sokolik, 2002]

### **3. IR hyperspectral measurements**

Since we intend to improve the dust retrieval algorithm utilizing IR hyperspectral measurements with a quantification of the retrieval accuracy, we provide here detailed information on the AIRS hyperspectral measurements to be used in this study. Launched into Earth-orbit on May 4, 2002, AIRS is a first successful hyperspectral IR radiometer observing the Earth's surface and atmosphere [Aumann et al, 2003; Chahine et al, 2006]. AIRS is one of six instruments on board the Aqua satellite, a part of the National Aeronautics and Space Administration (NASA) Earth Observing System. AIRS along with its partner microwave instrument, Advanced Microwave Sounding Unit (AMSU-A), represents an advanced atmospheric sounding system. Combined two instruments aim at observing the global water and energy cycles, climate variation and trends, and the response of the climate system to increased greenhouse gases.

AIRS built by NASA Jet Propulsion Laboratory, is a cross-track scanning instrument. Its scan mirror rotates around an axis along the line of flight and directs IR energy from the Earth into the instrument. As the spacecraft moves along, this mirror sweeps the ground creating a scan swath that extends roughly 1650 km. Aqua is in a sun-synchronous orbit with ascending node at 1:30 pm local time. AIRS covers the global two times (daytime and nighttime) a day, but some points near the equator are missed since the swaths do not overlap at low latitudes. The spatial resolution is 13.5 km at nadir and  $41 \times 21.4$  km at the scan extremes. The scan geometries of

AIRS and its partner microwave instruments, AMSU-A, and the Humidity Sounder for Brazil (HSB), are illustrated in Figure 6.

Within the AIRS instrument the IR energy is separated into wavelengths, similar to rain drops splitting sunlight into a rainbow. By having multiple IR detectors, each senses radiance at a particular wavelength with 2,378 detectors covering the IR spectral range of 3.8–4.6  $\mu\text{m}$ , 6.2–8.2  $\mu\text{m}$ , and 8.8–15.4  $\mu\text{m}$  at a nominal spectral resolution of  $\lambda/\Delta\lambda = 1200$ . Radiometric sensitivity expressed as the Noise Equivalent Temperature Difference (NE $\Delta$ T) for a scene temperature of 250 K is 0.07–0.4 K for 3.75–11  $\mu\text{m}$ , and 0.27–0.68 K for 11.75–15.4  $\mu\text{m}$ . Detailed NE $\Delta$ T at 250 K measured in orbit for the 2,378 channels are shown in Figure 7. These great improvements of the spectral resolution and accuracy make it available to retrieve temperature and water vapor over a range of heights in the atmosphere.

Absorption by gases in the atmosphere is mainly a feature of the IR bands, and thus each IR wavelength is quite sensitive to temperature and other gases. The AIRS upwelling spectrum in Figure 8 suggests that an AIRS spectrum contains gaseous absorption bands by water vapor, CO<sub>2</sub>, O<sub>3</sub>, and other trace gases. In addition to the absorptions, it is noticed that the atmospheric gases are nearby transparent in the vicinity of 11  $\mu\text{m}$ , referred to as an ‘IR window region’ which mainly reflects surface conditions. Using information on the window and absorption regions over an AIRS spectrum, temperature and water vapor profiles have been officially produced and distributed with the purpose of improvement of weather forecasts and climate researches. Not only

the atmospheric profile retrieval, the extremely narrow spectral resolution allows us to resolve vertical distribution of other parameters such as cloud and dust.

Subsequent IR hypersepctral sensors on polar orbiting satellites are successfully launched and give more refined information about Earth's surface and atmosphere. The Infrared Atmospheric Sounding Interferometer (IASI) is one of the hyperspectral instruments measuring the spectral radiation of the atmosphere. Its instrument concept is based on the Michelson interferometer which allows an extremely narrow spectral resolution of  $0.35\text{--}0.5\text{ cm}^{-1}$  over a spectral range covering the IR region from  $3.62\text{ }\mu\text{m}$  ( $2760\text{ cm}^{-1}$ ) to  $15.5\text{ }\mu\text{m}$  ( $645\text{ cm}^{-1}$ ) with 8,461 channels. [Siméoni et al. 1997; Blumstein et al., 2004]. The first verification program for the IASI has been performed in vacuum on two occasions: testing and calibration at the instrument level and integration at the MetOp payload level. These two tests have shown that the first verification performance has been successfully completed [Blumstein et al., 2004]. The first flight model was launched in 2006 onboard the first European meteorological polar-orbiting satellites, MetOp-A. The second and third instruments will be mounted on the MetOp-B and C satellites with launches scheduled on September 2012 and October-November 2016, respectively.

The Cross-track Infrared Sounder (CrIS), a Fourier transform spectrometer observes the emitted radiance with 1305 spectral channels over three wavelength ranges:  $9.14\text{--}15.38\text{ }\mu\text{m}$ ;  $5.71\text{--}8.26\text{ }\mu\text{m}$ ; and  $3.92\text{--}4.64\text{ }\mu\text{m}$  [Bloom 2001; Glumb et al. 2003]. CrIS is on aboard the Suomi National Polar-

orbiting Partnership (NPP) spacecraft lifted off on Oct. 28, 2011, to begin its Earth observation mission. The early check of CrIS shows that its spectral calibration is proving to be excellent, with a spectral accuracy of approximately  $\sim 1$  ppm (= 0.015 K at  $2388\text{ cm}^{-1}$ ). The random noise performance of CrIS in the longwave spectral region is approximately four times better than AIRS and IASI, and comparable to AIRS in the midwave and shortwave spectral regions. The Joint Polar Satellite System (JPSS), the next generation polar-orbiting operational environmental satellite system procured by the National Oceanic and Atmospheric Administration (NOAA), will be loaded the CrIS providing continuity of observation. JPSS-1 and -2 are scheduled to be launched in 2016 and 2022, respectively.

Not only is the polar-orbiting satellite, a project for IR hyperspectral sensors in geostationary satellites is preceding now. GeoMetWatch (GMW) is a commercial company licensed by the U. S. Government to operate a global geostationary hyperspectral imaging/sounding system. GMW and its partners are developing an advanced sensor, 'Sounding & Tracking Observatory for Regional Meteorology (STORM)' which will be mounted on six geostationary orbit satellites. The first launch is slated for 2015, with the full complement GMW global constellation, comprised of the Six-Satellite-STORM-System (S4), to be fully deployed by 2019–2020. Each STORM sensor makes full-disk observations every 20 minutes to one hour with  $0.6\text{--}2.5\text{ cm}^{-1}$  spectral resolution over an IR range of  $4.3\text{--}15.2\text{ }\mu\text{m}$  at 2 km Field-Of-View (FOV).

The next European operational geostationary meteorological satellite

system, the Meteosat Third Generation (MTG) will comprise six satellites, with the first spacecraft likely to be ready for launch from 2020. MTG will have more advanced instruments, including an interferometer, the Infra-red Sounder (IRS). The IRS is based on an imaging Fourier interferometer with a spectral resolution of  $0.625 \text{ cm}^{-1}$  wavenumber, taking measurements in two bands of the long wave IR (14.3–8.3  $\mu\text{m}$ ) and the midwave IR (6.25–4.6  $\mu\text{m}$ ), with a spatial resolution of 4 km. The IRS will deliver over the full disk in the long wave IR 800 spectral channels and in the midwave 920 channels with a basic repeat cycle of 60 minutes.

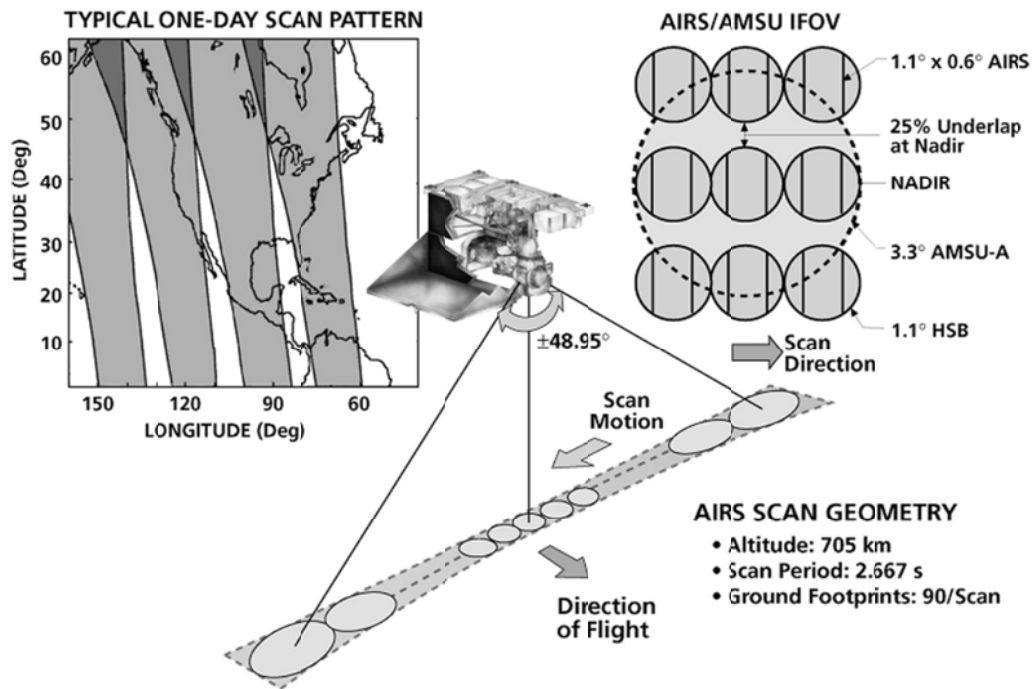


Figure 6. AIRS scan geometry and the relative alignment of the AIRS/AMSU/HSB footprints. [Aumann et al., 2003]

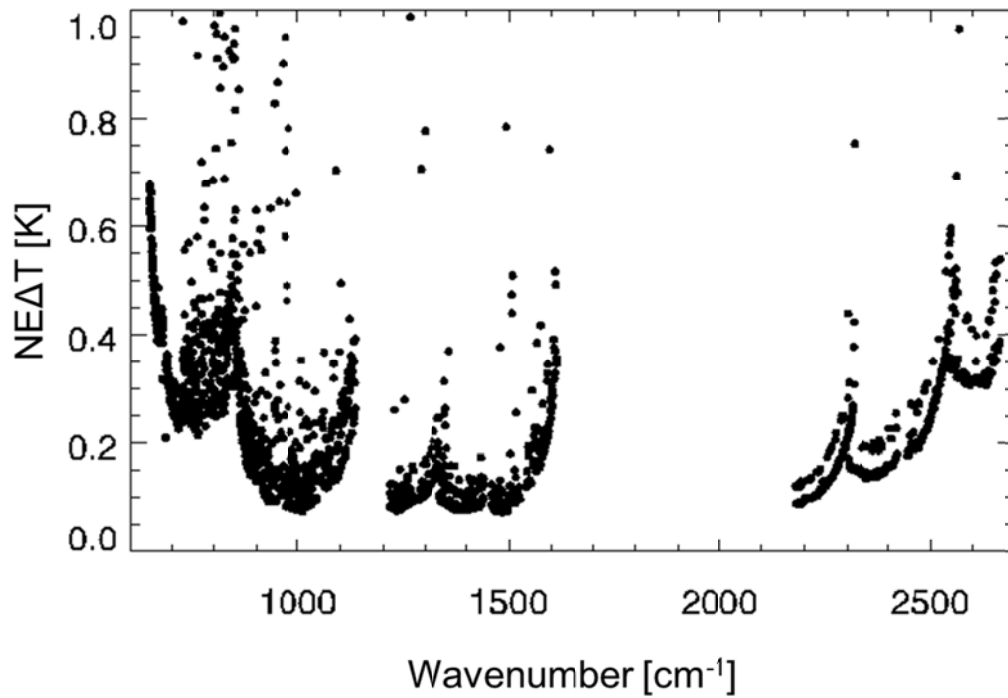


Figure 7. AIRS Noise Equivalent Temperature Difference (NE $\Delta$ T) at 250 K measured in orbit.

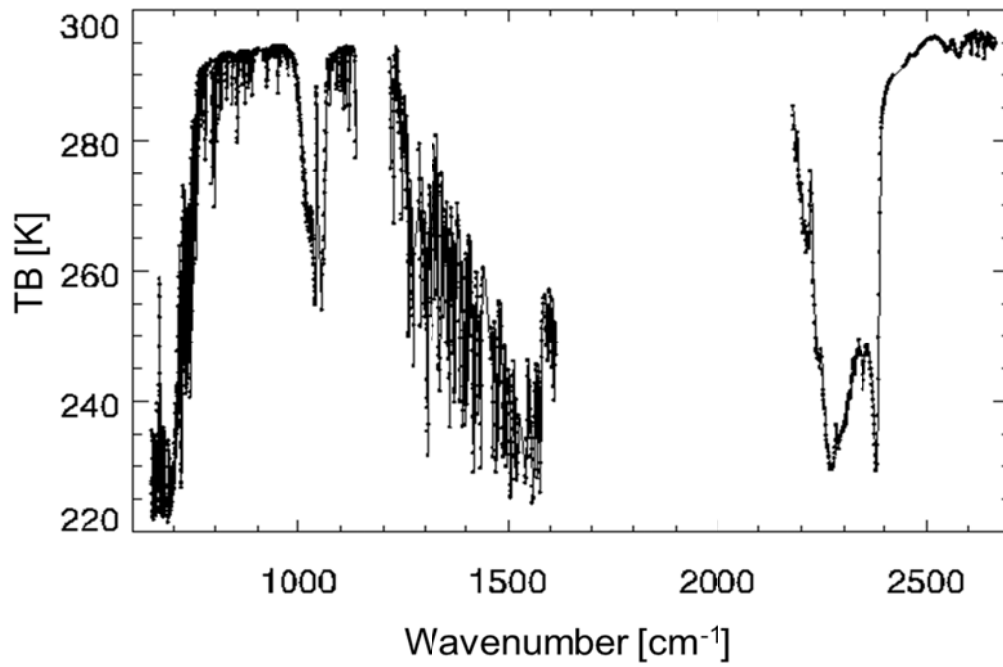


Figure 8. Simulated AIRS upwelling spectrum in TB. The simulation is performed using 'Mid-latitude summer atmospheric profile' and constant surface emissivity of 1.0.

## **4. Examining dust signal in the AIRS hyperspectral measurements**

### **4.1 Sensitivity of IR TB to dust amount and height**

Radiative transfer simulations are performed in order to examine the effect of mineral dust on IR spectra for various AOT and dust height using the fast Radiative Transfer for Television Infrared Observation Satellite (TIROS) Operational Vertical Sounder (RTTOV) version 9.3. For each simulation, we assume that only one layer contains a homogeneously distributed dust, and daytime situations are not considered. Surface and atmospheric profiles are from ‘Mid-latitude summer atmospheric profile’ while surface emissivity is set to constant of 1.0. The simulated TBs and dust effects are illustrated in Figure 9 and 10. For each figure, only one variable (AOT or dust height) is changed while keeping other reference values fixed, i.e., AOT = 0.8 and dust height = 707 hPa.

The simulated IR TBs show that the dust signal increases with AOT and height, and can reach up to 12 K (e.g. AOT=2.0). The simulated effect of Asian dusts on IR spectra is particularly substantial over IR window regions (i.e.: 3.7–4.1  $\mu\text{m}$ , 8.8–9.3  $\mu\text{m}$ , 10–13  $\mu\text{m}$ ), although the window regions are also sensitive to surface temperature and emissivity. Comparing the dust effects of various AOT and heights in Figure 9b and 10b, respectively, it is noticed that shortwave channels (3–5  $\mu\text{m}$ ) are mostly sensitive to AOT, whereas longwave

channels (8–12  $\mu\text{m}$ ) are sensitive to both of AOT and height. Dust signals for various heights are obvious over the  $\text{CO}_2$  and water vapor bands, albeit much smaller than window regions. The effect of various dust heights on  $\text{CO}_2$  and water vapor bands indicates that these bands carry information on dust heights, in company with the temperature and water vapor profiles. The sensitivity tests suggest that dust effect on IR spectra is apparently enough to be used for retrieval of mineral dust. However, since an IR spectrum is very sensitive to environmental states, it is critical to acquire information relative to surface and atmospheric conditions.

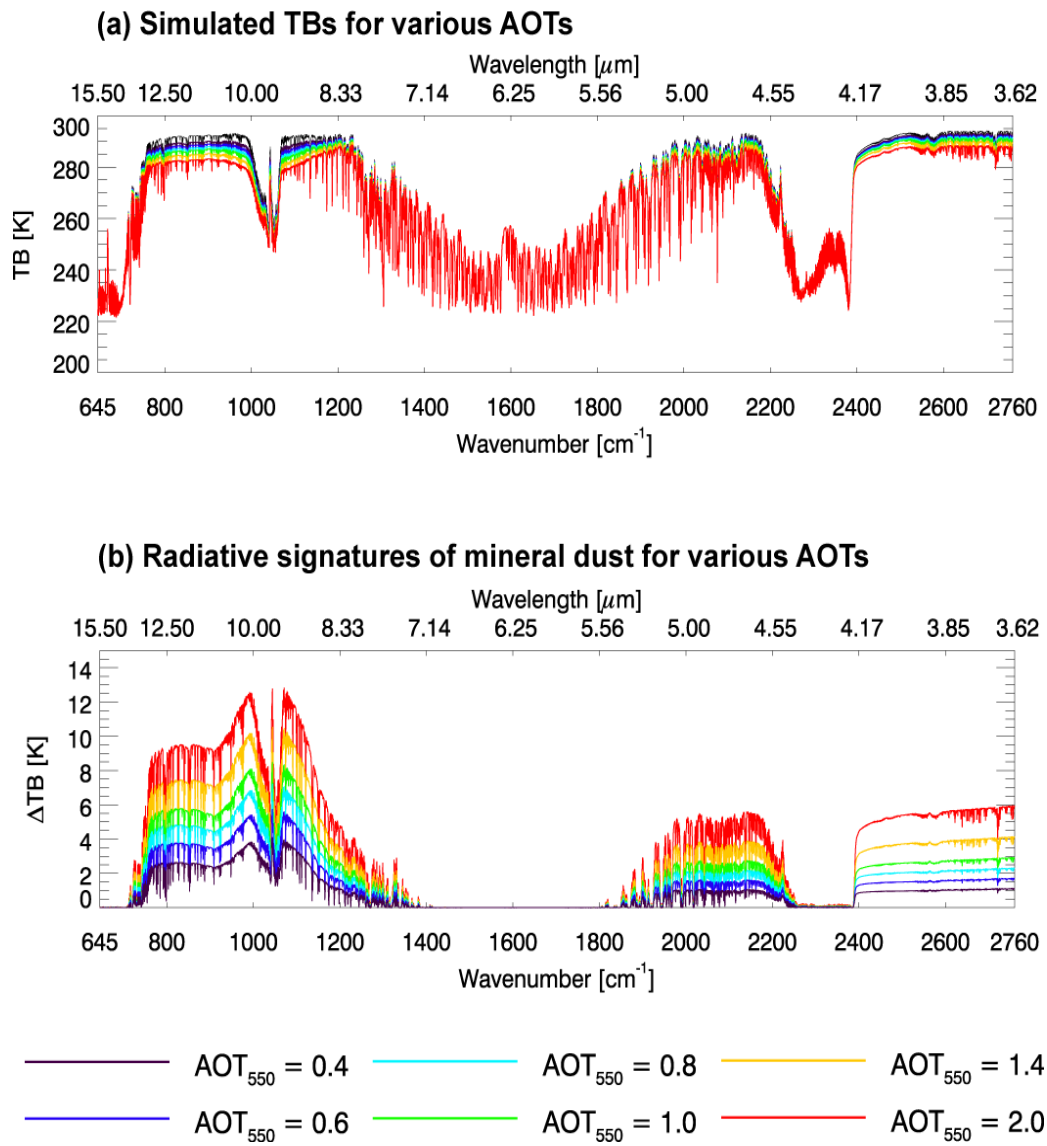
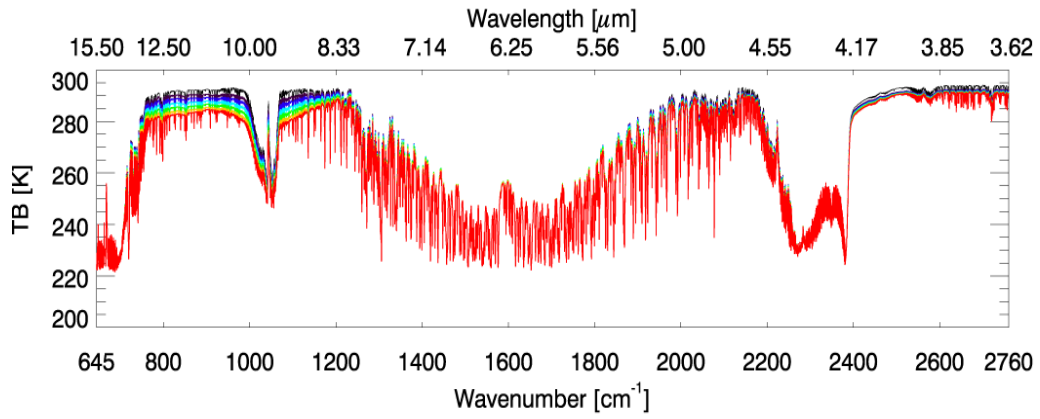


Figure 9. (a) Simulated IR TBs with various AOT and (b) differences between TBs simulated under clear-sky and mineral dust condition.

**(a) Simulated TBs for various dust altitudes**



**(b) Radiative signatures of mineral dust for various dust altitudes**

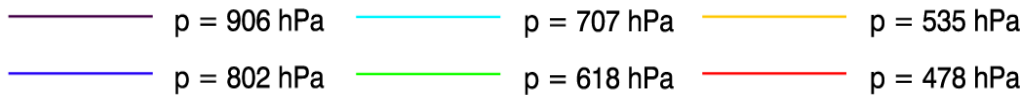
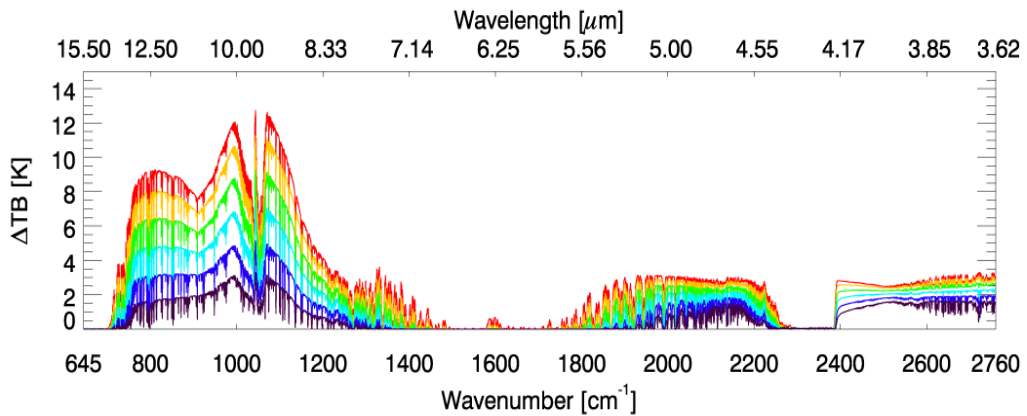


Figure 10. Same as Figure 9 except for various dust heights.

## 4.2 Construction of training data sets for ANN model

To further examine whether the IR hyperspectral measurements can be used for the dust retrieval, a statistical approach is employed with the use of remotely-sensed AIRS measurements. One of the statistical methods we adopt here is the ANN method as it enables to learn about an arbitrary function through a training process, which can produce a model describing a nonlinear relationship between variables [Krasnopolsky and Schiller, 2003; Mas and Flores, 2008]. For training the ANN model, a set of collocated data is necessary to relate predictand (here, AOT or dust height) to predictor variables (here, AIRS TBs and other inputs). The recent A-Train mission [Stephens et al., 2002] provides a good means to construct these necessary collocated data sets, from which the ANN training can be accomplished.

Although measurements are available for both daytime and nighttime, only the longer wavelength spectral measurements over the 6.2–15.4  $\mu\text{m}$  band are used to construct the collocated data, excluding the solar-affected band (3.8–4.6  $\mu\text{m}$ ) during the daytime. AIRS channels covering the wavelength range 6.2–15.4  $\mu\text{m}$  are roughly divided into four bands: window (WIN; 8.15–12.8  $\mu\text{m}$ ),  $\text{CO}_2$  (12.9–15.0  $\mu\text{m}$ ), water vapor (WV; 6.3–8.0  $\mu\text{m}$ ), and  $\text{O}_3$  (9.2–10.1  $\mu\text{m}$ ). Considering only channels with lower noise equivalent differential temperatures ( $\text{NE}\Delta\text{T}$ ) and removing weak gaseous absorption channels over the WIN band, a total of 234 channels (130, 31, 44, and 29 channels for the WIN,  $\text{CO}_2$ , WV, and  $\text{O}_3$  bands, respectively) are selected for the ANN model development. Spectral locations of the selected channels are shown in Figure 11.

Relating AIRS-measured brightness temperatures described above to AOTs through the ANN learning procedures, we use MODIS-derived AOT data. The MODIS sensor onboard the same Aqua satellite measures radiances at 36 spectral bands spanning the VIS-IR region (0.415–14.235  $\mu\text{m}$ ) with a spatial resolution of 250 m, 500 m, or 1 km at nadir, depending on the wavelength. The MODIS Level 2 aerosol product ('MYD04\_L2') provides aerosol properties with a spatial resolution of about 10 km based on VIS measurements [Remer et al., 2005]. In this study, AOTs based on 'Deep Blue Aerosol Optical Depth 550 Land' [Hsu et al., 2004] are collocated with AIRS TBs over land because the deep blue algorithm (using channels at wavelengths shorter than 0.5  $\mu\text{m}$ ) is known to more efficiently detect dust aerosols over bright arid and semiarid regions. Over the ocean, AOTs from 'Optical Depth Land and Ocean' based on a look-up table approach [Levy et al., 2003] are collocated with AIRS TB data.

Separately from the training for the AOT, AIRS TBs are related to CALIPSO-derived dust heights for developing an ANN model for the dust height. The CALIPSO satellite, also part of the A-Train, has a two-wavelength (532 and 1,064 nm) lidar instrument CALIOP that offers a cross-sectional view of aerosol and thin cloud along the satellite track [Winker et al., 2007]. The CALIPSO Lidar Level 2 Aerosol Layer ('CAL\_LID\_L2\_05kmALay') top and base heights ('Layer\_Top\_Altitude' and 'Layer\_Base\_Altitude,' respectively) and AOT at 532 nm ('Feature\_Optical\_Depth\_532') are collected to specify vertical distribution of dust layers and to construct a training data set for the ANN model. In order to identify dust-laden pixels, data flagged as dust or

polluted dust aerosols in 'Feature\_Classification\_Flag' of the CALIPSO aerosol product are used for collocation with AIRS TBs. Total attenuated backscatter profiles at 532 nm, measured by the CALIOP, are used for validating AIRS-derived height for case studies.

In addition, land surface topography ( $z_{\text{stc}}$ ) and relative air mass from the surface to the sensor ( $1/\mu$ ;  $\mu = \cos\theta$  where  $\theta$  is the satellite viewing angle) are included as inputs to the model.  $\text{BTD}_{11-12}$  are also included as an input to examine the sensitivity of the ANN model to the given inputs. For the  $\text{BTD}_{11-12}$  calculation, the difference is taken between TBs averaged over the 11.8–12.2  $\mu\text{m}$  and 10.8–11.2  $\mu\text{m}$  bands.

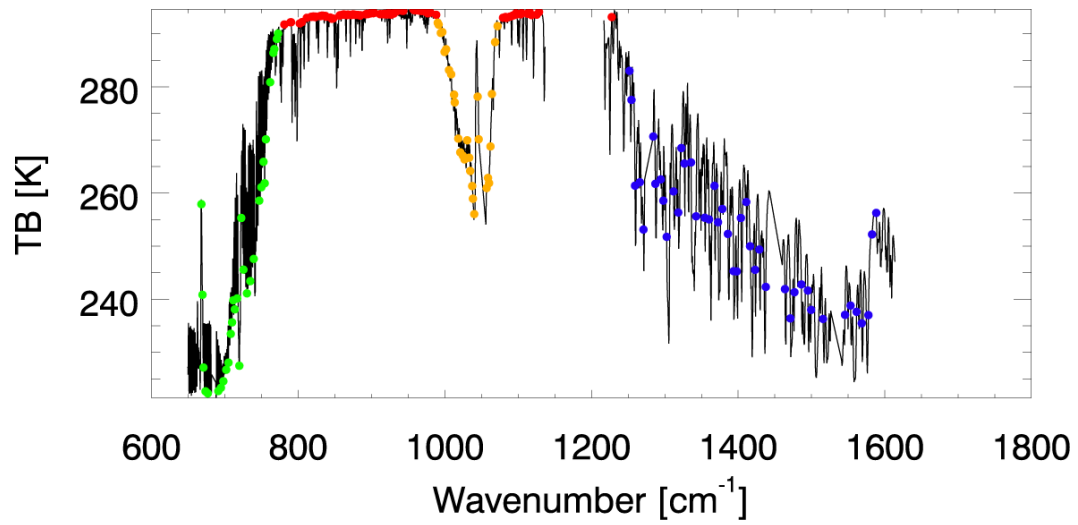


Figure 11. Selected AIRS 234 channels used for the ANN model development in this study. Dots in green, red, yellow, and blue represent selected channels over CO<sub>2</sub>, WIN, O<sub>3</sub>, and WV bands, respectively.

### 4.2.1 Detecting FOVS containing dust

The NASA's AIRS Level 1B operational retrieval system currently produces a dust detection flag using a dust-detection algorithm (DDA) [DeSouza-Machado et al., 2010] indicating an identifiable amount of material present in the atmosphere. It computes BTDs for five AIRS channels near the 10  $\mu\text{m}$  atmospheric window region, 822.4, 900.3, 961.1, 1129.0 and 1231.3  $\text{cm}^{-1}$ . These channels were chosen since they have relatively low noise, span either side of the region of strong IR dust absorption, and avoid ice absorption as shown in Figure 12. The peak region of dust imaginary refractive index on a wavenumber range of 1000–1100  $\text{cm}^{-1}$  is not used, as it coincides with the region of strong ozone absorption peak. These BTDs undergo a number of tests to generate a summed score, with the FOV tagged 'dusty' if the scores exceed a threshold value. The DDA tests described by DeSouza-Machado et al. [2010] assume an underlying ocean emissivity, and developed over dust-laid tropical and mid-latitude oceans of the Atlantic.

Since the DDA basically originate from BTD method using IR window channels, its performance inevitably exhibits regional differences, as does the BTD retrieval approach [Darmenov and Sokolik, 2005]. Comparing with MODIS true images of Asian dust, the DDA was modified by altering test and cumulative thresholds. Table 1 summarizes the algorithm applied to detect Asian dust. Although the DDA is a highly effective algorithm to identify dust-laid pixel, this simple test is unable to provide quantitative information on dust such as AOT and height. DeSouza-Machado et al. [2010] suggest that the main

purpose of the DDA is to quickly determine if the dust content of a scene is large enough to warrant a more sophisticated retrieval. Therefore in this study, use of the DDA is limited to select AIRS FOVs which are covered with dust and applicable to dust retrieval algorithm.

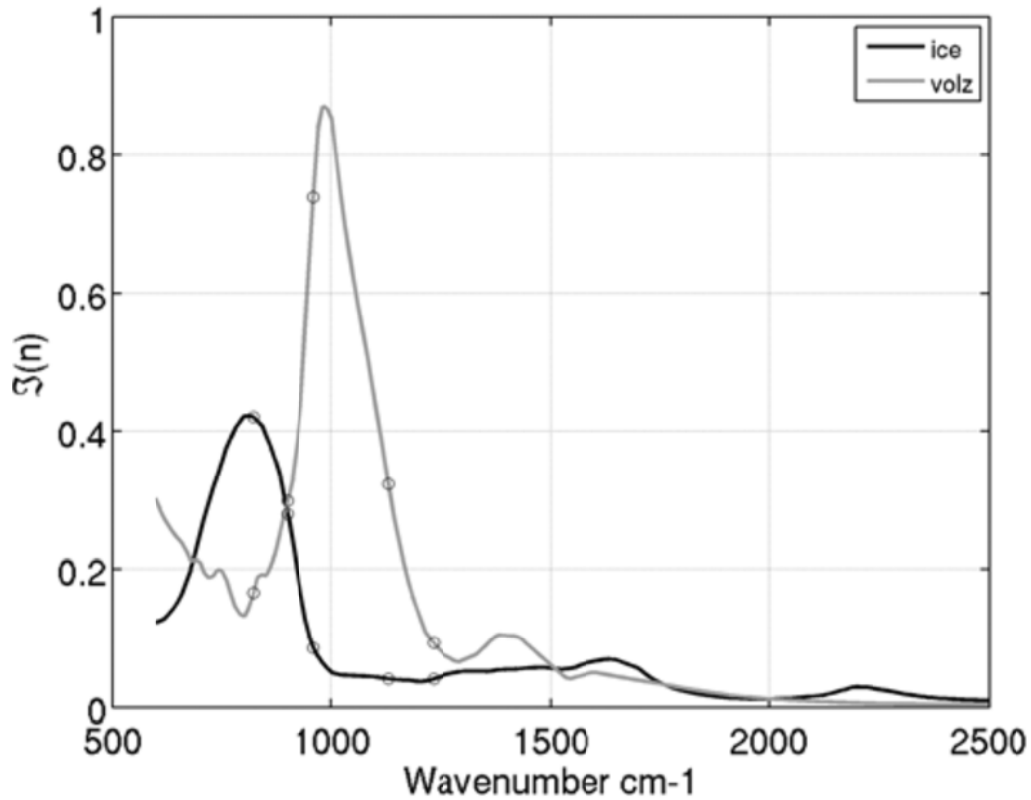


Figure 12. Imaginary part (absorptive component) of ice and dust refractive indices. The Volz Saharan dust data is used for this plot. The circles show the locations of the AIRS channels used for the DDA. Note that dust has a peak absorption at about  $10\ \mu\text{m}$  ( $1000\ \text{cm}^{-1}$ ) while ice has a peak absorption at longer wavelengths (about  $12\ \mu\text{m}$  or  $800\ \text{cm}^{-1}$ ). This spectral separation can allow IR instruments to discriminate between the presence of ice or dust in a FOV. Ozone also has peak absorption in the  $1000\text{--}1080\ \text{cm}^{-1}$  region. [DeSouza-Machado et al., 2010]

#### 4.2.2 Construction of collocated AIRS vs. MODIS data

For a given dust loading in an atmospheric column, the spectral variation of optical thickness can be expressed by spectrally varying extinction efficiencies that can be obtained from the Mie calculation. That is,

$$\tau_{\lambda_1} = \frac{Q_{ext,\lambda_1}}{Q_{ext,\lambda_2}} \tau_{\lambda_2} \quad (2)$$

where  $Q_{ext,\lambda_1}$  and  $Q_{ext,\lambda_2}$  represent extinction efficiencies at two wavelengths  $\lambda_1$  and  $\lambda_2$ , respectively. Taking  $\lambda_1$  and  $\lambda_2$  as the VIS and IR bands, respectively, IR-based AOT can be converted to an equivalent to VIS-based AOT. Instead of explicitly relating AOTs from different spectral bands, the ANN method may implicitly relate the IR TBs to VIS-based AOT, through an expected relationship between IR TBs and IR-based AOT. It should be noted that Equation. (2) is valid only if loaded aerosols are also sensitive to the IR spectra. When dusts are a dominant aerosol species, Equation (2) can be accepted as a first-order approximation for converting AOT at one band to AOT at a different band. In fact, Lee and Sohn [2012] was able to retrieve AOT at 550 nm from MODIS IR TBs using a similar ANN method.

In training, the predictand (or target output) in the AOT retrieval model is defined as the AOT equivalent to that retrieved from MODIS at 550 nm, such that AIRS TBs can be implicitly related to AOTs at 550 nm. Because of the similar target sizes of AIRS and MODIS, the MODIS AOT whose target location is closest to the AIRS FOV is chosen for collocation. Training data for AOT are constructed for a period from February to May 2007 over the East

Asian region (15–55°N and 70–150°E). In this procedure, only dust-laden AIRS pixels are retained after applying the AIRS-based dust detection method, DDA, described above. Although clouds are excluded in the process of dust detection using the DDA, AIRS Level 2 effective cloud fraction ‘CldFrcSfd’ is also employed for more distinct cloud screening by taking AIRS FOVs with mean cloud fraction less than 0.2.

### 4.2.3 Construction of collocated CALIPSO vs. AIRS data

For a given atmospheric column, dust is determined to be present if the CALIPSO feature classification flag indicates dust or polluted dust. Then, vertical extent of dust layer is determined from CALIPSO-derived top and bottom altitudes of single or multiple dust layers. For the ANN training model for dust height, all dust layer heights within one CALIPSO pixel are weighted by AOTs of the corresponding layers to obtain a single dust effective height ( $z_{dust}$ ) at a given location, i.e.,

$$z_{dust} = \sum_{i=1}^N z(i) \frac{AOT(i)}{AOT(total)} \quad (3)$$

where  $z(i)$  and  $AOT(i)$  are mean height above sea level and AOT at the  $i$ th dust layer, respectively, and  $N$  is the total number of dust layers from CALIPSO products. Thus, in Equation (3),  $AOT(total)$  is a simple summation of AOTs in  $N$  individual dust layers. Because of the weighted mean,  $z_{dust}$  can be considered to be ‘effective dust height’, but we keep ‘dust height’ in this study for the simplicity.

Due to different spatial resolutions (i.e. 13.5 km versus 5 km at nadir for AIRS and CALIPSO, respectively), multiple CALIPSO pixels can be within one AIRS FOV. All CALIPSO aerosol measurements along the track within an AIRS FOV are averaged to collocate to AIRS data if at least one of the CALIPSO pixels is determined to be dust-laden. The collocation is performed over the same geographical domain used for MODIS AOT-TB collocation but over a two-year period (January 2007–December 2008).

Table 1. AIRS Dust Flag Detection<sup>a</sup>

Classification	Test Channel BTD over ocean <sup>b</sup>	Test Channel BTD over land <sup>b</sup>	Score
Dust0	$\text{find}((b-d) \geq -0.5 \text{ and } (b-d) \leq 1.00)$	$\text{find}((b-d) \geq -0.5 \text{ and } (b-d) \leq 1.00)$	1
Dust1	$\text{find}((d-e) \leq -1.25)$	$\text{find}((d-e) \leq -1.25)$	2
Dust2	$\text{find}((d-a) \leq -0.75)$	$\text{find}((d-a) \leq -0.75)$	4
Dust3	$\text{find}((c-d) \geq -0.2 \text{ and } (c-d) \leq 1.0)$	$\text{find}((c-d) \geq -0.2 \text{ and } (c-d) \leq 1.0)$	8
Dust4	$\text{find}((b-e) \geq -4.5 \text{ and } (b-e) \leq -0.3)$	$\text{find}((b-e) \geq -4.5 \text{ and } (b-e) \leq -0.3)$	16
Dust5	$\text{find}((b-a) \leq 0.115)$	$\text{find}((b-a) \leq 0.115)$	32
Dust6	$\text{find}((b-c) \geq 0.05 \text{ and } (b-c) \leq 1.5)$	$\text{find}((b-c) \geq 0.05 \text{ and } (b-c) \leq 1.5)$	64
Dust7	$\text{find}((c-a) \leq 0.80)$	$\text{find}((c-a) \leq 0.40)$	128
Dust8	$\text{find}((c-e) \leq 0.2)$	$\text{find}((c-e) \leq -0.15)$	256

<sup>a</sup>Cumulative threshold are 380 and 360 for ocean and land, respectively.

<sup>b</sup>Channel centers (a)–(e) are 822.4, 900.3, 961.1, 1129.0 and 1231.3  $\text{cm}^{-1}$  respectively. Thresholds for tests 7 and 8 must be modified for best performance over land.

### 4.3 ANN model development

Remotely sensed IR radiances from satellites carry information related to atmospheric parameters, but have a strong nonlinearity. In a nonscattering atmosphere, the upward radiance ( $I_\lambda$ ) at the top of the atmosphere is influenced by surface emissivity ( $\varepsilon_\lambda$ ), surface temperature ( $T_s$ ), relative airmass ( $m_r=1/\mu$ ;  $\mu=\cos\theta$ , where  $\theta$  is the sensor zenith angle), and the optical thickness ( $\tau$ ) from the surface to the TOA, i.e.,

$$I_\lambda = \varepsilon_\lambda B_\lambda(T_s) e^{-\tau/\mu} + \int_0^\tau B_\lambda(\tau') e^{-\tau'/\mu} \frac{d\tau'}{\mu} \quad (4)$$

The TOA IR radiance,  $I_\lambda$ , is contributed by the nonlinear combination of emissivity with layer mean temperature, and by surface emission. Because of the high complexity inherent in physically determining the AOT from IR TBs as shown in Equation (4), there may not be a general way to link IR TBs to VIS-based AOTs. Thus, it should be worthwhile to examine to what extent dust information may be gleaned from hyperspectral measurements, using a tool that can explain the nonlinear relationship between dust loading and IR radiances.

The ANN provides a convenient and powerful means of performing nonlinear classification and regression by partitioning the input space into subdomains, which may then be associated with a desired set of output values [Freeman and Skapura, 1991]. We use a so-called multilayer perceptron (MLP) ANN model, which allows a feed-forward network to link either MODIS AOT at 550 nm or CALIOP  $z_{\text{dust}}$  with AIRS TBs over the WIN, CO<sub>2</sub>, WV, O<sub>3</sub> bands, and with  $z_{\text{sfc}}$ ,  $1/\mu$ , and BTD<sub>11-12</sub>. The multilayer feed-forward ANN model used

in this study consists of three layers—an input layer, a hidden layer, and an output layer—that are connected by synaptic weights. The model has a single hidden layer with 5 neurons, and a tangent sigmoidal function is used in all the neurons to fit the nonlinear response of neurons to given inputs. A bias parameter is added to both the hidden and output layers for more flexible use of the activation function. In the training procedure, a learning rate of 0.01 and a bias of 1 are provided. The weight adaptation rule considered here is a *backpropagation algorithm*, which is a steepest descent algorithm to minimize the error term [Rumelhart et al., 1986]. Implementation details of the training process can be found in Brierley and Batty [1999], and a more theoretical basis in Bishop [1995]. The structure of the ANN model is shown in Figure 13.

Using the collocated datasets, ANN models are developed by first examining how well the ANN model performs with given input parameters. A total of 46,073 collocated MODIS AOTs are related to various input parameters. Sensitivity tests are conducted by adding parameters in an orderly manner (i.e., TBs over the WIN band first, followed by TBs over the CO<sub>2</sub>, WV, and O<sub>3</sub> bands, and  $z_{\text{sfc}}$ ,  $1/\mu$ , and BTD<sub>11-12</sub> last, in a cumulative fashion).

The obtained correlation coefficient and root mean square error (RMSE) for each given input parameters are shown in Figure 14a for AOT. It is noted that training results based only on WIN band TBs shows good agreement with MODIS AOT retrievals, with a correlation coefficient larger than 0.86, demonstrating that hyperspectral WIN channel measurements carry rich information about dust AOTs. With more channels from other bands (i.e., CO<sub>2</sub>,

WV, and  $O_3$ ) added for training, statistics steadily improve with each addition.  $z_{\text{sfc}}$  and  $1/\mu$  also exert a positive influence on the correlation, resulting in a highest correlation coefficient of around 0.90 and lowest RMSE of 0.34 when combined with TBs over various bands. However, poorer statistics are noted for  $\text{BTD}_{11-12}$ , probably because  $\text{BTD}_{11-12}$  is a degraded WIN band that contains information that has already been used in 130 WIN channels.

Using 50,976 pairs of collocated data, the same procedures used for AOT are applied to examine how sensitive  $z_{\text{dust}}$  retrieval is to given input parameters. Statistics obtained from these sensitivity tests are given in Figure 14b. A correlation coefficient of 0.68 for only the WIN channel TBs suggests that  $z_{\text{dust}}$  is also most sensitive to WIN channels, although the correlation is weaker than that in the AOT test. It is noted that a substantial variance is explained by adding  $\text{CO}_2$  channel TBs, as shown in correlation coefficient increased to about 0.74 and reduced RMSE from about 0.94 km to 0.86 km. The substantial improvement in statistics resulting from the addition of the  $\text{CO}_2$  channels suggests that the synergistic use of WIN channels with  $\text{CO}_2$  channels can improve  $z_{\text{dust}}$  retrieval from hyperspectral sounder measurements. This may be because information about temperature profiles from  $\text{CO}_2$  channels can be added to dust emissivity information, likely from WIN channels, resulting in better description of TOA radiances. In contrast, other input parameters such as WV,  $O_3$ ,  $1/\mu$ , and  $\text{BTD}_{11-12}$  appear to have little impact on  $z_{\text{dust}}$  retrieval, despite slightly improving statistics with addition of further input parameters. Again, the addition of  $\text{BTD}_{11-12}$  tends to detract from the overall performance of  $z_{\text{dust}}$

retrieval.

Based on the results of the sensitivity tests, it can be concluded that WIN channels are most important for both AOT and  $z_{\text{dust}}$  retrieval. However, adding CO<sub>2</sub> channels results in substantial improvements in  $z_{\text{dust}}$  retrieval. Nevertheless, in this study, we use all parameters except BTD<sub>11-12</sub> in the development of ANN models for both AOT and  $z_{\text{dust}}$  because of the tendency for resultant statistics to improve with the addition of parameters (listed in Table 2).

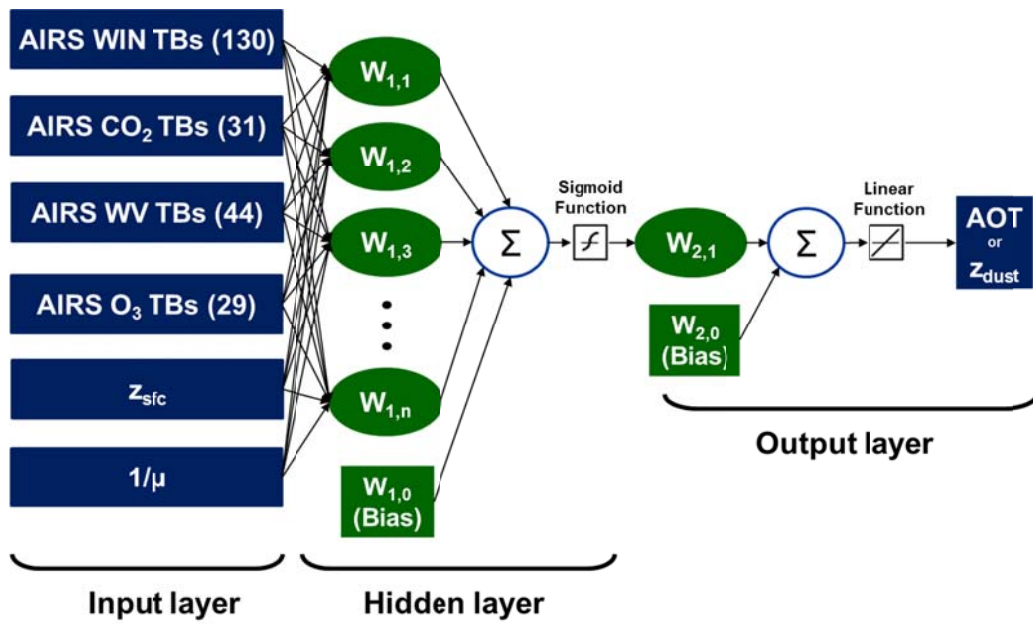


Figure 13. Structure of the ANN model showing 236 inputs (234 AIRS TBs, topography ( $z_{sfc}$ ), and relative airmass of the sensor ( $1/\mu$ )), a single hidden layer with 5 neurons, and the target outputs (AOT and dust height ( $z_{dust}$ )).

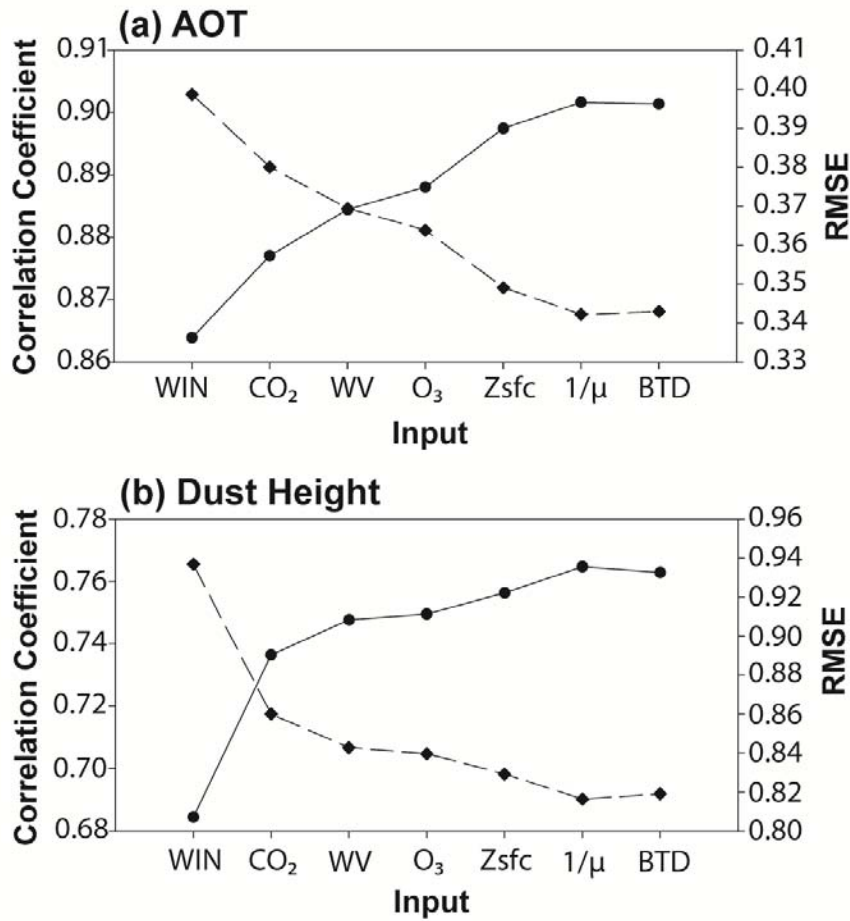


Figure 14. Correlation coefficients and RMSEs (a) between AIRS-derived and MODIS-estimated AOTs, and (b) between AIRS-derived and CALIPO-measured dust height. Solid and dashed lines are for correlation and RMSE, respectively. WIN, CO<sub>2</sub>, WV, and O<sub>3</sub> on the abscissa represent inputs of AIRS TBs at window, CO<sub>2</sub>, water vapor, O<sub>3</sub> bands, respectively. And  $z_{sfc}$ : land surface topography,  $1/\mu$ : relative airmass from the surface to the sensor,  $BTD_{11-12}$ : brightness temperature difference between 11  $\mu\text{m}$  and 12  $\mu\text{m}$ . Inputs are arranged in a cumulative fashion.

Table 2. Inputs used for the Artificial Neural Network models

Inputs	Notations	Descriptions
1–130	AIRS WIN TBs	AIRS TBs at window band (8.1 –12.8 $\mu\text{m}$ )
131–161	AIRS CO <sub>2</sub> TBs	AIRS TBs at CO <sub>2</sub> band (12.9–15.0 $\mu\text{m}$ )
162–205	AIRS WV TBs	AIRS TBs at water vapor band (6.3–8.0 $\mu\text{m}$ )
206–234	AIRS O <sub>3</sub> TBs	AIRS TBs at O <sub>3</sub> band (9.2–10.1 $\mu\text{m}$ )
235	$z_{\text{sfc}}$	Topography
236	$1/\mu$	Relative airmass (secant of $\theta_{\text{sat}}$ )

## 4.4 Validation

In order to validate the performance of the retrieval models discussed above, we compare AIRS pixel-based AOT and  $z_{\text{dust}}$  retrievals with MODIS AOT and CALIPSO  $z_{\text{dust}}$  estimates. For the validation of AOT retrieval from AIRS measurements, AIRS AOT retrievals during the period February–May 2008 are compared with collocated MODIS-derived AOTs. For the dust height validation, AIRS  $z_{\text{dust}}$  retrievals over a one-year period (January–December 2009) are compared with collocated CALIPSO measurements. Both comparisons are conducted for the same geographical domain used for constructing the training data set.

Comparison results from a total of 57,384 collocated pairs of AOTs are given in a two-dimensional density histogram (Figure 15a). It is indicated that AIRS AOTs obtained using the ANN method are in good agreement with MODIS AOTs, with a correlation coefficient of 0.84, mean bias of 0.03, and RMSE of 0.37. The obtained statistics suggest that MODIS-derived dust AOTs at 550 nm can be fairly accurately estimated from hyperspectral IR measurements, probably through the relationship between wavelengths and extinction efficiencies expressed in Equation (2). In other words, IR-based dust AOTs can be obtained quite accurately from hyperspectral IR sounder measurements and can, therefore, be related to the VIS AOTs through Eq. (2).

For the validation of  $z_{\text{dust}}$  retrievals, AIRS-retrieved  $z_{\text{dust}}$  data at a pixel level are collocated with CALIPSO measurements over a one-year period. Validation results based on a total of 20,272 AIRS dust pixels are presented in

Figure 15b. It is shown that the retrieved  $z_{\text{dust}}$  is in agreement with CALIPSO estimates, with a correlation coefficient of 0.79, mean bias of about -0.02 km, and RMSE of 0.54 km. It is of interest to note that a large portion of dust loadings are found below 3 km in weighted height. Note that the AIRS FOV along the CALIPSO track is about 13.5 km at the nadir, resulting in less than half of the pixel area being filled with CALIPSO pixels, which are not necessarily all dust pixels. Thus, it can be expected that better retrievals may be possible when exact collocated data sets with complete dust pixels are employed.

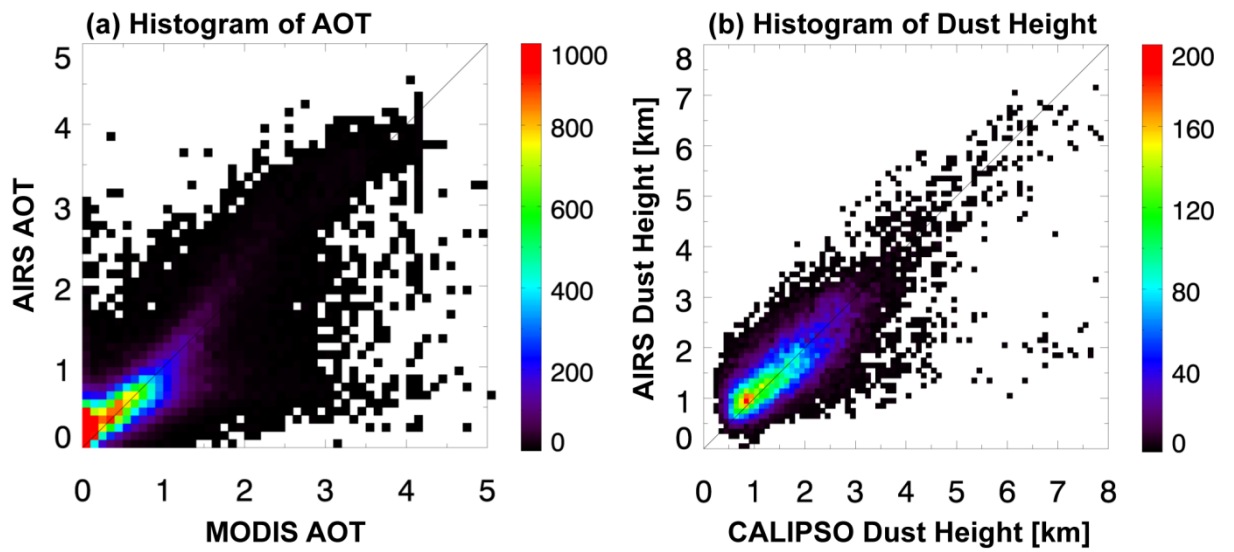


Figure 15. Two dimensional histogram of (a) MODIS-derived vs. ANN-retrieved AOTs for February–May 2008, and (b) CALIPSO-derived  $z_{\text{dust}}$  vs. ANN-retrieved  $z_{\text{dust}}$  for January–December 2009 in a 0.1 bin size.

#### 4.5 Case studies

In addition to the validation of the ANN models using general statistics, it is also of interest to examine how pixel-based ANN retrievals are related to MODIS and CALIPSO measurements. This is because pixel-level AIRS retrievals can provide not only daytime AOTs but also MODIS-like nighttime dust AOTs. Furthermore, two-dimensional  $z_{\text{dust}}$  data, comparable to those that can be obtained from CALIPSO  $z_{\text{dust}}$  measurements, can also be provided by AIRS measurements. Such data would be valuable for dust monitoring or application to dust forecasting. To demonstrate the feasibility of this, we select a dust event observed over China and Korea during March 1–2, 2008 and two cases of dust outbreaks that occurred on April 17, 2009 and April 23, 2009 over the Taklimakan and Inner Mongolian Gobi Deserts, respectively.

It should be noted here that the ANN model is retrained for  $z_{\text{dust}}$  without  $1/\mu$ . This is because the CALIPSO targets are within a viewing angle of 10 to 19° from the AIRS nadir view; thus, AIRS targets outside this range were not defined. Note that the following AIRS-derived  $z_{\text{dust}}$  data (in Figures 19 and 21) are retrieved from TBs on 234 channels and  $z_{\text{sfc}}$ .

#### **4.5.1 March 1–2, 2008 case**

In situ measurements indicate that an intense Asian dust event occurred over the Northeast China and Korea peninsular during March 1–2, 2008. Figure 16 provides MODIS true color images and retrieved AOTs using the trained ANN model and MODIS-derived AOTs. A strong dust plume is clearly presented in MODIS true color images (Figure 16a and 16b) moving rapidly from China to Korea across the Yellow Sea. Figure 16c–e are for AOTs retrieved from the ANN model, and the MODIS AOTs are displayed in the Figure 16f and 16g. A strong dust storm locating western Bohai bay and around Tianjin in China (Figure 16a, 16c, and 16f) moves eastward during nighttime on March 1 (Figure 16d), and finally arrived the Korean peninsula on March 2 (Figure 16b, 16e and 16g).

Figure 16c indicates that ANN AOT fairly well captures the dust storm nearby the Bohai bay on March 1, and gives a good agreement with MODIS AOT in both of strength and spatial distribution. Figure 16d focuses on retrieved AOT of the dust being advected toward the Korean peninsula over the Yellow Sea during nighttime. Only qualitative interpretation is possible from Figure 16d, because there are no comparable observation data to verify the nighttime AOT in this case. Though dust over the Shandong peninsula is not observed due to the relatively narrow swath of AIRS, the movement of dust band is clearly shown. Therefore we can conclude that it is possible to infer that the ANN-produced AOT can capture the movement pattern of nighttime dust band. In Figure 16e, a strong dust is retrieved from the ANN model over the

South Korea except some parts of central areas. Horizontal distribution of the ANN-produced dust coincides with the surface measurements and the MODIS true color image (Figure 16b). The dust band over the North Korea cannot be verified by in situ measurements, however, MODIS true color image shows that a strong dust covers the part of the North Korea indicating the model successfully retrieves the dust. On the other hand, Asian dust over the Korean peninsula is not retrieved by MODIS, probably due to clouds near the dust storm. The intense dust belt over the Yellow sea with AOT about 3.0 is observed by MODIS, but the AIRS measurements are not available due to its narrow swath.

Examining how the AOT retrievals match with ground-based measurements, AIRS-derived AOTs are compared with skyradiometer retrievals at two sites of the Aerosol Robotic Network (AERONET) in Figure 17. The geographical locations of the two sites, Xinglong in China and Gwangju in South Korea, are shown in Figure 17a. For comparisons, all AIRS-retrieved AOTs within a radius of 15 km of the sites are averaged and marked on Figure 17b and 17c with the time series of AOTs retrieved by skyradiometer measurements. Since MODIS-derived AOTs are not available near the sites, they could not be compared with the ground-based measurements.

The AOTs for various wavelengths retrieved from skyradiometer measurements at Xinglong are also plotted in Figure 17b. The skyradiometer-derived AOTs at 1020, 870, 675, and 440 nm wavelengths are available at Xinglong on March 1, 2008, and there seems to be little differences between the

AOTs depending on wavelengths, indicating that large dust particles are dominant. As shown in Figure 17b, the AIRS-derived AOT of 0.75 measured at 0500 UTC corresponds to the skyradiometer-retrieved AOTs in a range 0.76–0.81 which are observed at 0508 UTC. A strong dust event was also measured by the skyradiometer at Gwangju with AOTs in a range 1.5–3.0 on March 2, 2008. AOTs at seven wavelengths (1020, 870, 675, 500, 440, 380, and 340 nm) are retrieved, and their time series are plotted in Figure 17c. Comparing with the measurements in Xinglong, differences in AOT depending on wavelength are larger than those of Xinglong, suggesting that the particle size of dust in Gwangju is smaller than the one observed at upstream site. The AIRS-derived AOT of 1.95 is slightly smaller than the skyradiometer-retrieved AOTs. However, it is shown to be in a reasonable agreement with the skyradiometer-derived AOTs of 2.18–2.45.

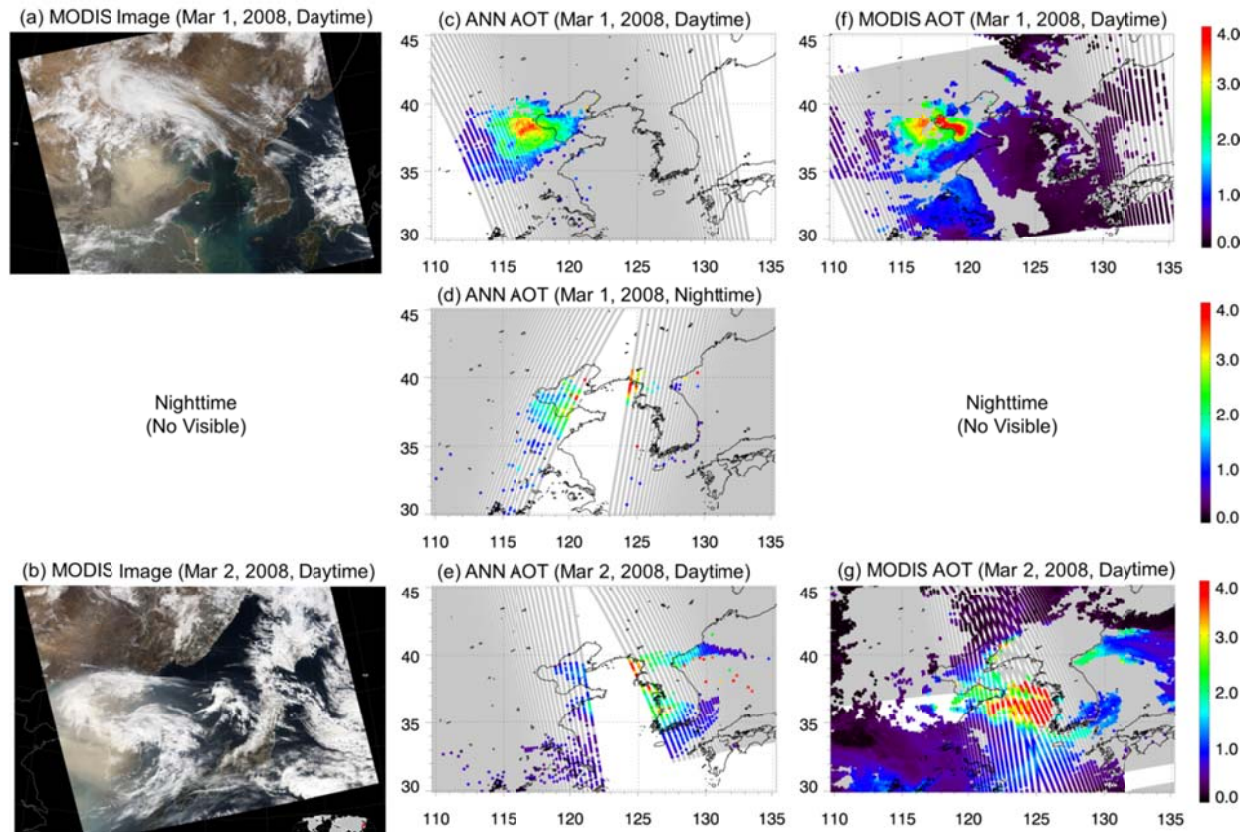


Figure 16. (a)–(b) MODIS true color images, (c)–(e) AOTs retrieved from AIRS measurements using the ANN model, and (f)–(g) MODIS-derived AOTs during 1 – 2 March 2008.

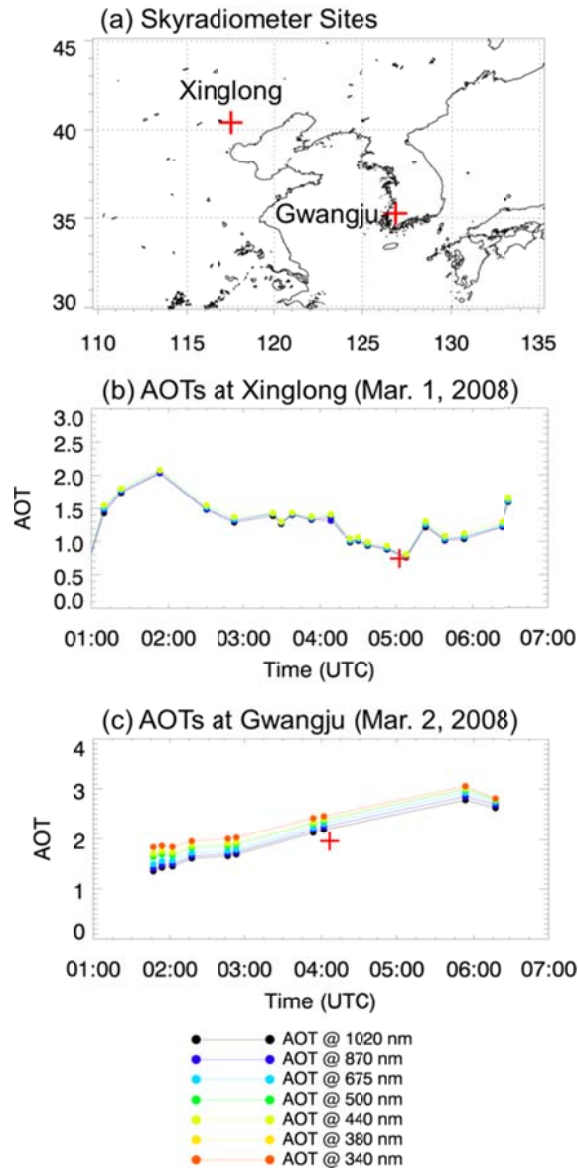


Figure 17. (a) Geographical locations of the two skyradiometer sites (Xinglong and Gwangju) of AERONET. Time series of AOTs observed by skyradiometers (a) at Xinglong on March 1, 2008 and (b) at Gwangju on March 2, 2008 are shown as closed circle. The AIRS-estimated AOTs for each site are plotted with red-cross marks in (b) and (c).

#### 4.5.2 April 17, 2009 case

Figure 18 shows the MODIS true color image, AIRS-retrieved AOT, and MODIS AOT distribution for the Asian dust outbreak that occurred on April 17, 2009 over the Taklimakan Desert area. In the true color image (Figure 18a), a bright yellowish dust area is clearly visible in the north of the Tibetan Plateau, which is located in the southern part of the image and is covered with broken clouds above its darker surface. AIRS pixel-based AOT retrievals (Figure 18b) show the presence of dust extending from southwest to northeast, with maximum AOTs up to 4.0 centered over the area around 39°N and 87°E (an eastern part of the Taklimakan Desert). General patterns and magnitudes shown in AIRS retrievals are quite similar to those found in MODIS AOTs based on the deep blue algorithm, although maximum areas and magnitudes are rather large. The MODIS deep blue algorithm detected weak AOTs north of about 43.5°N, where a clear area is seen on the MODIS true color image. Since CALIPSO measurements (Figure 18b) indicate that no dust is present north of 43.5°N (around an eastern tail of the Tien Shan mountain range), low AOT areas diagnosed by the deep blue algorithm are not likely to be dust-related. A correlation coefficient of 0.86 obtained from collocated pixels between AIRS-derived AOTs and MODIS AOTs (not shown here) again indicates that the pixel-based results are consistent with results obtained from the validation of the ANN model (Figure 15a).

The two-dimensional distribution of the AIRS-derived  $z_{\text{dust}}$  data for this case is shown in Figure 19a, where the red solid line indicates the CALIPSO

along-track direction from south to north. A vertical view of CALIOP total attenuated backscatter at 532 nm is given in Figure 19b, along with collocated  $z_{\text{dust}}$  ('+') retrieved from AIRS measurements. Considering that the backscatters are included only if larger than  $5.0 \times 10^{-3} \text{ km}^{-1} \text{ sr}^{-1}$ , the close agreement shown in Figure 19b suggests that AIRS retrieval well represents the altitude of the dense dust layer. It is of interest to note that the lower  $z_{\text{dust}}$  ( $< 3 \text{ km}$ ) areas in Figure 19a roughly correspond to the lower desert basin area lower than 1000 m above sea level.

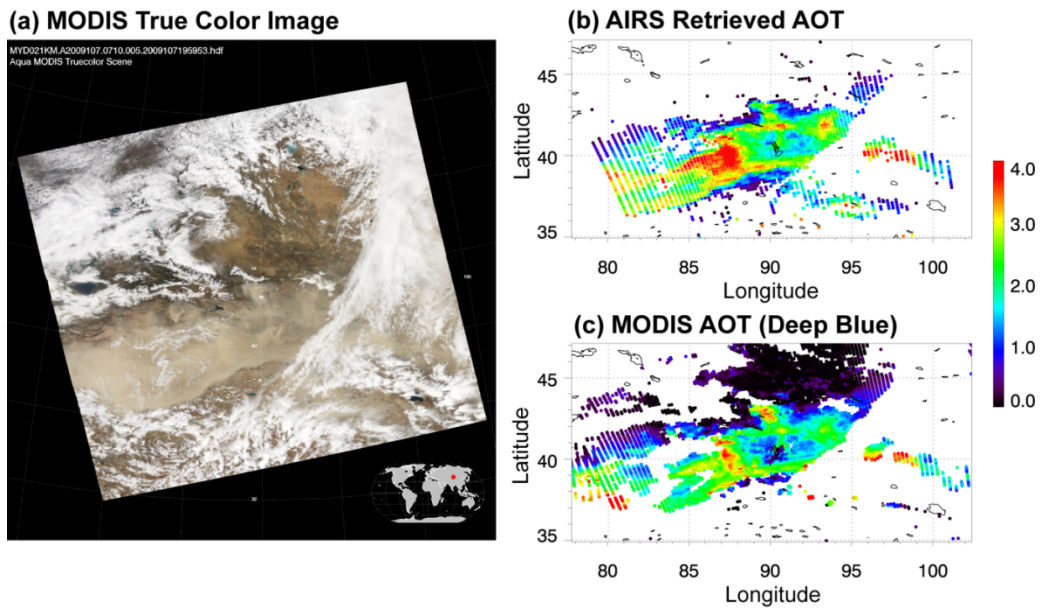


Figure 18. (a) MODIS true color image, (b) AOT retrieved from AIRS measurements, and (c) MODIS-derived AOT on April 17, 2009 over the Taklimakan Desert area.

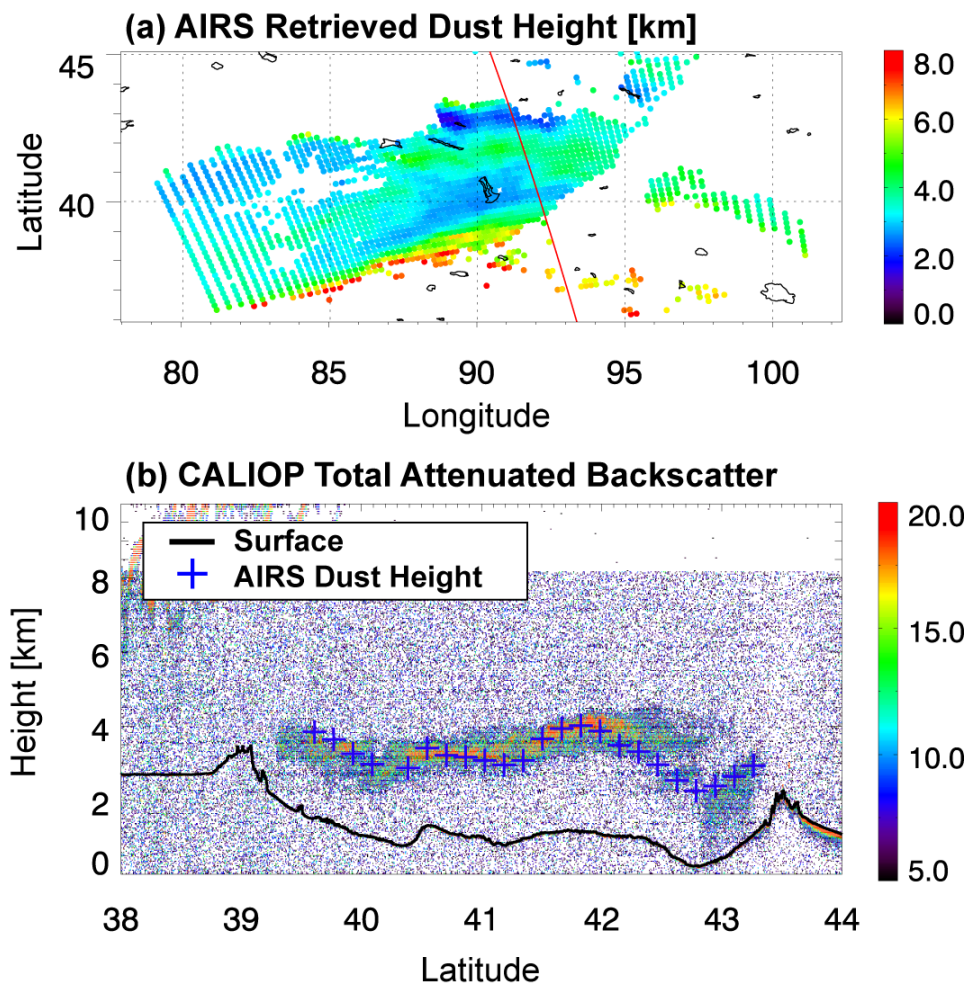


Figure 19. (a) Two-dimensional distributions of dust heights retrieved from AIRS measurements, and (b) vertical view of CALIOP-measured total attenuated backscatter at 532 nm on April 17, 2009 over the Taklimaken Desert area, along the CALIPSO track [red line in (a)]. The backscatter in unit of  $\text{km}^{-1} \text{sr}^{-1}$  are multiplied by 1000, and values smaller than  $5.0 \times 10^{-3} \text{ km}^{-1} \text{sr}^{-1}$  are masked out in (b).

### 4.5.3 April 23, 2009 case

AOT and  $z_{\text{dust}}$  for another dust outbreak, which occurred on April 23, 2009 over the Mongolian Gobi Desert, are retrieved from AIRS measurements and compared with MODIS AOT and CALIOP  $z_{\text{dust}}$  (Figures 20 and 21). In the MODIS true color image (Figure 20a), dust features are represented by a bright yellow color over the northwest of Shanxi Province (located in the southeast corner of the domain), likely following a low-pressure system causing a vortex-shaped cloud over the Gobi Desert. In the AIRS retrieval (Figure 20b), the high AOT area over  $42^{\circ}\text{N}$ ,  $109^{\circ}\text{E}$  appears to be in the vicinity of an area of vortex-shaped cloud. In this retrieval, because cloud screening is not done separately but by applying the algorithm of DeSouza-Machado et al. [2010] for determining the presence of dust, some cloud areas remain and are determined to be areas of dust; this results in high dust AOT in spite of the presence of cloud near the vortex center. It is interesting to observe a narrow dust band on the MODIS true color image, along the narrow zone off the Qinghai high-terrain area (located in the southwest quarter of the MODIS image domain). The narrow dust band, probably moving from the eastern Taklimakan Desert, is captured well by both AIRS and MODIS AOT. Again, at the pixel level, a high correlation coefficient of 0.88 between the two retrievals indicates that the ANN-based AIRS dust AOT values are comparable to those from the MODIS deep blue algorithm.

Two-dimensional distributions of the AIRS-derived  $z_{\text{dust}}$  for this case are shown in Figure 21a, and a comparison is made using the vertical profiles of

CALIOP-measured total attenuated backscatter along the track from south to north in Figure 21b (expressed as a red line in the Figure 21a). It is shown that CALIPSO-measured height distribution along the track is generally captured well by AIRS retrievals. However, overestimation is apparent over the high-terrain area around 38°N. Although it is not clear whether the complex terrain features give rise to this overestimation, it is not surprising to note that remote sensing over the high complex terrain area has been always problematic. A closer look suggests that the high attenuated backscatter region south of 37°N appears not to be related to dust presence, but to cloud (see the MODIS true color image). The dust layer is found to be substantially diffused vertically in comparison to the rather compact dust layer in the April 17 case (Figure 19b). By nature, because AIRS  $z_{\text{dust}}$  represents the layer mean AOT-weighted height, retrieval results may be more different to CALIOP measurements if the total dust layer is deeper or more diffused.

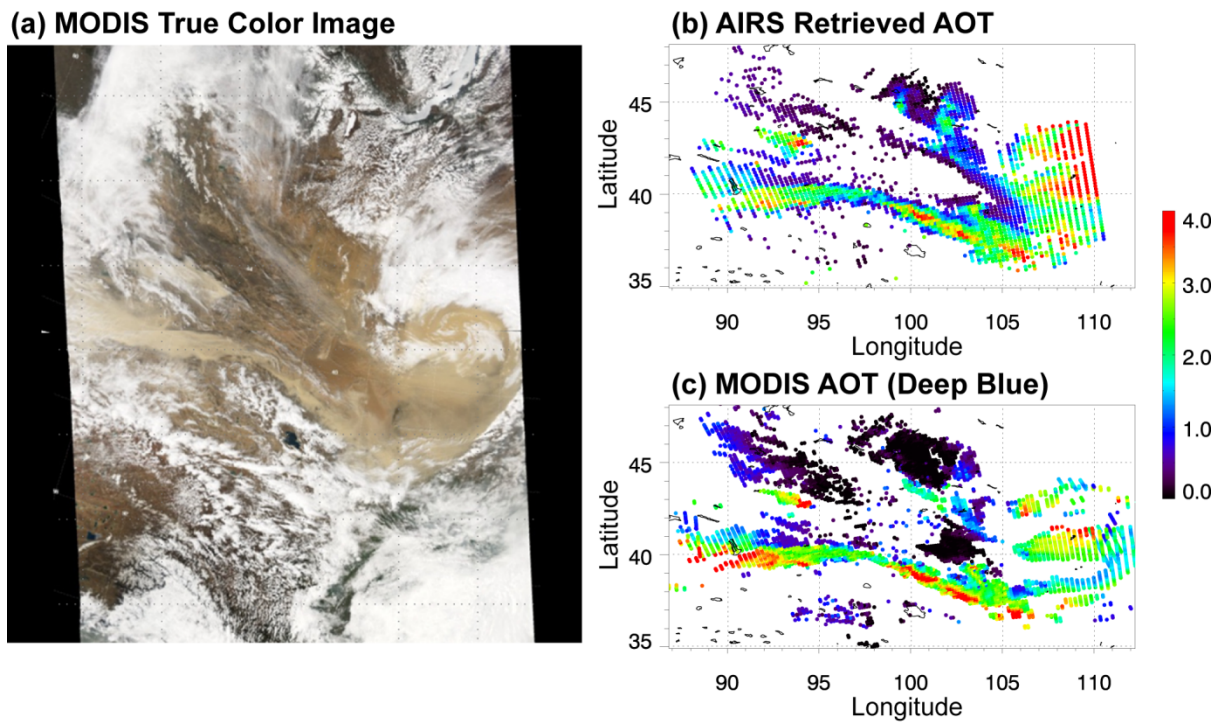


Figure 20. Same as Figure 18, except for the dust outbreak on April 23, 2009 over the Gobi Desert.

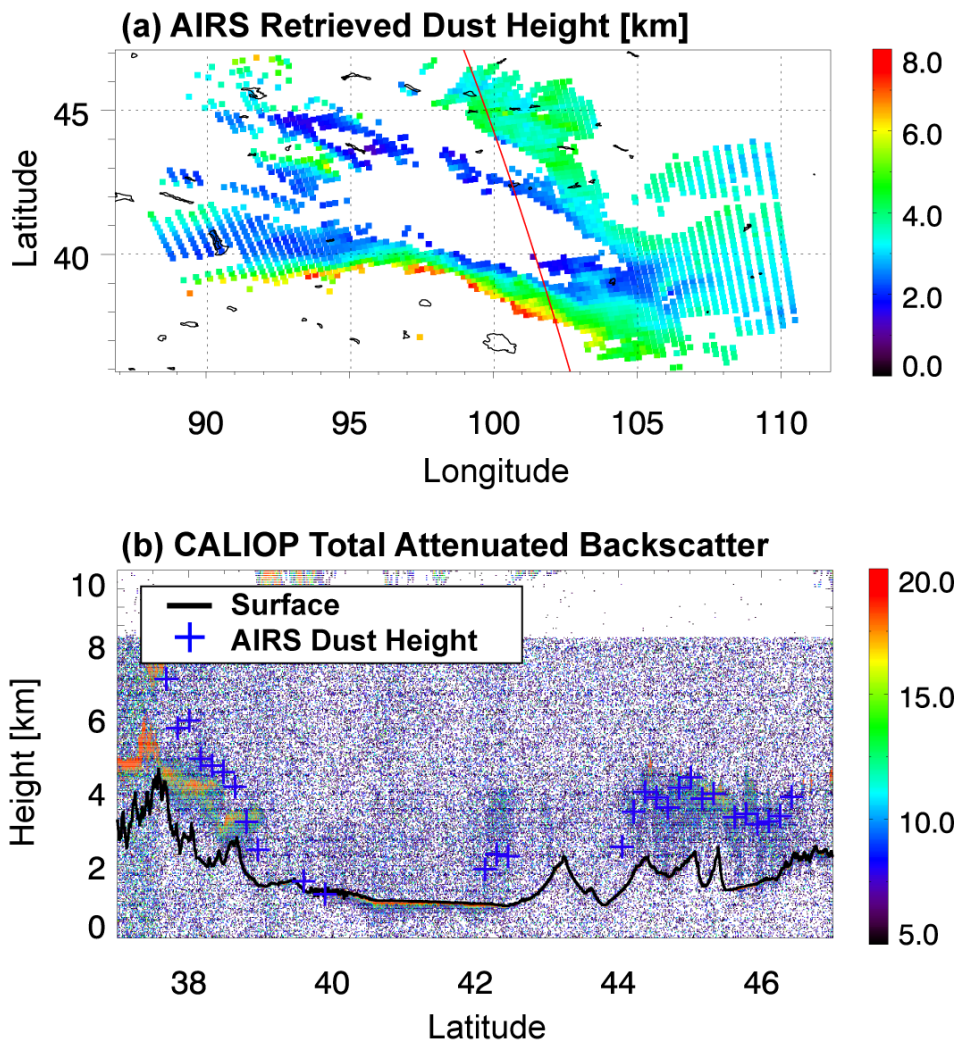


Figure 21. Same as Figure 19, except for the dust outbreak on April 23, 2009 over the Gobi Desert.

## 5. Simulation of dust impact on AIRS spectrum

A physical inversion method, contrary to statistical approaches, is more complicated to be constructed than a statistical approach. Nevertheless, the physical inversion method has an advantage of apparent physical meanings for all components of the algorithm, and thus it is possible to fully understand the retrieval processes which are not easy to understand from statistical retrieval approaches. As shown in section 4, AOT and  $z_{\text{dust}}$  are successfully retrieved using a statistical approach. The results demonstrate potential for retrieving AOT and dust heights from IR hyperspectral sounder measurements. Encouraged by the success, we make attempt to apply a physical inversion method to retrieve quantitative parameters of Asian dust, in addition to the statistical approach.

An electromagnetic signal is recorded by a detector after it interacts with a target containing molecules, particulates, and/or surfaces. For each target (or state)  $x$ , there is a corresponding ideal measured signal,  $y$ , determined by the light scattering and radiative transfer theories. We can describe the physics formally as the forward function  $f(x)$ ,

$$y = f(x) . \quad (5)$$

However, in practice not only is there always experimental error, but it is often necessary to approximate the detailed physics by some forward model  $F(x)$ . Therefore the relationship between the measurement and the state can be described as

$$y = F(x) + \varepsilon , \quad (6)$$

where  $y$  is the measurements with error  $\varepsilon$ , and  $F(x)$  is a vector valued function of the state, which encapsulates all understanding of the physics of the measurement. To construct a forward model for Asian dust retrieval, no less significant is the knowledge about scattering and absorptions induced by interactions between dust particles and IR light. Consequently, a better description of dust optical properties and accurate radiative transfer modeling are a prerequisite for aerosol retrieval.

### **5.1 Dust modeling for radiative transfer calculation**

The calculation of radiative transfer with aerosols is generally based on the Lorentz-Mie scattering calculation with prescribed aerosol optical properties. However, unlike in the VIS spectral range for which abundant measurements of optical properties are available [Patterson and Gillette, 1977; Levin et al., 1980; Hess et al., 1998; Dubovik et al., 2002; Myhre et al., 2003; Aoki et al., 2005], relatively few observations of IR dust optical properties are available in the literature [e.g. Volz, 1972; Volz, 1973; Hess et al., 1998]. Those observed refractive indices for dust have been routinely used for Asian dust studies [Gu et al., 2003; S.-W. Kim et al., 2004; Aoki et al., 2005; Zhang et al., 2006; Zhang et al., 2009]. Considering that the optical properties of dust depend on the mineralogical composition and thus on the dust source regions [Sokolik et al., 1998; Darmenov and Sokolik, 2005], it is of interest to examine how well the currently available optical properties can support our capability of radiative transfer modeling to simulate IR features associated with Asian dust. This type

of research is now possible because finer IR spectral signatures of the dust are routinely measured on satellite platforms, such as AIRS; furthermore, the vertical structures of the dust layer can be probed by satellite-borne active sensors, such as CALIPSO.

In this section, we aim to understand the impact of various aerosol properties and surface emissivity on the IR spectral features. The IR radiative transfer modeling is improved with optical and physical properties for Asian dust from skyradiometer measurements, various refractive indices, and the use of spatially and temporally varying surface spectral emissivity in a radiative transfer model. Then the simulations are compared with the AIRS TBs for validating the results. Even though we only focus on AIRS in this paper because of the availability of collocated CALIPSO data used for the radiance simulation, the obtained results should also be valid for other IR hyperspectral measurements.

## **5.2. Radiative transfer modeling**

In order to examine the performance of radiative transfer models for simulating the effects of Asian dust, we use aerosol size distributions obtained from ground-based skyradiometer measurements at Dunhunag located in the east of Taklimakan Desert of China, in conjunction with three different IR refractive indices for the mineral dust. The influence of surface emissivity on satellite measurements is also tested with monthly land surface emissivity data. Details of those inputs used for the modeling are found in sections 5.2.2.

### **5.2.1 Radiative transfer model**

RTTOV (Version 9.3) model is used for simulating TOA radiances. The RTTOV model was designed for fast calculation of radiances measured by space-borne IR and microwave sensors viewing the atmosphere and surface [Saunders et al., 1999; Saunders et al., 2010]. For the simulation of TOA radiances including aerosols, it employs 10 aerosol components from the Optical Properties of Aerosols and Clouds (OPAC; Hess et al., [1998]) database plus a volcanic ash component (total 11 components) to allow mixing of the various aerosol components. Any specific aerosol is thus described through a mixture of the necessary species from these 11 components.

The OPAC database describes four components of mineral aerosols, nucleus mode, accumulation mode, coarse mode, and mineral-transport mode. Those four mineral aerosol components are assumed to have the same refractive index, but different size distributions [Hess et al, 1998]. The refractive index of mineral aerosol is from various sources (i.e., Volz [1973], Patterson and Gillette, [1977], Levin et al., [1980], and quartz absorption features [Schütz, 1979]). The size distribution parameters from d'Almeida [1989] and Schütz [1979] are used to describe aerosols over deserts [Köpke et al., 1997]. Those refractive indices and size distributions are mainly from observations over North African Deserts, and partly from arid areas of the U.S. and the Middle East. Considering that mineralogical compositions and their optical properties exhibit a strong regional dependency [Claquin et al., 1999; Darmenov and Sokolik, 2005], it may be

worthwhile to test if they are suitable (or which is more suitable) for better describing the radiative effect pertinent to Asian dust.

TOA radiances except strong gas absorption bands should be sensitive to the surface emissivity because of the transmission of surface-emitted radiance to the TOA radiance through the transparent or semi-transparent atmosphere. Moreover Asian dust sources are located in Chinese and Mongolian arid regions. The dust is transported across large distances, over widely varying surface types with different emissivity properties. Because the default configuration of RTTOV assumes the emissivity over land to be a fixed value of 0.98, we used a land surface emissivity atlas (see section 5.2.3) to account for the spectral, spatial, and temporal variability of this parameter in our simulations. For sea surfaces, we used the RTTOV default routine (ISEM-6), which calculates the ocean surface emissivity analytically as a function of the wavelength.

### **5.2.2 Dust modeling and improved Lorentz-Mie calculation**

The scheme implemented in RTTOV to parameterize aerosol scattering is based on methodology of Chou et al. [1999]. This scheme (referred to as the scaling approximation) approximates the effect of scattering by scaling the optical depth by a factor derived by including the backward scattering in the emission of a layer and in the transmission between levels. This parameterization relies on the hypothesis that the diffuse radiance field is isotropic and can be approximated by the Planck function which allows the

radiative transfer equation to be formulated in the same way as for clear sky conditions. In the scaling approximation the contribution of the thermal diffuse scattered radiation is simulated by replacing in the radiative transfer equation the absorption optical depth,  $\tau_a$ , with an effective extinction optical depth,  $\tau_e$ , defined as:

$$\tau_e = \tau_a + b\tau_s \quad (7)$$

where  $\tau_s$  is the scattering optical depth and  $b$  is the integrated fraction of energy scattered backward for incident radiation from above or below. More details about the actual implementation in RTTOV are given in Matricardi [2005].

It has been known that IR extinction process caused by dust aerosols is better explained by the inclusion of nonsphericity of dust particles in the Mie calculation (e.g. Hudson et al., [2008]; Klieber et al., [2009]). However, because its non-spherical effect is small over IR spectral range [Yang et al., 2007], we generate the necessary parameters (i.e., absorption and scattering coefficients, single-scattering albedo, and phase function) for the assumed spherical dust particles using the Lorentz-Mie theory. The size distribution for Asian dust is obtained from sky radiometer measurements (Figure 22). Three different refractive indices for mineral aerosol [i.e., mineral component from OPAC database, dust-like component based on the measurements of Volz [1972, 1973] [Shettle and Fenn, 1979], and quartz from the High Resolution Transmission (HITRAN) database [Rothman et al., 2009] (hereafter referred to as OPAC, Volz, and HITRAN, respectively)] are used for examining the impact

of different refractive indices on TOA radiances. The backscattering parameter,  $b$ , in equation (7) is then calculated from the phase function obtained using a code provided by the European Centre for Medium-Range Weather Forecasts (ECMWF) [personal communication with Dr. Marco Matricardi at ECMWF]. Optical parameters obtained from the above calculations are then included in RTTOV for the dust affected radiance simulations.

### ***Size distribution of Asian dust***

Skyradiometers (e.g. POM-01; Prede Co. Ltd.) measure direct and diffuse solar radiation at seven wavelengths of 315, 400, 500, 675, 870, 940, and 1020 nm, and then aerosol optical thickness (AOT), single-scattering albedo, Ångström exponent, and volume size distribution are retrieved from the measurements by applying an inversion technique developed by Nakajima et al. [1996]. Size distributions for Asian dust retrieved from sky radiometer measurements at Dunhuang, China, are used for the Lorentz-Mie calculation. The Dunhuang site (40.146°N, 94.799°E) is located at the eastern edge of the Taklimakan Desert where Asian dust emission takes place all year, and thus the obtained optical properties at this site should represent the properties of Asian dust (e.g. D.-H. Kim et al., [2004]). Measured data are obtained from the skyradiometer network (SKYNET) data center in Chiba University of Japan (available at <http://atmos.cr.chiba-u.ac.jp/>). The size distribution representing Asian dust is obtained by taking an average of all available dust measurements over a nine-year period (October 1998–January 2007) selected by applying pre-determined dust indices (i.e., AOT at 550 nm  $\geq$  0.5, Ångström exponent  $\leq$

0.3 [Lee et al., 2002]). Retrieved size distributions are given in Figure 22a in terms of number density versus particle radius.

Since the sky-radiometer-derived size distribution for the Asian dust also includes contributions by other types of aerosol, we combine three modes for mineral aerosol components (i.e., nucleus, accumulation, and coarse modes) from the OPAC database [Hess et al., 1998] to best fit the mean size distribution from the sky radiometer measurements. The number mixing ratios for nucleus, accumulation, and coarse modes are 0.862, 0.136, and  $0.217 \times 10^{-2}$ , respectively. The best-fit result (thick solid line) is given in Figure 22b along with the three OPAC modes centered at a radius of 0.07, 0.39, and 1.90  $\mu\text{m}$ , respectively. It is shown that the measured distribution is well fitted with three modes in the case of particles larger than 0.1  $\mu\text{m}$  in radius, while particles smaller than 0.1  $\mu\text{m}$  noted in the skyradiometer-retrieved distribution are likely erroneous. The large variations shown by particles smaller than 0.1  $\mu\text{m}$  in Figure 22a strongly suggest that sky radiometer measurements are not suitable for retrieving optical properties for particles smaller than 0.1  $\mu\text{m}$  (so-called nanoparticles). In this study, the size distribution depicted by the best-fit curve is used for generating the optical properties of Asian dust.

### ***Refractive indices of dust***

Refractive index is an important parameter that controls the optical properties of dust particles and, thus, the radiative signature of dust. We employ and test three different refractive indices ( i.e.: OPAC, Volz, and HITRAN). The refractive indices of OPAC and Volz have been commonly used to simulate dust

impacts or retrieve dust properties from measured IR spectra [Sokolik, 2002; DeSouza-Machado et al., 2010; Peyridieu et al., 2010]. The refractive index of quartz from HITRAN is also tested because quartz is one of the major components of Asian dust [Jeong, 2008]. The real and imaginary parts of the three refractive indices are given in Figure 23. Generally, larger absorption can be expected from OPAC in comparison to Volz over most of the IR spectrum. A more fluctuating feature is obvious for HITRAN, suggesting very large absorption near 9  $\mu\text{m}$  and a smaller absorption near 12.5  $\mu\text{m}$ . OPAC depicts absorption peaks near 9 and 12.5  $\mu\text{m}$ , similar to HITRAN but with a flat distribution.

### ***Extinction coefficients***

The IR extinction coefficients are calculated with the three different refractive indices for the Asian dust size distribution given in Figure 22b. In Figure 24, the extinction coefficient of OPAC shows a minimum value of  $1.7 \times 10^{-4} \text{ km}^{-1}$  near 8  $\mu\text{m}$ , and a maximum of  $4.9 \times 10^{-4} \text{ km}^{-1}$  at around 9.5  $\mu\text{m}$ . HITRAN appear to be quite similar to OPAC, except for spectral regions around 7–9  $\mu\text{m}$  and near 12.5  $\mu\text{m}$ , where HITRAN shows distinct peaks. The extinction coefficient of Volz seems to follow a similar pattern to OPAC, although the magnitudes are generally smaller than the others, showing values between  $1.2 \times 10^{-4}$  and  $3.5 \times 10^{-4} \text{ km}^{-1}$  over the IR spectral region. Volz shows a relatively smoother distribution of the extinction efficient. It is expected that the simulated spectrum using HITRAN may show significantly different features from OPAC or Volz because of the strong extinction coefficient near 8.5  $\mu\text{m}$ .

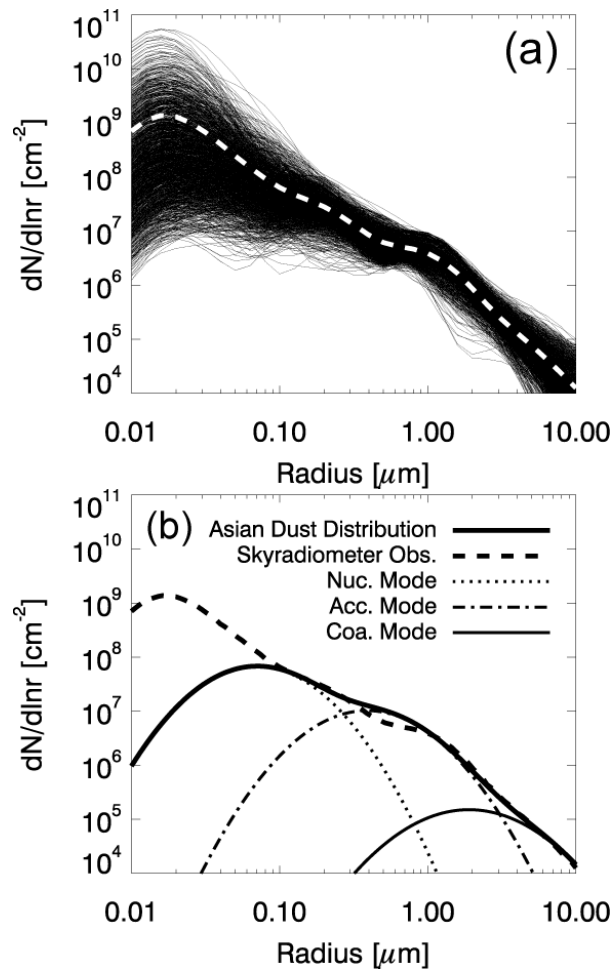


Figure 22. (a) Size distributions of Asian dust retrieved from sky radiometer measurements at Dunhuang, China (thin solid lines), and the mean size distribution (white dashed line). (b) Mean size distribution from the sky radiometer measurements (thick dashed line), three modes for mineral dust components from OPAC (nucleus mode: Nuc, accumulation mode: Acc, and coarse mode: Coa), and the best fit for the mean size distribution (thick solid line).

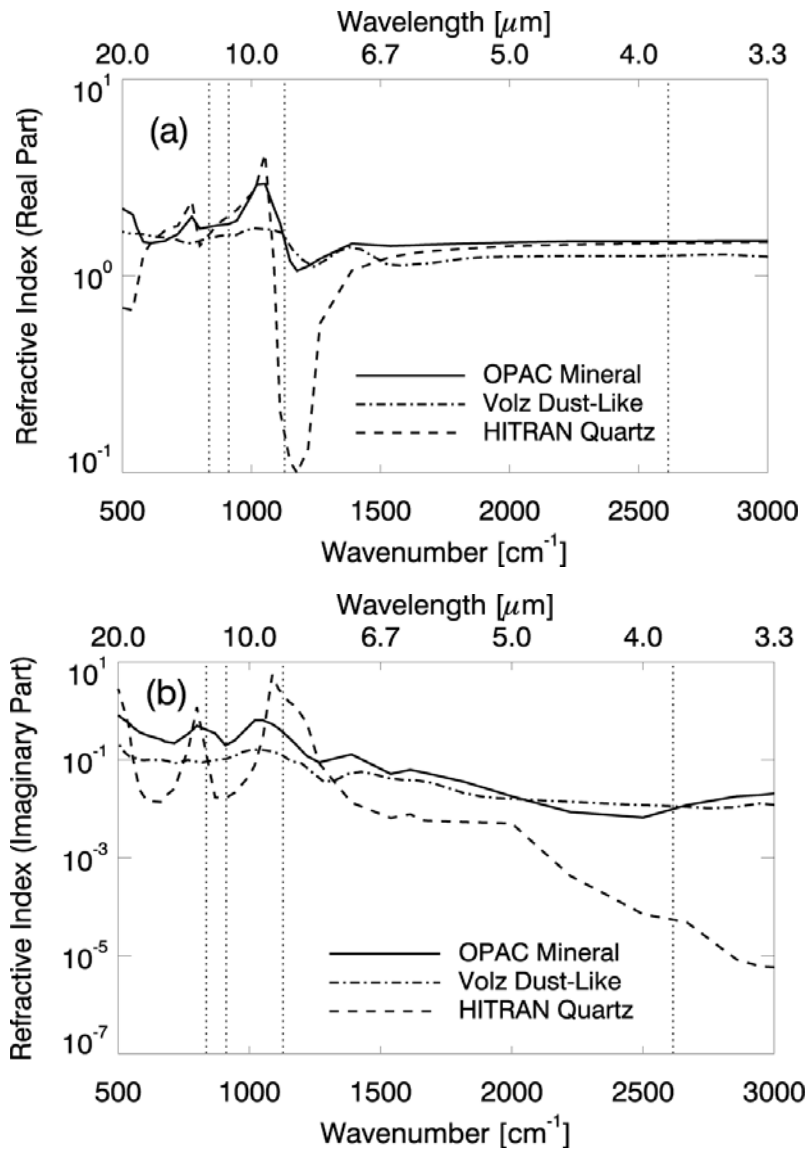


Figure 23. (a) Real and (b) imaginary parts of the refractive indices for OPAC mineral aerosol component (solid line), Volz dust-like aerosol (dashed-dot line), and HITRAN quartz (dashed line). The vertical dashed lines depict the spectral locations of four channels (ch770; 11  $\mu\text{m}$ , ch 565; 12  $\mu\text{m}$ , ch 1247; 8.9  $\mu\text{m}$ , ch 2330; 3.8  $\mu\text{m}$ ) used for the BTM calculation.

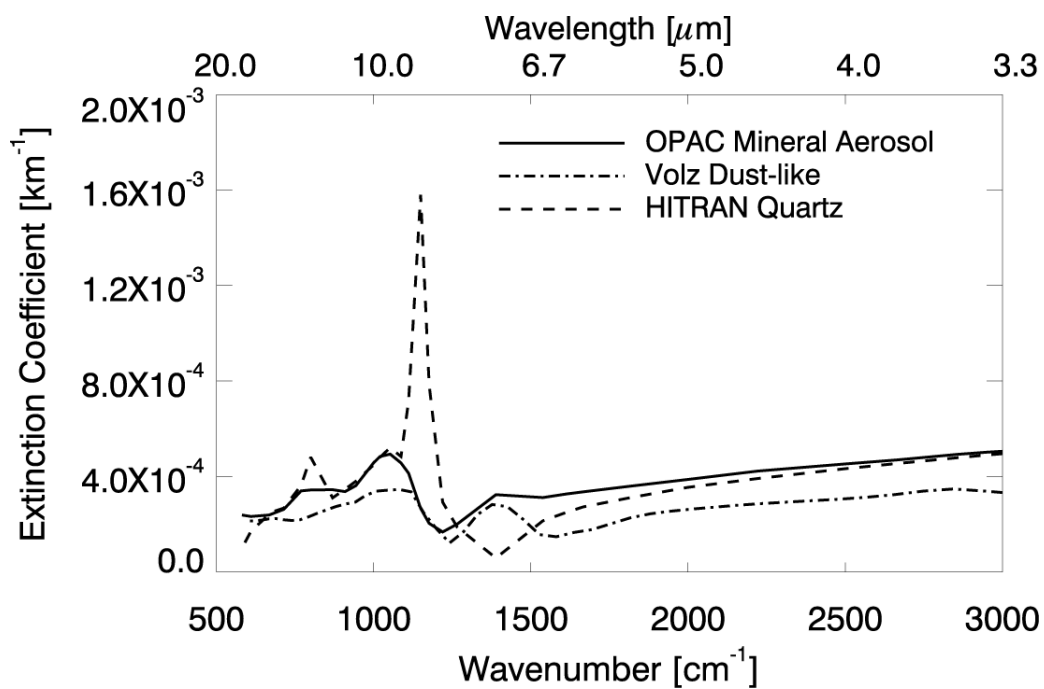


Figure 24. Extinction coefficients for the mineral aerosol component of OPAC (solid line), dust-like aerosol of Volz (dashed-dot line), and HITRAN quartz (dashed line) over the IR region. The coefficients are calculated with the given Asian dust size distribution of Figure 22.

### 5.2.3 Surface emissivity

In this study we specify the surface emissivity using the global IR surface emissivity data produced by the University of Wisconsin/Cooperative Institute for Meteorological Satellite Studies (UW/CIMSS) [Borbas et al., 2007; Seemann et al., 2008; available at <http://cimss.ssec.wisc.edu/iremisis/>], which were derived from the baseline fit method and principal component analysis regression. A conceptual model for a baseline fit is developed on the basis of high spectral resolution laboratory measurements (i.e., the Moderate Resolution Imaging Spectroradiometer (MODIS)/University of California, Santa Barbara (UCSB) (<http://www.ices.ucsb.edu/modis/EMIS/html/em.html>) and Advanced Spaceborne Thermal Emission and Reflection Radiometer (ASTER) emissivity libraries [Salisbury and D’Aria, 1994; Baldrige et al., 2009]) with 10 hinge-point wavelengths (3.6, 4.3, 5.0, 5.8, 7.6, 8.3, 9.3, 10.8, 12.1, and 14.3  $\mu\text{m}$ ) to capture the spectral shape between 3.6–15  $\mu\text{m}$  (Seemann et al. 2008). We use the land surface emissivity produced each month with a  $0.05^\circ$  spatial resolution at 416 wavenumbers over the IR spectral range, allowing for climatological seasonal variations of the surface emissivity [Borbas et al., 2007]. The latest version of RTTOV (Version 10.1) includes this global IR emissivity atlas as part of the package. Over the ocean, we use the emissivity computed from the Infrared Surface Emissivity Model (ISEM)-6 [Sherlock, 1999] which is part of RTTOV.

### 5.3 AIRS spectral radiance simulations

In order to test the performance of the radiative transfer model, we simulate AIRS TOA radiances using RTTOV with a specification of the dust vertical profile using CALIPSO aerosol products. The level 2 aerosol layer product used in this study contains the top and base altitude of the dust layer, AOT, and feature classification flag of each detected aerosol layer. Dust pixels and associated properties are obtained only if the CALIPSO pixel is determined to be dust-loading and CALIPSO AOT at 532 nm (hereinafter AOT532) is greater than 0.1. This is because  $AOT_{532} < 0.1$  is considered to be dominant in background aerosol. Dust profiles are discarded if CALIPSO level 2 data indicate cloud contamination.

Atmospheric temperature and moisture profiles are also used as inputs to the radiative transfer model. Six-hourly (e.g. 0000, 0600, 1200, and 1800 UTC) temperature, moisture, and ozone profiles are obtained from the ECMWF Reanalysis (ERA)-Interim data, which are given at fixed 37 pressure levels (1000, 975, 950, 925, 900, 875, 850, 825, 800, 775, 750, 700, 650, 600, 550, 500, 450, 400, 350, 300, 250, 225, 200, 175, 150, 125, 100, 70, 50, 30, 20, 10, 7, 5, 3, 2 and 1 hPa) in a  $1.5^\circ \times 1.5^\circ$  grid format [Dee et al., 2011]. Surface variables (skin temperature, surface temperature, surface dew point temperature, and surface pressure) are also extracted from ERA-Interim data.

For the simulation, AIRS observations are collocated with the vertical profile of dust from CALIPSO measurements, and with surface and atmospheric conditions of ERA-Interim data. In doing so, ERA-Interim data are

interpolated temporally into the AIRS observation timeline using the two closest analysis times, and spatially to the pixel location of interest using surrounding data points. Since CALIPSO and Aqua satellites show about a two minute time difference in the overpass, both measurements at the nadir view are considered to be collocated. However, because the spatial resolutions of AIRS and CALIPSO are 13.5 km and 5 km at nadir, respectively, all CALIPSO aerosol measurements within each AIRS pixel are averaged to construct collocated CALIPSO and AIRS measurements. Total 16,387 AIRS - CALIPSO collocated pairs were constructed over the two-year period (January 2008–December 2009) in the region 15°N–55°N, 70°E–150°E (i.e., over East Asia). CALIPSO dust information and collocated ERA-Interim temperature, moisture, and ozone profiles, and surface variables are used as inputs to the RTTOV model. Only nighttime simulations are performed, because diurnal variations of surface variables, such as the skin temperature, are much larger during the daytime and thus it is more difficult to resolve the expected diurnal variation during the daytime by simple interpolation. ECMWF surface pressure is used for defining the vertical extent of the atmospheric column at a given geographical location.

#### **5.4. Comparisons with observations**

We first simulated AIRS radiances using the RTTOV-9.3 model without any modifications, employing the OPAC optical parameters of dust described in section 5.2.1. In this step, the mineral coarse mode is selected and a fixed land

surface emissivity (0.98) is used. The results are taken as a reference for comparison with results from the improved simulations developed in this study. The AIRS radiances affected by dust are simulated using ERA-Interim surface and atmospheric variables and CALIPSO-derived AOT532 with dust top and bottom heights as inputs to RTTOV. The simulations are performed for the total 16,387 AIRS field-of-views, which are collated with CALIPSO measurements.

Comparisons are made between simulated and observed TBs in the scattergrams given in Figure 25 with associated statistics (correlation coefficient, mean bias, and root mean square error). AIRS has over two thousand channels, however, because the window channels are much more sensitive to dust than other gaseous absorption channels, we chose only four window channels (channel numbers 770, 565, 1247, and 2330 corresponding to 11, 12, 8.9, and 3.8  $\mu\text{m}$  spectral bands, respectively) for the scattergram comparison. The TBs at those channels are referred to as TB11, TB12, TB8.9, and TB3.8, respectively. The dashed line in each diagram represents a best fit regression line.

In Figure 25, all simulations of the four window channels demonstrate good agreement with observations, as shown by high correlation coefficients around 0.97. Regression equations suggest a similar pattern for all 4 channel simulations. However, mean biases for TB8.9 and TB3.8 appear to be larger than for TB11 and TB12; mean biases for the TB11, TB12, TB8.9, and TB .8 channels are 0.54, 0.05, 1.5, and 1.9 K, respectively. RMSEs of the simulations

are in the order of 3–4 K, although TB8.9 and TB3.8 show slightly larger RMSEs.

Although there is a good agreement of the simulations with observations as shown in Figure 25, it is still not clear whether the influence of the dust is properly simulated. The BTD using the 11, 12, 8.5, and 3.8  $\mu\text{m}$  channel TBs is commonly used for detecting the presence of mineral dust in the atmosphere [Ackerman, 1989; Ackerman 1997; Darmenov and Sokolik, 2005]. In order to examine whether the modeling approach adopted in this study is capable of simulating the dust effect accurately, we compare the simulated BTDs with AIRS measured values, i.e.: TB11–TB12 (BTD<sub>11-12</sub>), TB8.9–TB11 (BTD<sub>8.9-11</sub>), and TB3.8–TB11 (BTD<sub>3.8-11</sub>).

Scatterplots of simulated versus measured BTDs are given in Figure 26. The BTD<sub>11-12</sub> shows a weak linear relationship with correlation coefficient, mean bias, and RMSE of 0.67, 0.86 K, and 0.49 K, respectively (Figure 26a). The simulated BTD<sub>8.9-11</sub> (Figure 26b) displays a much lower sensitivity with a wider spread extending to about –10 K of the measured BTD<sub>8.9-11</sub>. The comparison between observed TB11 and TB8.9 indicates that observed TB8.9 is always lower than observed TB11 and the low bias of TB8.9 seems to be larger for higher TB11 (not shown). On the other hand, a well-matched one-to-one correspondence is noted in the simulated results (not shown). Thus, the large discrepancy shown in BTD<sub>8.9-11</sub> (Figure 26b) is likely attributable to the use of a fixed surface emissivity in the simulation. The simulated BTD<sub>3.8-11</sub> are also compared with observations (Figure 26c). In general, simulated BTDs show a

relatively large positive bias of 1.36 K in comparison to the corresponding observed values. The correlation coefficient of 0.31 is low and the RMSE of 2.02 K is relatively large, suggesting that the RTTOV model may not reproduce the dust features observed in the combination of the 11 and 3.8  $\mu\text{m}$  channels.

Overall, as noted in the comparison of BTDs, the default dust optical properties and fixed land surface emissivity used in RTTOV should not be adequate for simulating Asian dust signals in IR measurements, especially for BTD. Poor agreement of the simulated BTDs for the 8.9 and 3.8  $\mu\text{m}$  channels suggest that the dust optical properties or land surface emissivity near 8.9 and 3.8  $\mu\text{m}$  used in the RTTOV as default are likely to be unrepresentative of real situations, and hence, the default values should be updated with more realistic values.

To examine the impact of the land emissivity on the simulation, the default value of 0.98 in RTTOV model is replaced by temporally and spatially varying UW/CIMSS surface emissivity data. The simulated BTDs are plotted against measurements in Figure 27. In the scatterplots, better agreement of the simulations with AIRS observations is clear, especially for  $\text{BTD}_{8.9-11}$  and  $\text{BTD}_{3.8-11}$ . For example, the almost random pattern of simulated  $\text{BTD}_{8.9-11}$  shown in Figure 26b now shows a linear relationship, with a correlation coefficient of 0.83. Better agreement is also visible in  $\text{BTD}_{3.8-11}$  as shown by the increased correlation coefficient from 0.31 to 0.61 (Figure 26c and 27c). The improvement of  $\text{BTD}_{11-12}$  is less as shown by only slightly improved statistics.

The improvement of  $\text{BTD}_{8.9-11}$  and  $\text{BTD}_{3.8-11}$ , demonstrates that specification of more accurate surface emissivity is crucial for improving simulations of dust-affected IR radiances, especially near the 8.9 and 3.8  $\mu\text{m}$  spectral bands. This improvement is particularly important because arid regions have relatively low and variable surface emissivity in the 3.5–4.5 and 8–10  $\mu\text{m}$  bands [Salisbury and D’Aria, 1992; Salisbury and D’Aria, 1994], and these are the bands we often use for monitoring dust storms. In the previous studies, dust has been monitored by using the BTB between two split window channels [J. Li et al. 2007] or using three window channels [Zhao et al. 2010]. Efforts have been made to relate the BTB to a quantitative measure of dust intensity [e.g. Zhang et al. 2006]. However, results obtained in this study strongly suggest that a robust simple BTB criterion may not be adequate because of strong influences of geographically and temporally varying emissivity on the TOA TB.

To test the impact of the assumed dust refractive index on the AIRS TB simulations the size distributions for Asian dust retrieved from the sky radiometer measurements (section 5.2.2(a)) are used for the simulations, together with OPAC and Volz refractive indices for mineral dust and the HITRAN refractive index for quartz given in Figure 23. For comparison, coarse mode and mineral-transported distributions are also included. While the coarse mode has a mode radius of 1.9  $\mu\text{m}$ , the size distribution for the transported component has a mode radius of 0.5  $\mu\text{m}$  [Hess et al., 1998]. The three simulations are based on a combination of the OPAC refractive index for mineral dust with three different size distributions (i.e., Asian dust, transported

mode, and coarse mode). In the simulations, moderate to strong dust cases showing collocated CALIPSO AOT532 > 0.5 are chosen in order to reduce the uncertainties arising from surface variables. Of total 16,387 AIRS-CALIPSO collocated data, 2,350 cases satisfying the criteria remain. Mean biases from the observations are presented over the two spectral regions in Figure 28 after taking the average of 2,350 simulations, and associated RMSEs for the 4 window channels (11, 12, 8.9, and 3.8  $\mu\text{m}$ ) are given in Table 3. Also plotted in Figure 28 are results from the use of different refractive indices for the given Asian dust size distribution.

It is shown that the size distribution from the coarse mode (OPAC-CO in Figure 28) only results in the largest underestimate, of up to  $-1.5$  K over most of the window region in the thermal IR band. Use of the OPAC transported mode and Asian dust distributions (i.e., OPAC-TR and OPAC-AD) give rise to significantly reduced TB differences by up to  $-1$  K. It is also clear that a noticeable improvement has been made by use of the Asian dust model throughout the thermal IR window region of interest (Figure 28a).

The impact of the three refractive indices for the Asian dust size distribution on the AIRS TB simulations shows that use of the Volz refractive index for mineral dust provides the best agreement with observations over the thermal window region. Note that the refractive index from the HITRAN quartz does not reduce the bias over the  $750\text{--}870$   $\text{cm}^{-1}$  region, probably because of the peak in the extinction coefficient of the HITRAN quartz over the same wavelength region of Figure 24. Standard deviations calculated from 2,350

cases at 4 channels show that seasonal and geographical fluctuations of the bias from the AIRS measurements are in the order of 2-3 K (Table 3). Consistent with the mean bias result, the combination of Volz refractive index with AD distribution (Volz-AD) yielded smallest standard deviations (2.4–2.5K) in general.

In contrast to the significant radiance differences in the longwave IR when particle size distribution and refractive index are varied, the shortwave IR window region ( $2400\text{--}2700\text{ cm}^{-1}$ ) in Figure 28b shows less sensitivity to both size distribution and refractive index. Different from smaller biases shown in the shortwave IR region the relative errors are much larger (2–4% of radiance) because of the smaller emitted radiant intensity over those bands (not shown). Larger relative errors suggest the difficulty of using shortwave IR channel measurements to monitor the dust features.

One might concern about influences of gas absorption due to uncertain input data (particularly due to uncertainties in water vapor profile). Sensitivity tests were conducted by allowing  $\pm 10\%$  of uncertainty in water vapor profiles. Results indicate that the uncertainly range caused by  $\pm 10\%$  error in the water vapor profile is within at most 0.1 K except some strong water vapor absorption bands (not shown). Since BTDs are between TBs at weak water vapor absorption bands, and  $\text{CO}_2$  and  $\text{O}_3$  absorptions should be much smaller there, obtained results from Figure 28 and others should be valid even if uncertainties in gas absorption exist.

By using the Asian dust size distribution, the Volz refractive index for the mineral dust, and the UW/CIMSS surface emissivity, three BTD distributions are calculated to show the improvement in simulations when compared to Figures 26 and 27. The results are given in Figure 29. All three BTDs show improved accuracy compared to those shown in Figures 26 and 27. It is concluded that amongst the available refractive indices for the dust, the use of the Volz refractive index gives the best performance when combined with the Asian dust size distribution and UW/CIMSS surface emissivity.

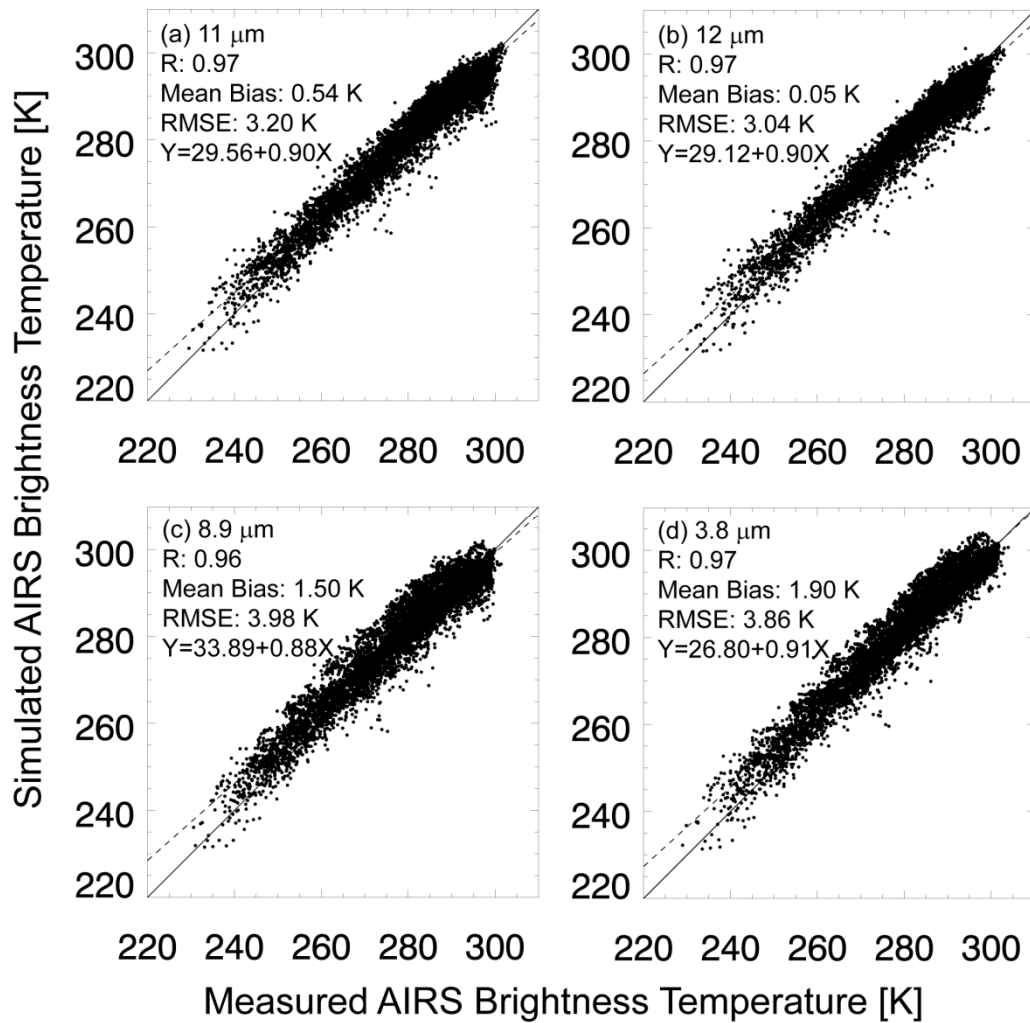


Figure 25. Scatter plots of simulated and measured AIRS  $T_{BS}$  for (a) 11  $\mu\text{m}$  (ch 770), (b) 12  $\mu\text{m}$  (ch 565), (c) 8.9  $\mu\text{m}$  (ch 1247), and (d) 3.8  $\mu\text{m}$  (ch 2330) with associated statistics. The  $T_{BS}$  are simulated with OPAC mineral aerosol refractive index and with OPAC mineral coarse mode size distribution. Dashed lines represent best fit regression lines.

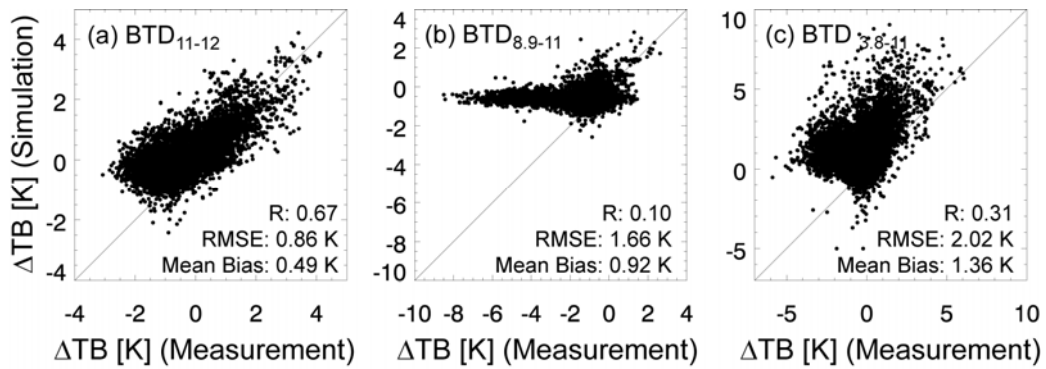


Figure 26. Scatter plots for simulated and measured (a) BTD<sub>11-12</sub>, (b) BTD<sub>8,9-11</sub>, and (c) BTD<sub>3,8-11</sub>. The T<sub>BS</sub> are simulated with OPAC mineral aerosol refractive index and with OPAC mineral coarse mode size distribution. The default land surface emissivity of 0.98 is used.

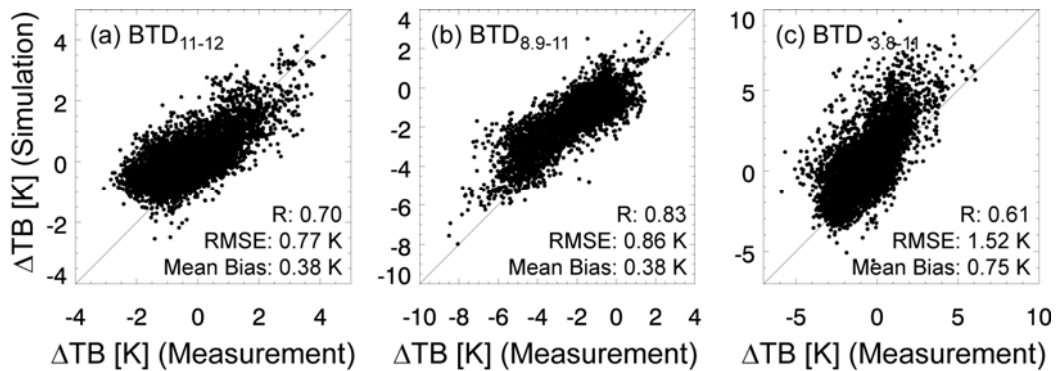


Figure 27. As Figure 26, except for the use of UW/CIMSS surface emissivity data.

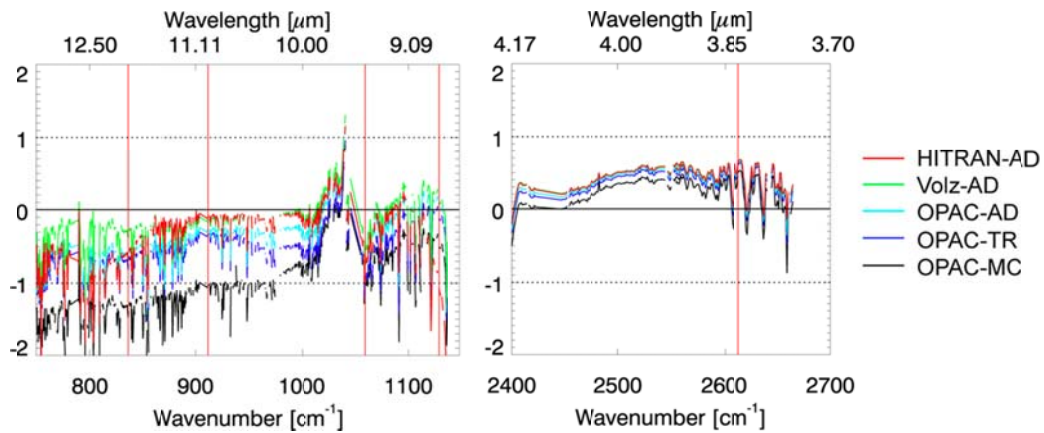


Figure 28. Mean bias (simulated  $T_B$  minus measured  $T_B$ ) for dust with CALIPSO AOT<sub>532</sub> > 0.5 for IR spectral bands (a) 750–1150  $\text{cm}^{-1}$  and (b) 2400–2700  $\text{cm}^{-1}$ . The  $T_B$ s are simulated with three refractive indices (OPAC: OPAC mineral aerosol component; Volz: Volz dust-like; HITRAN: quartz from HITRAN database) and with different dust-size distributions (AD: Asian dust size distribution; TR: mineral-transported in OPAC; CO: mineral coarse mode in OPAC). Surface emissivities over the land are specified by UW/CIMSS surface emissivity data. The vertical red lines indicate the four channels (ch 770; 11  $\mu\text{m}$ , ch 565; 12  $\mu\text{m}$ , ch 1247; 8.9  $\mu\text{m}$ , ch 2330; 3.8  $\mu\text{m}$ ) used for the BT-D comparison.

Table 3. Standard deviations of error of the simulated  $T_{BS}$  for AIRS-CALIPSO dust pixels if CALIPSO AOT532 > 0.5 (total 2350 cases).  $T_{BS}$  are simulated with three refractive indices (OPAC: OPAC mineral aerosol component; Volz: Volz dust-like; HITRAN: quartz from HITRAN database) and with different dust-size distributions (AD: Asian dust size distribution; TR: mineral-transported in OPAC; CO: mineral coarse mode in OPAC).

	11 $\mu\text{m}$ (ch 770)	12 $\mu\text{m}$ (ch 565)	8.9 $\mu\text{m}$ (ch 1247)	3.8 $\mu\text{m}$ (ch 2330)
HITRAN-AD	2.45 K	2.69 K	4.27 K	2.63 K
Volz-AD	2.50 K	2.38 K	2.46 K	2.51 K
OPAC-AD	2.67 K	2.68 K	2.72 K	2.62 K
OPAC-TR	2.75 K	2.81 K	2.89 K	2.70 K
OPAC-CO	3.63 K	3.52 K)	3.49 K	2.96 K

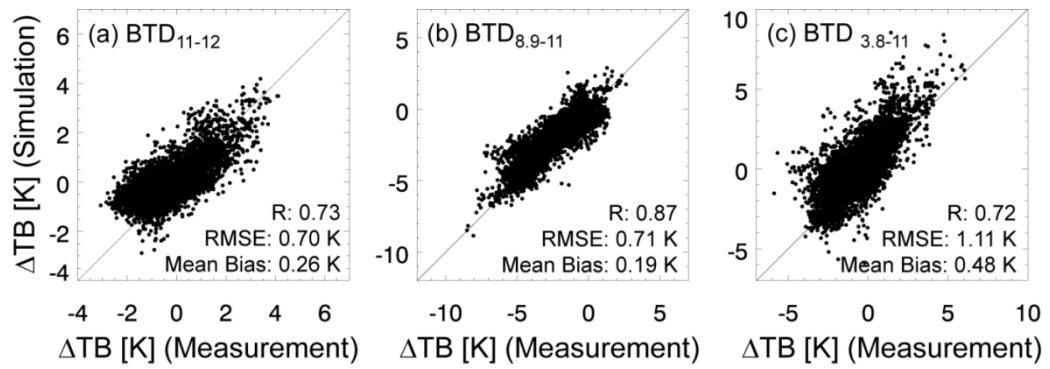


Figure 29. As Figure 26, except for the use of the Volz dust-like refractive index, the given Asian dust size distribution, and the UW/CIMSS surface emissivity data.

## 6. Dust retrieval using a physical method

### 6.1 Retrieval algorithm

Since IR radiance is contributed by the nonlinear combination of emissions from environmental state and dust particles, the measurement  $y$  and the dust state  $x$  exhibit highly nonlinear behavior. In the non-linear case, it may not be possible to obtain an explicit solution. The task in the nonlinear case is to find a best estimate  $\hat{x}$  and an error characteristic that describes the probability density function (PDF) well enough for practical purposes. If a Bayesian solution is described by a Gaussian PDF, then we obtain the conditional PDF of  $x$  given  $y$  [Rodgers, 1976],

$$-2 \ln P(x|y) = (y - F(x))^T S_\epsilon^{-1} (y - F(x)) + (x - x_a)^T S_a^{-1} (x - x_a) + c, \quad (8)$$

where  $P(x|y)$  is PDF of  $x$  given  $y$ ,  $F(x)$  is the nonlinear forward model in Equation (6),  $S_\epsilon$  is the measurement error covariance,  $S_a$  is the assumed background error covariance, and  $c$  is a constant. To find the maximum probability state  $\hat{x}$ , derivative of Equation 8 gives following implicit equation for  $\hat{x}$ ,

$$-\hat{K}^T(\hat{x}) S_\epsilon^{-1} [y - F(\hat{x})] + S_a^{-1} (\hat{x} - x_a) = 0, \quad (9)$$

where  $K(x) = \nabla_x F(x)$  represents the gradient of the forward model. For a general equation  $g(x) = 0$ , the iteration is analogous to Newton's method, and can be written,

$$x_{i+1} = x_i - [\nabla_x g(x_i)]^{-1} g(x_i). \quad (10)$$

Using the Newtonian iteration in Equation (10), iterative solution of Equation (9) is obtained as,

$$x_{i+1} = x_a + (S_a^{-1} + K_i^T S_\epsilon^{-1} K_i)^{-1} K_i^T S_\epsilon^{-1} [y - F(x_i) + K_i(x_i - x_a)] \quad (11)$$

where  $x_a$  is the background state,  $K_i = K(x_i)$ , and  $i$  is the iteration number. The retrieved vector is a weighted sum of the constraint by background and an inversion of the forward model ( $F^{-1}(y)$ ), with weightings determined by the background and measurement error covariance vectors. The background covariance  $S_a$  approaching zero implies that the background is an accurate estimate of the true parameters and the solution approaches the constraint. Conversely, as the background covariance is approaching infinity, the constraint is an inaccurate estimate of the true structure and the solution tends toward that specified by the inversion of the forward model.

The dust retrieval algorithm is based on the Newtonian iteration method (Equation (11)), and its details partly follow the design of Yao et al. [2012] from which AOT and top height of a dust layer are produced. The vector  $y$  in Equation (11) is the observed AIRS TBs for eleven channels described in section 6.2. The forward model,  $F$ , is constructed based on the simulation study in section 5 with the best combination of the dust optical properties and surface emissivity. The fast radiative transfer model, RTTOV-9.3, is used to dust affected AIRS spectra.

The measured IR spectrum is also strongly affected by atmospheric and

surface situations. Therefore, if all variables including surface temperature and atmospheric profiles are retrieved simultaneously with dust state, it is highly probable that the retrieval algorithm may become ill-posed and provide unstable products. In this study, the aim here is to retrieve only the effective dust height and density number (corresponding to AOT), and the surface and atmospheric states are known and thus remains constant while iteration.

Desouza-Machado et al. [2010] illustrate that the dust optical depth retrieval is less sensitive to the thickness of the dust layer than location of the dust layer. To reduce the retrieval uncertainty, the dust geometrical depth is set to 5 layers, which is about 1 km in the lower troposphere. The initial dust top is set to 617 hPa with an uncertainty of 0.1 hPa. The initial density number is set to  $2000 \text{ cm}^{-3}$ , which results in an optical depth of approximately 1.0 in the longwave IR band, with an uncertainty of  $2000 \text{ cm}^{-3}$  empirically. The TB uncertainty from the model and observation is assumed to be 0.5 K at each selected channel. The optical depth at each channel could be calculated in the RTTOV-9.3 from the retrieved density number. As with Peyridieu et al. [2010] and DeSouza-Machado et al. [2010], the  $10.4 \text{ }\mu\text{m}$  wavelength, which roughly corresponds to the maximum of the IR emission from Earth and the absorption of the dust, is chosen therein as the reference wavelength for IR optical depth.

## **6.2 Channel selection**

It is well known that the physical retrievals strongly depend on the accuracy of the forward model for selected channels. Significant differences

between observed and simulated TBs could be caused by the differences in dust composition, which could strongly depend on regions [Claquin et al., 1999; Sokolik, 2002]. Therefore, the channels selected for the physical retrieval should be well simulated with the use of available information on dust composition over any particular area.

The simulation study in section 5 shows that differences between the simulated and observed TBs are less than 0.5 K in the 10.2–11.5  $\mu\text{m}$  band when the dust effect is taken into account. Moreover, results of ANN model in section 4 demonstrated that IR WIN channel measurements carry information on dust AOTs, and that addition of the CO<sub>2</sub> channels can improve  $z_{\text{dust}}$  retrieval from hyperspectral sounder measurements. Consequently, eleven thermal channels in WIN and CO<sub>2</sub> band as listed in Table 4 are used to retrieve dust height and IR optical depth. These channels with different surface transmittance could benefit the retrievals due to their different sensitivities to dust at different levels. Although the shortwave IR channels could provide more information on the dust optical depths, the smaller signal-to-noise ratio makes it difficult to use those channels for meaningful retrieval, beside influences of solar contamination during the day time. Moreover, the use of only longwave channels in the retrieval could guarantee the consistency of the retrievals both day and night.

Table 4. AIRS selected channels number, wavenumber, wavelength, and surface transmittance simulated using the tropical atmospheric profile in RTTOV 9.3.

Channel number	Wavenumber ( $\text{cm}^{-1}$ )	Wavelength ( $\mu\text{m}$ )	Surface transmittance
205	708.133	14.122	0.000
312	739.441	13.524	0.002
382	761.881	13.125	0.143
671	870.792	11.484	0.276
672	871.114	11.450	0.157
673	871.436	11.475	0.315
676	872.404	11.463	0.521
914	965.215	10.360	0.636
924	969.222	10.318	0.621
929	971.237	10.296	0.432
933	972.856	10.279	0.532

### **6.3 Meteorological model**

For the dust retrieval, the atmosphere and surface states are assumed to be known parameters, and taken from the Regional Data Assimilation and Prediction System (RDAPS) provided by KMA. As an operational weather forecasting system in Korea, RDAPS focuses on the East Asian region as shown in Figure 30. The system is based on the fifth-generation Mesoscale Model (MM5), which is a limited-area, nonhydrostatic or hydrostatic, terrain-following sigma-coordinate model designed to simulate or predict mesoscale and regional-scale atmospheric circulation [Grell et al., 1994; Dudhia et al., 1998]. Atmospheric temperature and moisture profiles obtained from RDAPS are used as inputs to the radiative transfer model, which are given at fixed 19 pressure levels (1000, 950, 900, 850, 800, 750, 700, 650, 600, 550, 500, 450, 400, 350, 300, 250, 200, 150, and 100 hPa) for every 3 hours (e.g. 0000, 0300, 0600, 0900 1200, 1500, 1800, and 2100 UTC) with 27 km horizontal resolution. Skin temperature, surface temperature, surface moisture, and surface pressure are also extracted to define surface condition.

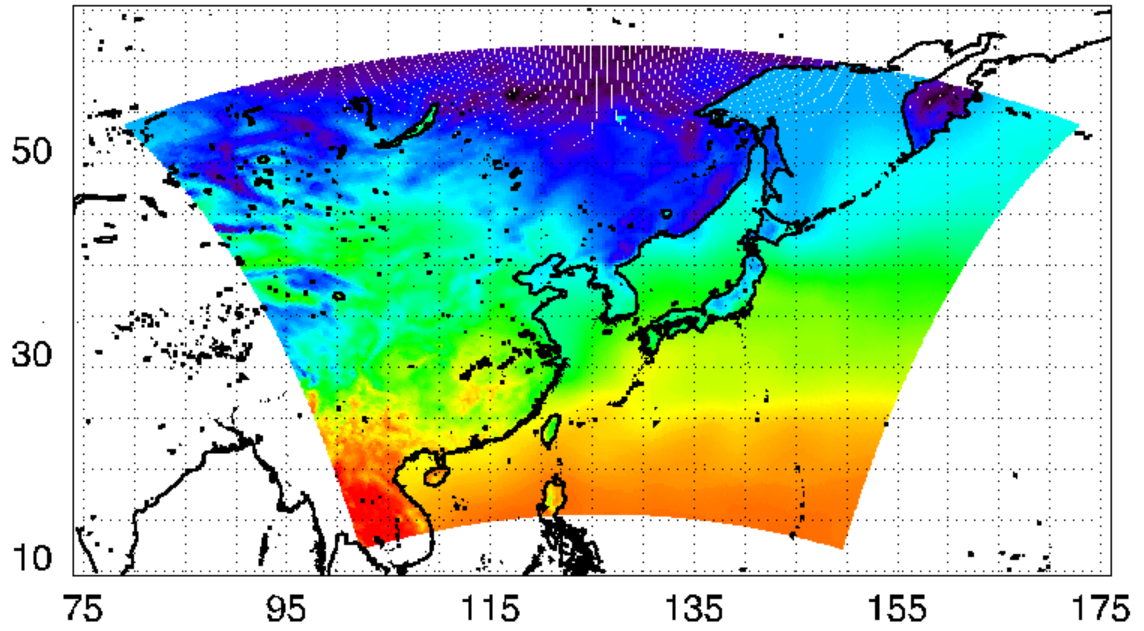


Figure 30. An example of skin temperature distribution obtained from RDAPS dataset showing the model domain.

## 6.4 Results

Using the developed physical retrieval algorithm, four dust cases were retrieved and analyzed in detail. We mainly focused on dust storms in the source region, because information on rising dust plumes, such as loading and height, is a critical factor in dust forecasting. Only dust-laden AIRS FOVs determined from the DDA method were used for the retrieval.

### 6.4.1 February 29, 2008 case

An intense dust outbreak occurred in the Gobi Desert on February 29, 2008. The associated MODIS true color image, scattergram, AIRS IR AOT retrieved from the physical algorithm, and MODIS AOT based on the deep blue algorithm are presented in Figure 31a–31d. A bright yellow dust storm is shown in the MODIS true color image (Figure 31a), though it is partly covered by widespread clouds. A scatterplot illustrating the relationship between the IR AOTs retrieved from AIRS and the VIS AOTs from MODIS is presented in Figure 31b. A correlation coefficient of 0.96 obtained from the collocated AOTs indicates the AIRS-derived IR AOTs are well correlated with the MODIS AOTs. The slope of the linear regression is about 0.34, which is comparable to the ratio of 0.31 reported by Pierangelo et al. [2004] for Sahara dust, but is slightly higher than the ratio of 0.05–0.25 of DeSouza-Machado et al. [2010] and the 0.23–0.29 of Yao et al. [2012], and lower than the 0.43 of DeSouza-Machado et al. [2006]. The horizontal distribution of pixel-level AOTs shows that the dust areas detected by AIRS in Figure 31c are consistent with the MODIS AOT

distribution in Figure 31d, indicating dust extending from northwest to southeast.

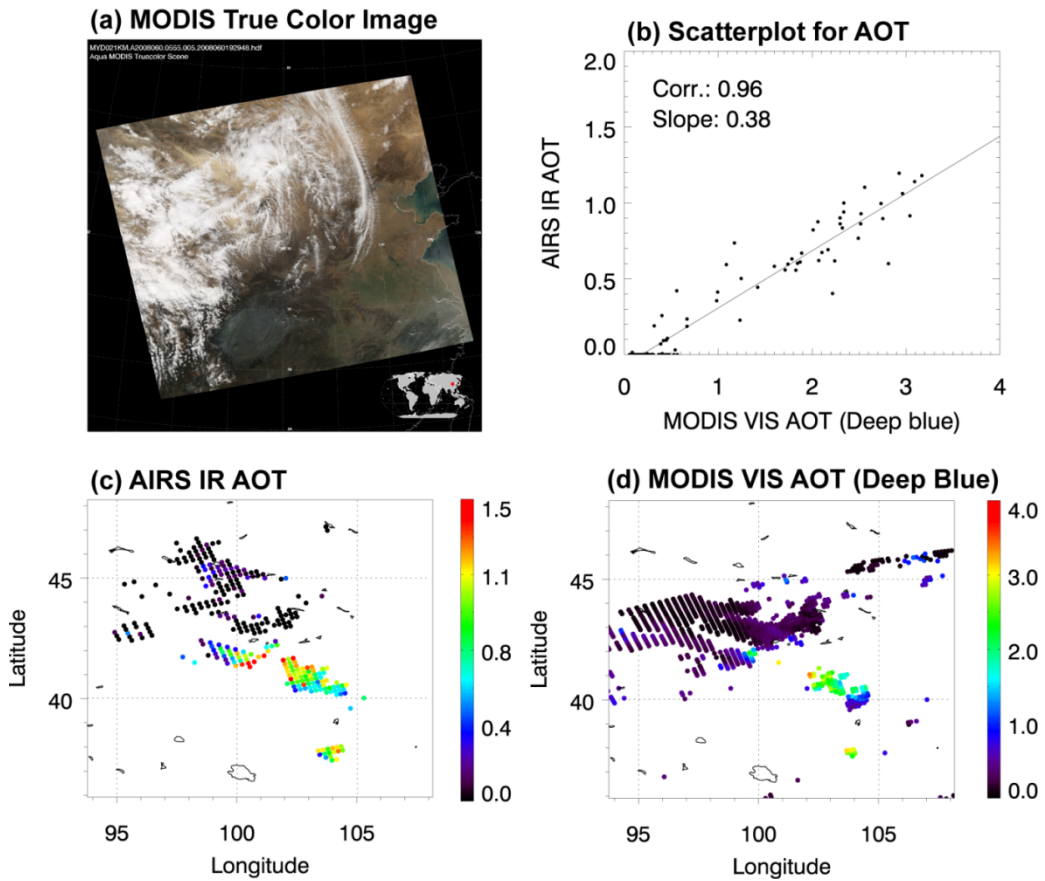


Figure 31. (a) MODIS true color image, (b) Scatterplot for AIRS IR AOT and MODIS VIS AOT, (c) IR AOT retrieved from AIRS measurements, and (d) MODIS-derived AOT on February 29, 2008.

### **6.4.2 March 1, 2008 case**

The dust plume originating in the Gobi Desert moved eastward and arrived in the western Bohai Bay and around Tianjin, China, on March 1, 2008. Figure 32 provides the MODIS true color image, AIRS IR AOT, and MODIS AOT. The MODIS AOT in Figure 32c is the combination of “Deep Blue Aerosol Optical Depth 550 Land” over land and “Optical Depth Land and Ocean” over ocean. Figure 32b indicates that ANN IR AOT fairly well captures the dust storm near the Bohai Bay, and gives a general good agreement with MODIS VIS AOT. Scatterplots for the collocated AIRS and MODIS AOTs in Figure 33 show the comparisons of AIRS IR AOTs with collocated “Deep Blue Aerosol Optical Depth 550 Land” and “Optical Depth Land and Ocean” over land and ocean, respectively. Between AIRS IR AOTs and MODIS deep blue AOTs, a good linear relationship is shown with a correlation coefficient of 0.91 and a slope of 0.34. However, the comparison between AIRS IR AOTs and MODIS AOTs over ocean gives a correlation coefficient of 0.77, which is lower than for land. In comparison with the slope of 0.34 over land, the slope over ocean is much lower value about 0.13, indicating a significant discontinuity of MODIS AOTs between land and ocean, whereas the AIRS AOTs have a smooth transition from land to ocean. The discontinuity of MODIS AOT between land and ocean appears to be visually evident in Figure 32c, noting that high AOT area larger than about 4.0 is largely separated along the coastal line near the Bohai Bay. Because of no persuading scientific reason explaining such contrast along the coast, we suspect that the discontinuity is caused by different MODIS

algorithms applied over land and ocean.

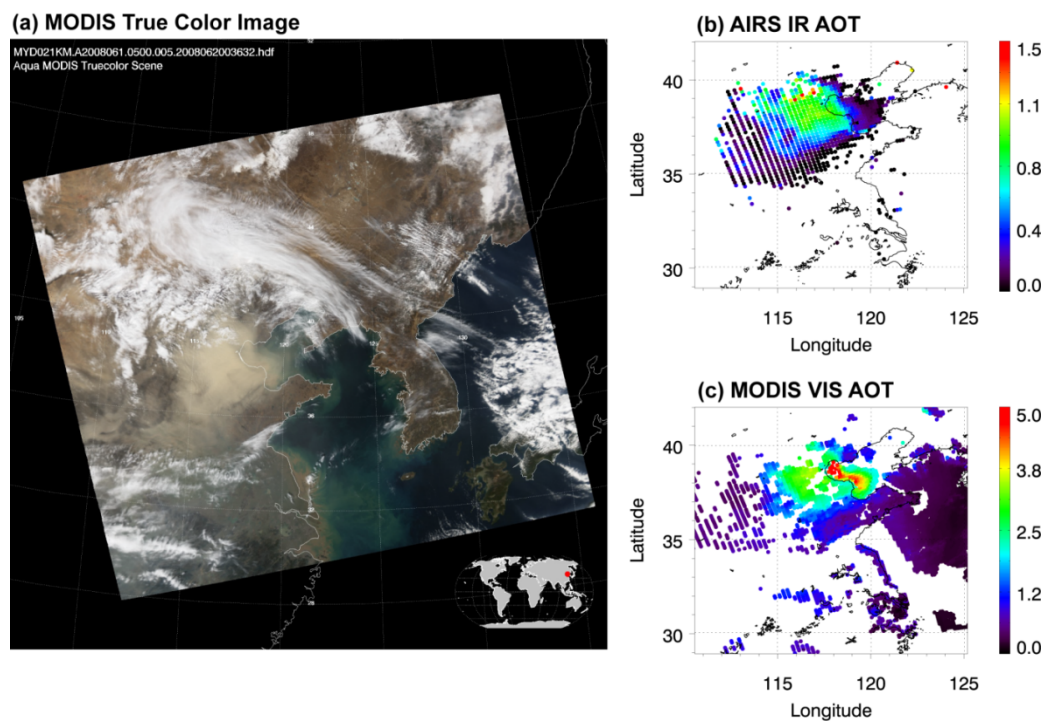


Figure 32. (a) MODIS true color image, (b) IR AOT retrieved from AIRS measurements, and (c) MODIS-derived AOT on March 1, 2008.

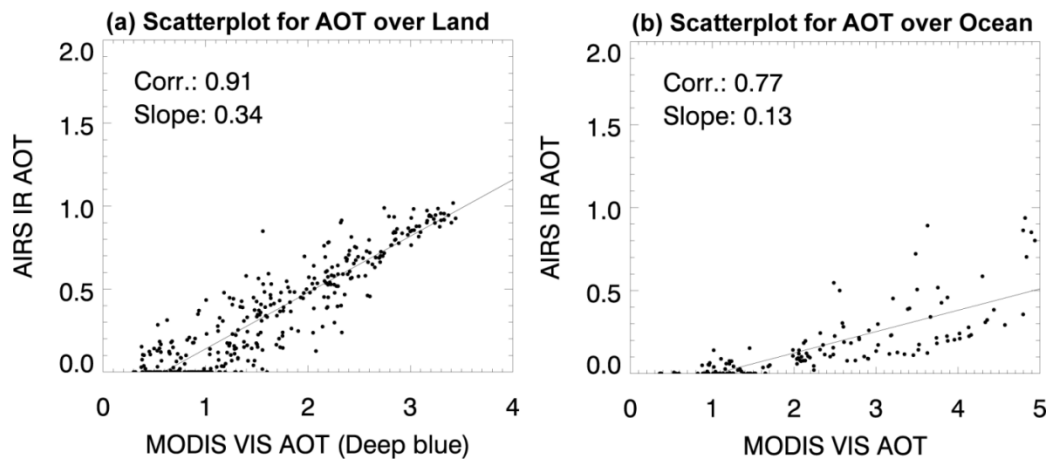


Figure 33. Scatterplots for AIRS IR AOT and MODIS VIS AOT over (a) land and (b) ocean on March 1, 2008.

### **6.4.3 May 11, 2011 case**

A giant swirl of dust storm was observed on May 11, 2011 where the borders of Mongolia and China meet. Figure 34 provides MODIS true color image (Figure 34a), AIRS and MODIS AOTs (Figure 34c and 34d), and their comparison (Figure 34b) for the dust storm. In Figure 34a, the true color image, the bright dust plume blowing in a counter-clockwise direction is clearly visible over the northern China, and its general pattern is captured fairly well by both of AIRS and MODIS AOTs as shown in Figure 34c and 34d, respectively. The scatterplot comparing AIRS and MODIS AOTs with a high correlation coefficient of 0.81 between the two retrievals indicates that the AIRS AOTs are comparable to those from MODIS.

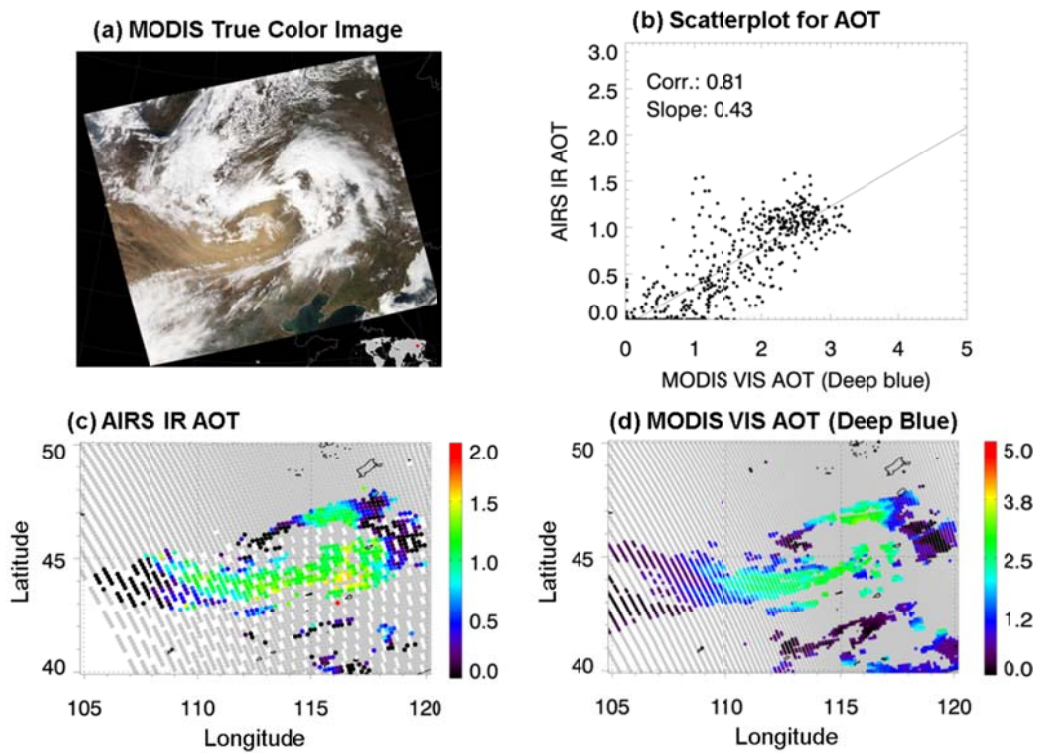


Figure 34. (a) MODIS true color image, (b) Scatterplot for AIRS IR AOT and MODIS VIS AOT, (c) IR AOT retrieved from AIRS measurements, and (d) MODIS-derived AOT on May 11, 2011.

#### **6.4.4 April 23, 2009 case**

The dust event on April 23, 2009, analyzed in section 4.5 using the ANN model, was applied to the physical algorithm again (Figure 35 and 36). In Figure 35b, the comparison between AIRS-retrieved IR AOTs and MODIS deep blue AOTs is shown, with associated statistics (correlation coefficient and slope). The scatterplot shows a linear relationship with a statistically meaningful correlation coefficient of 0.76 and a slope of 0.31. The general patterns shown in AIRS retrievals in Figure 35c are similar to those of MODIS AOTs based on the deep blue algorithm in Figure 35d. However, it was noted that some erroneous AOTs were noted along the Qinghai high-terrain area, in particular, at the southeast edge of the AIRS retrievals.

Considering that the ANN model was able to stably retrieve AOTs, it may be plausible to say that measured AIRS spectrum carries dust signals that could be converted to dust AOTs. Thus less accurate retrievals over the high terrain area are likely due to less accurate information on other parameters such as surface or atmospheric states that also influencing the AIRS spectrum. The high AOTs from the ANN approach near the vortex-shaped cloud area seem to be caused by incomplete cloud screening.

The two-dimensional distribution of the AIRS-derived effective dust height is given in Figure 36a while Figure 36b shows retrieved dust height along a CALIPSO track depicted by red line in Figure 36a. The AIRS dust height generally follows the CALIPSO-measured height inferred from the backscatters. However, the retrievals slightly deviate around 4 km, even over the

area north of 44°N where a rough and irregular dust layer exist.

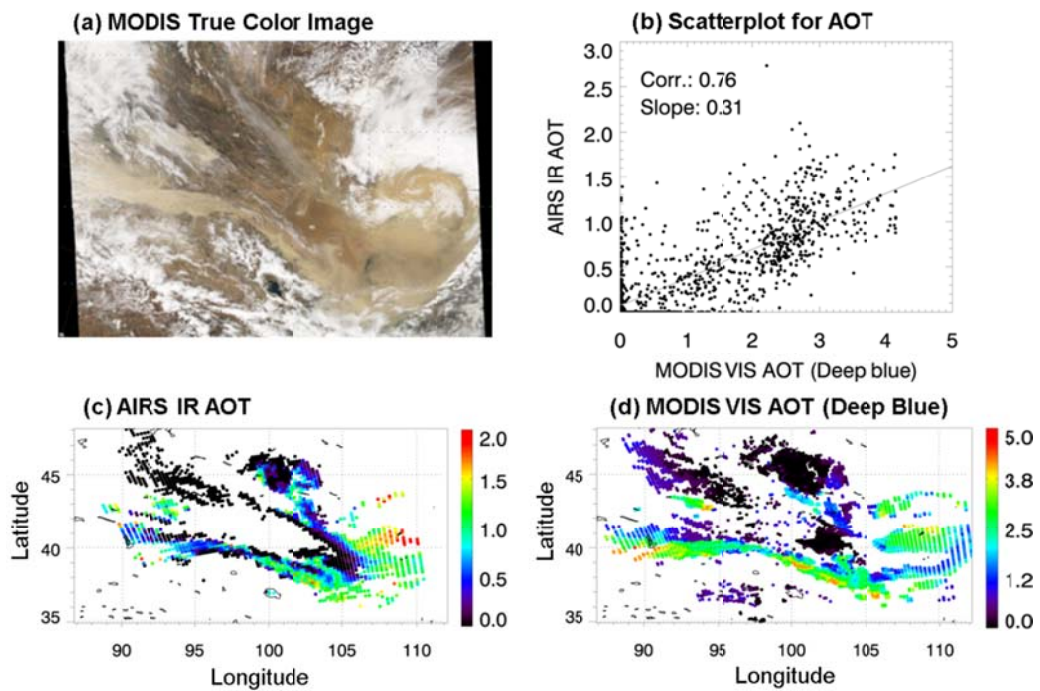


Figure 35. (a) MODIS true color image, (b) scatterplot for AIRS IR AOT and MODIS VIS AOT, (c) IR AOT retrieved from AIRS measurements, and (d) MODIS-derived AOT on April 23, 2009.

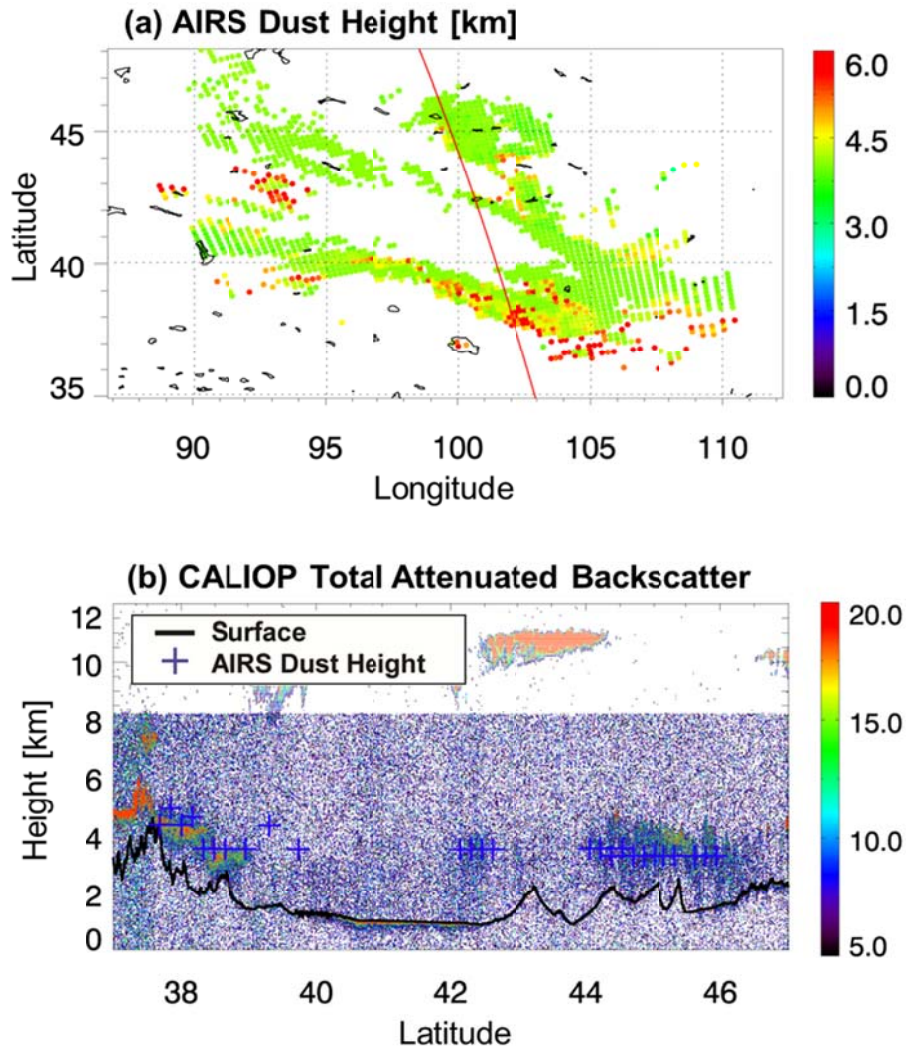


Figure 36. (a) Two-dimensional distributions of dust heights retrieved from AIRS measurements, and (b) vertical view of CALIOP-measured total attenuated backscatter at 532 nm on April 23, 2009 over the Gobi Desert area, along the CALIPSO track [red line in (a)]. The backscatter in units of  $\text{km}^{-1} \text{sr}^{-1}$  is multiplied by 1000, and values smaller than  $5.0 \times 10^{-3} \text{ km}^{-1} \text{sr}^{-1}$  are masked out in (b).

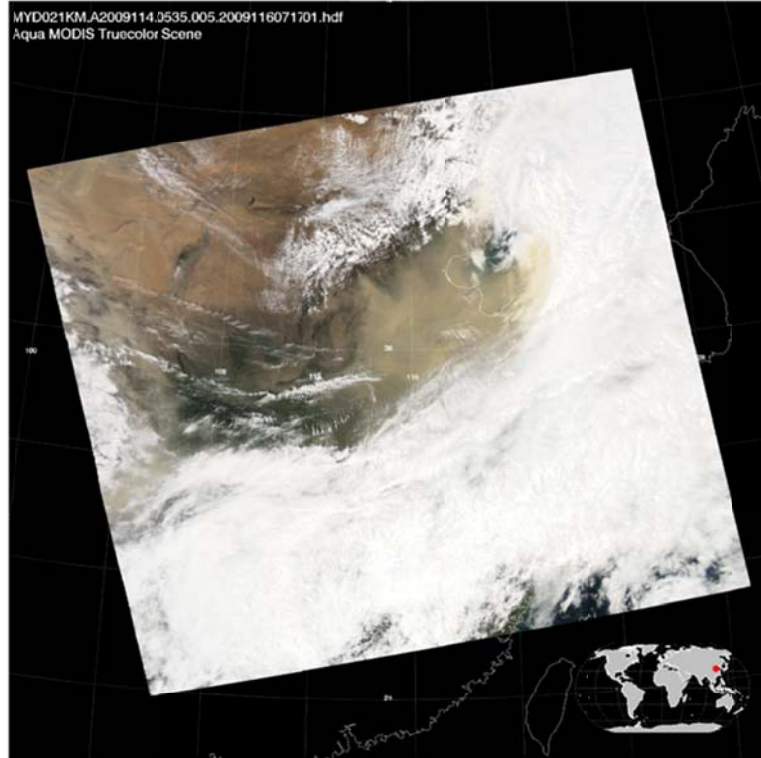
### **6.4.5 April 24, 2009 case**

Figure 37 focuses on AOT retrieval for the case of the dust plume that advected eastward on April 24, 2009. In the MODIS true color image in Figure 37a, a strong dust storm following deep convective clouds is represented over the area extending from Beijing eastward to the Tianjin and Bohai Bay. The general patterns of AIRS retrievals over land are quite similar to those of the MODIS. Over ocean, AIRS AOT is quite smaller than AOT for land, resulting in a weak discontinuity in AIRS AOT across the coastline. In contrast to the AIRS retrieval, MODIS-derived AOT over ocean is conspicuously larger than those over land. The noticeable discontinuity in MODIS AOTs between land and ocean is more obvious than AIRS, and it is likely caused by the different MODIS retrieval algorithms. Moreover, problems stemming from imperfect cloud screening appear to remain, resulting in high AOTs in the area between Laizhou Bay and Liaodong Peninsula which are covered by both cloud and dust features. Scatterplots for AIRS IR AOTs versus MODIS AOTs over land and ocean are given in Figure 38a and 38b, respectively. The AOTs show good relationships for both land and ocean retrievals, with correlation coefficients of 0.89 and 0.86. It is noted that large slope difference exists again between land and ocean, i.e. 0.44 vs. 0.24.

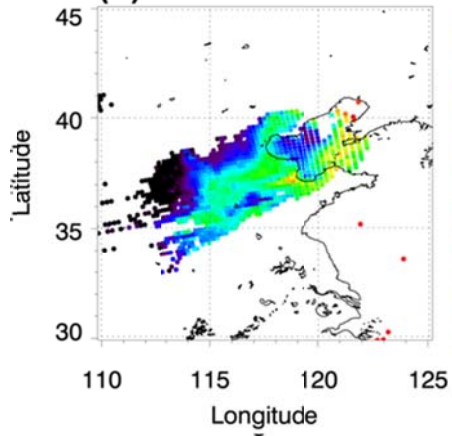
According to the CALIOP backscatter in Figure 39, a dust layer is located around 1.5–4 km in altitude along a 35°–39° CALIPSO track. South of the dust area, there is a thick and high cloud cover, and the Taihang mountains are located north of about 39.5°N. In Figure 39b, dust heights are retrieved in

reasonable range of 2–4 km, but retrieval error reaches up to about 0.9 km, and overestimations are evident over the area north of 38°N. By taking a closer look at the CALIOP level 1B attenuated backscatter in Figure 39b and the level 2 CALIPSO AOT (not shown here), shallow and weak dusts can be seen floating over a thick dust layer north of 38° latitude. Given the single dust layer assumption in the retrieval algorithm, the overestimate might be caused by the multiple dust layers.

**(a) MODIS True Color Image**



**(b) AIRS IR AOT**



**(c) MODIS VIS AOT**

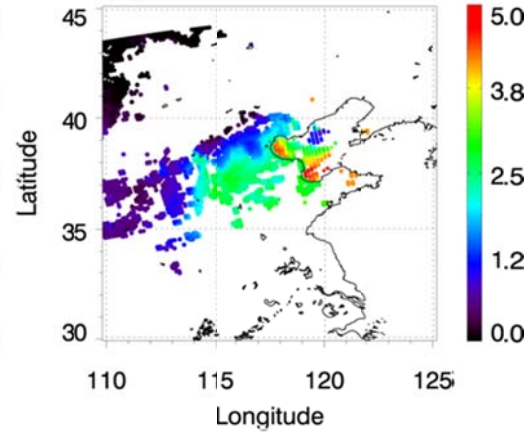


Figure 37. (a) MODIS true color image, (b) IR AOT retrieved from AIRS measurements, and (c) MODIS-derived AOT on April 24, 2009.

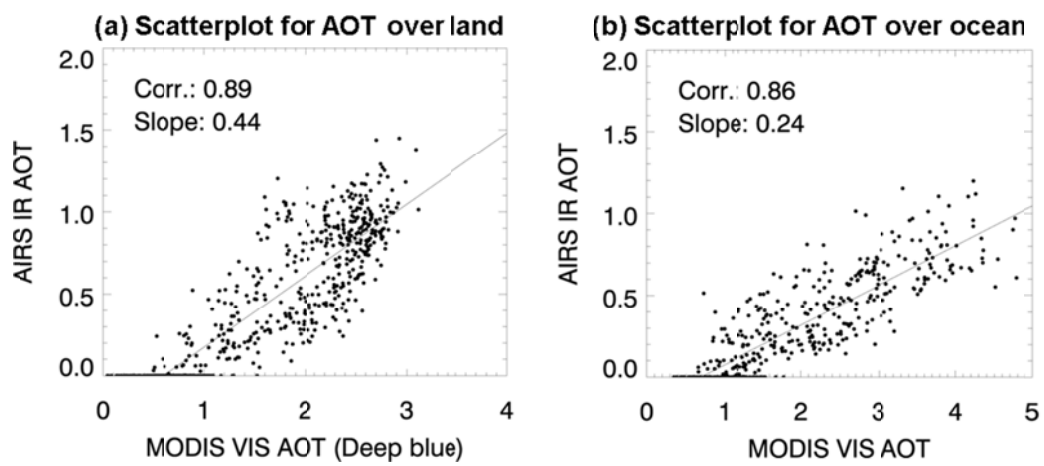


Figure 38. Scatterplots for AIRS IR AOT and MODIS VIS AOT over (a) land and (b) ocean on April 24, 2009.

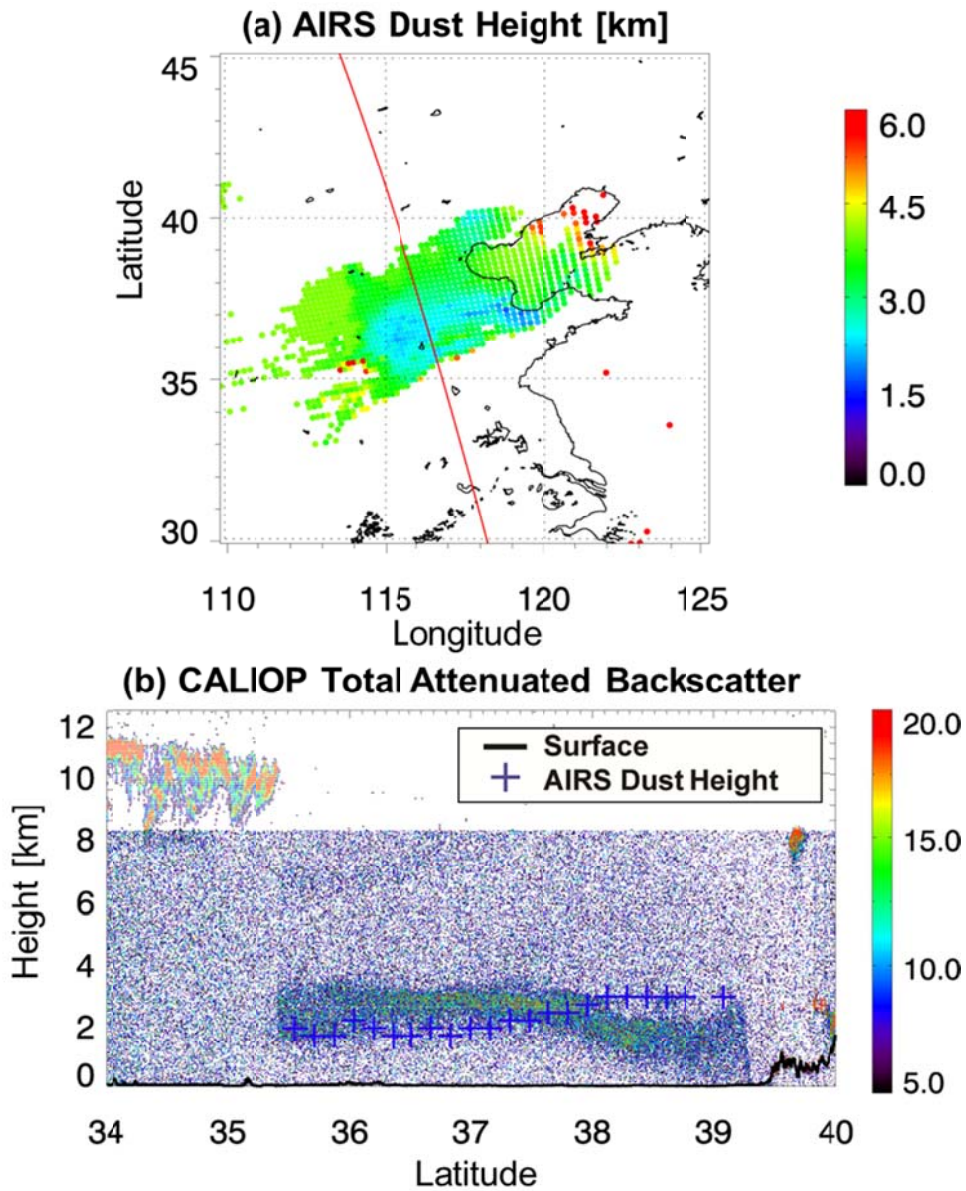


Figure 39(a) Two-dimensional distributions of effective dust heights retrieved from AIRS measurements and (b) vertical view of CALIOP-measured total attenuated backscatter at 532 nm along the CALIPSO track [red line in (a)] on April 24, 2009.

#### **6.4.6 Evolutionary feature of April 23–24, 2009 dust event**

Since MODIS aerosol product is based on visible measurements, it is only available during the daytime. However, it is now possible to retrieve AOT even during the nighttime because AIRS IR measurements are available in both day and night. Taking this opportunity to use IR-based dust optical properties for monitoring evolution of dust storms, day and nighttime dust AOTs and heights are retrieved on April 23, 2009 as a case of example. Obtained evolutionary features of the dust event from April 23 to 24 are shown in Figure 40 and 41. AIRS-derived AOTs are shown in the middle panels. Also shown are MODIS true color images (Figures 40a-b) and MODIS-derived AOTs but only daytime (Figures 40f-g). The combination of day and nighttime dust AOTs clearly depicts an evolutionary feature of dust storm: the dust band shown in the daytime of April 23 over the Gobi desert moved eastward during the nighttime, and then reached to the Bohai Bay on April 24. The vortex-shaped dust plume in Figure 40d implies that the dusts followed a cyclone surrounded by clouds, and the presence of cloud is shown visibly in MODIS cloud product (not shown here). Comparing with the daytime AIRS-retrieved AOTs on April 23 and 24, the magnitude of nighttime AOTs are in a reasonable range of 0.2–1.5, except for some pixels adjacent to the clouds.

Nighttime effective dust heights are also obtained from AIRS-measured TBs and displayed in Figure 41 with associated MODIS true color images, and CALIOP total attenuated backscatters at 532 nm for comparison. During the nighttime of Apr. 23, CALIPSO detects a dust layer in the south of the thick

clouds, and its vertical heights are in a range of 3–4 km as shown in the two-dimensional distribution of  $z_{\text{dust}}$  (Figure 41d). A comparison is made using the vertical view of CALIOP backscatters in Figure 41g along the track of CALIPSO, and it indicates that the CALIOP-measured dust heights are captured well by AIRS-retrieved  $z_{\text{dust}}$ . The continuous retrievals of two-dimensional dust height both for day and nighttime can be used as valuable information for dust monitoring and data assimilation.

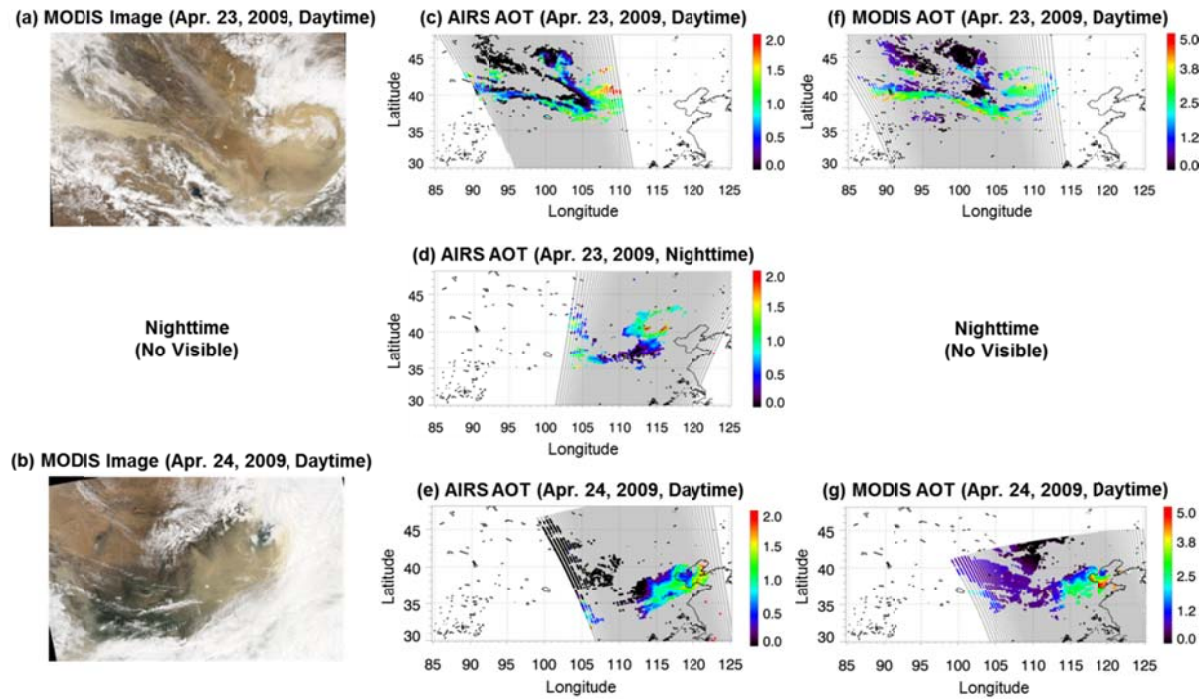


Figure 40. (a)–(b) MODIS true color images, (c)–(e) AOTs retrieved from AIRS measurements, and (f)–(g) MODIS-derived AOTs during April 23–24, 2008.

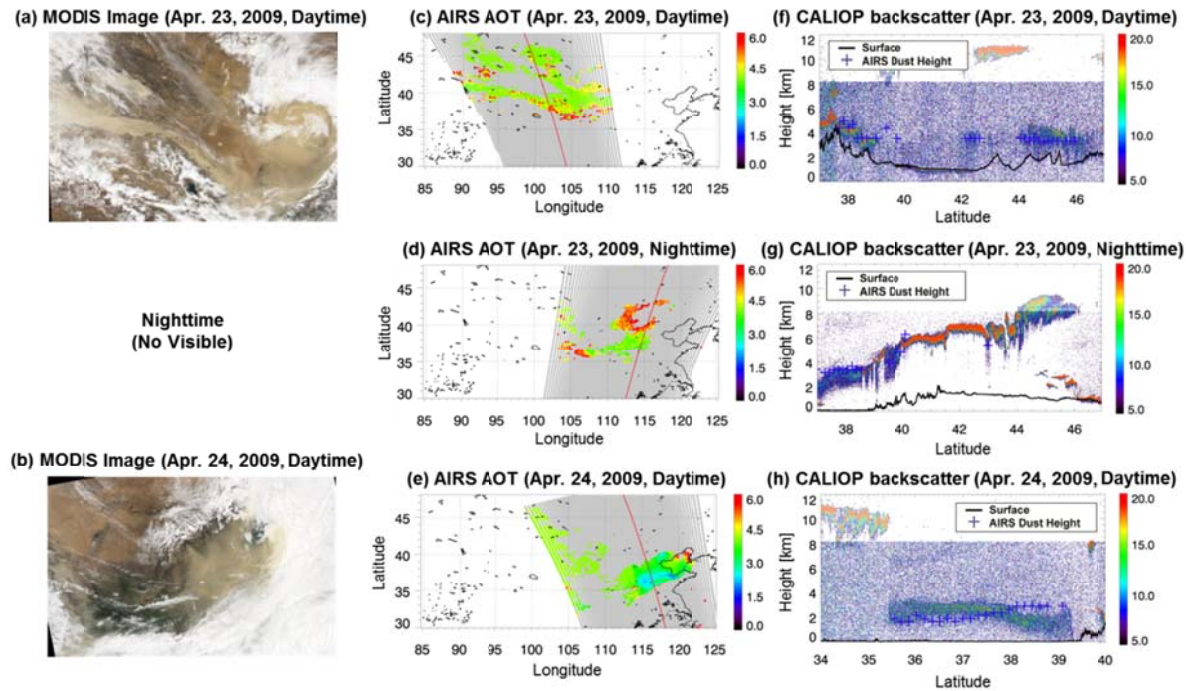


Figure 41. (a)–(b) MODIS true color images, (c)–(e)  $z_{\text{dust}}$  retrieved from AIRS measurements, and (f)–(h) vertical view of CALIOP-measured total attenuated backscatter at 532 nm during April 23–24, 2008, along the CALIPSO track [red line in (c)–(e)]. The backscatter in unit of  $\text{km}^{-1} \text{sr}^{-1}$  are multiplied by 1000, and values smaller than  $5.0 \times 10^{-3} \text{ km}^{-1} \text{sr}^{-1}$  are masked out in (f)–(h).

#### **6.4.7 April 23 and 24, 2009 cases with initial guess fields from ANN retrievals**

An advantage of physical retrievals is the ability to incorporate initial-guess information into the retrieval process. This is potentially helpful information which could improve performance of the physical retrieval algorithm if the initial-guess is accurate (Reuter et al., 1988). In this section, the physically based retrieval algorithm is applied to the dust event on April 23 and 24, 2009 again, but with different initial guess field. The daytime AOT and  $z_{\text{dust}}$  retrieved from the ANN models are employed as an initial-guess field for the dust retrieval, expecting more accurate retrievals. The uncertainty of initial AOT and dust height are established as  $2000 \text{ cm}^{-3}$  and 0.05 hPa, respectively. The retrieved AOT and  $z_{\text{dust}}$  are shown in Figures 42–46.

Figure 42 presents the AIRS-retrieved AOT on April 23, 2009 and the MODIS deep blue AOT for a comparison. The scatterplot for AIRS and MODIS AOTs in Figure 42b shows a linear relationship with a correlation coefficient of 0.72 which is slightly lower than the coefficient from constant initial-guess (Figure 35b). The two-dimensional distribution of the AIRS-derived AOT given in Figure 42c has a similar pattern with the distribution of MODIS AOT in Figure 42d, but some overestimation appears near cloudy pixels. The overestimation might be caused by relatively high AOTs by ANN retrievals in Figure 20b, and it produces slightly lower correlation coefficient. However, there is no significant difference between the retrieved AOTs using constant

AOT and ANN-derived AOTs as an initial-guess field. Two-dimensional retrieved  $z_{\text{dust}}$  and its comparison with CALIOP total attenuated backscatter for the same dust case are given in Figure 43a and 43b, respectively. Although overestimation is clear over the high-terrain area around  $38^{\circ}\text{N}$ , which might be induced by the ANN-retrieved  $z_{\text{dust}}$ , the retrievals appear in general more reasonable than nearly invariable  $z_{\text{dust}}$  based on constant initial-guess in Figure 36.

Figure 44 illustrates the MODIS true color image, AIRS-retrieved AOT, and MODIS AOT distribution for the dust plume observed on April 24, 2009. Over land, the AIRS AOTs (Figure 44b) are much similar to those from the constant first guess (Figure 37b) except for the southern boundary between dust and cloud. However, over ocean, there appears a significant distinction between AOTs between the use of ANN-retrieved values and constant value as initial-guesses. The use of ANN retrievals as the initial-guess brought in more homogeneous AIRS AOTs between land ocean, weakening the sharp contrast shown in Figure 37b. Excessively high AOT in the area between Laizhou Bay and Liaodong Peninsula, however, are likely associated with cloud contamination that is visible as yellowish area over the cloud edge north of Shandong peninsula. Overall, improvement is evident.

Scatterplots for AIRS and MODIS AOTs over land and ocean are given in Figure 45a and 45b, along with associated statistics. While the statistics of the comparison using ANN-retrieved initial-guess have a resemblance to those

of the constant initial-guess over land, a noteworthy distinction between the different initial-guesses is found over ocean. Correlation coefficient of 0.80 in Figure 45a is lower than that of constant initial-guess of 0.86, and slope goes up from 0.24 to 0.36 combined with an increase in AIRS-derived ocean AOTs. However, this increased slope appears in part due to high values that might be caused by cloud contamination. Although the correlation coefficients becomes slightly smaller, it seems sensible to conclude that the use of ANN-retrieved dust properties as an initial-guess field gives more reasonable results when reduced disparity between land and ocean AOTs are considered as shown in Figure 44c.

AIRS-retrieved  $z_{\text{dust}}$  for the dust plum on April 23, 2009 is given in Figure 46. As in the Figure 39, vertical view of CALIOP backscatters are plotted together with the AIRS-retrieved  $z_{\text{dust}}$  along the CALIPSO track. Comparing two-dimensional distributions of AIRS  $z_{\text{dust}}$  in Figure 39a and 46a, by and large, the  $z_{\text{dust}}$  from the ANN-retrieved initial-guess are lower than those from the constant initial-guess. Based on the comparison against CALIOP backscatters in Figure 46b, AIRS-retrieved  $z_{\text{dust}}$  agrees better with CALIOP dust height when ANN retrievals are used as an initial-guess for the physical retrieval.

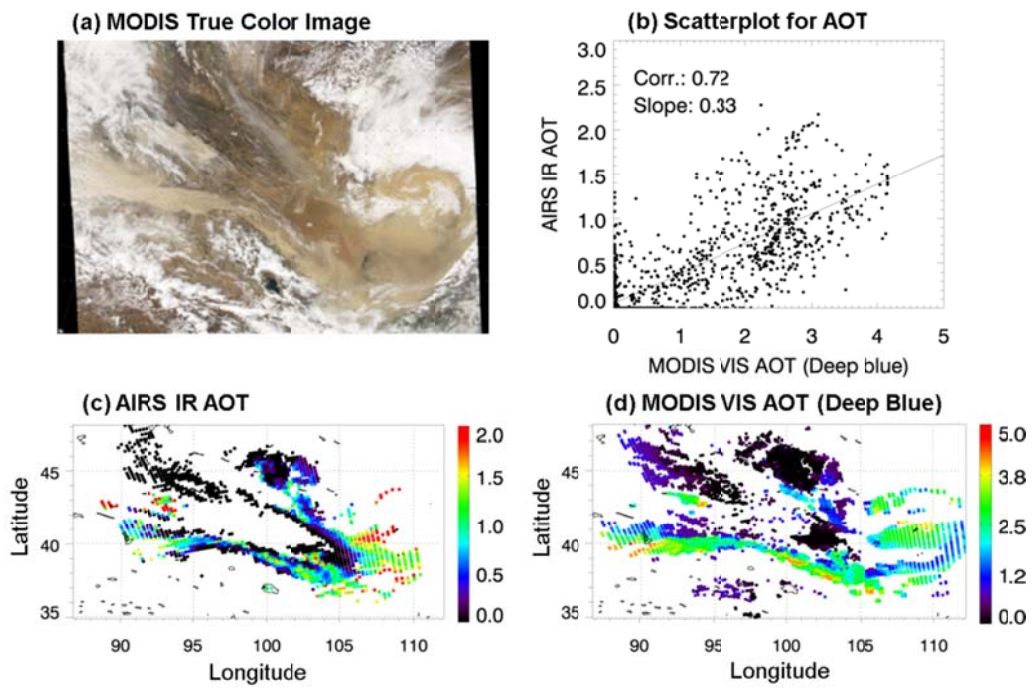


Figure 42. Same as Figure 35, except for use of the ANN-retrieved initial-guess field.

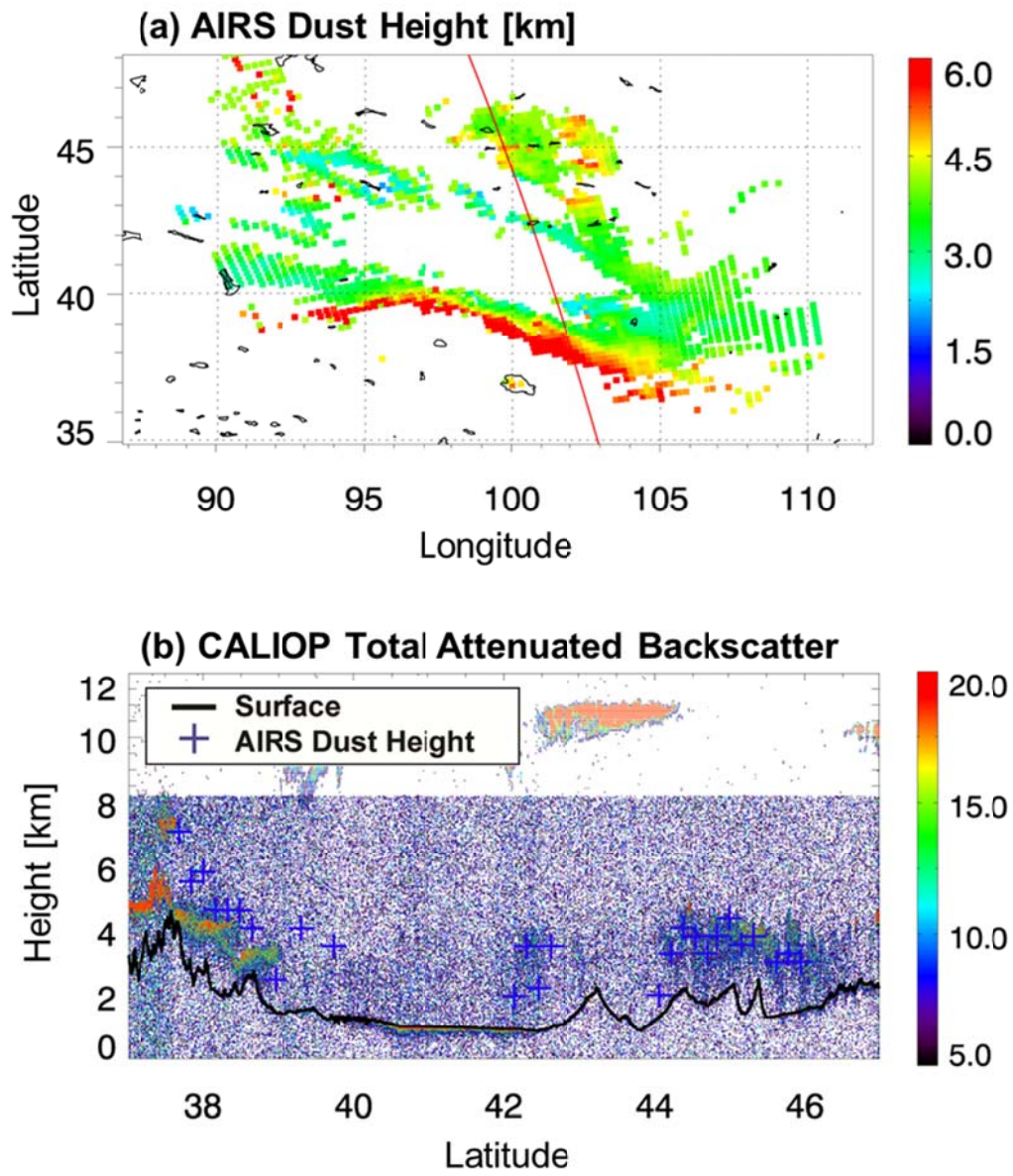
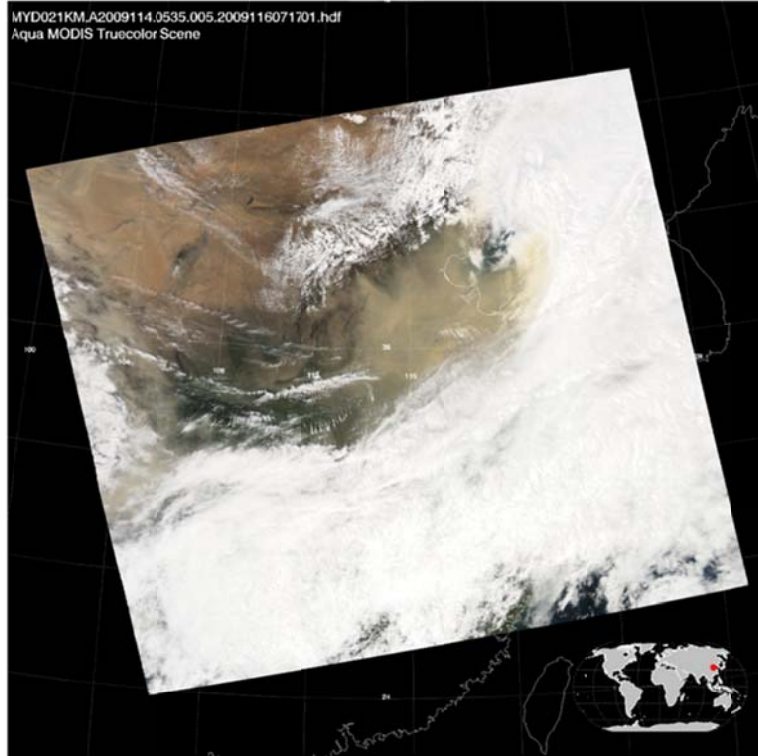
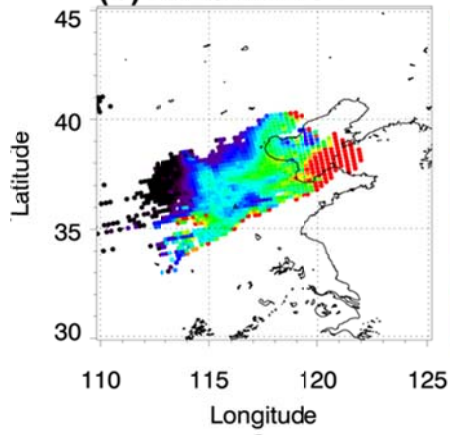


Figure 43. Same as Figure 36, except for use of the ANN-retrieved initial-guess field.

**(a) MODIS True Color Image**



**(b) AIRS IR AOT**



**(c) MODIS VIS AOT**

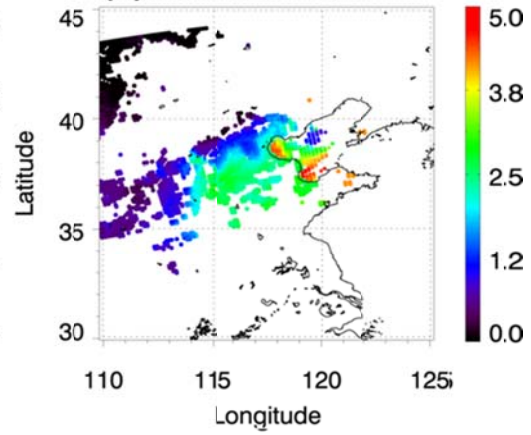


Figure 44. Same as Figure 37, except for use of the ANN-retrieved initial-guess field.

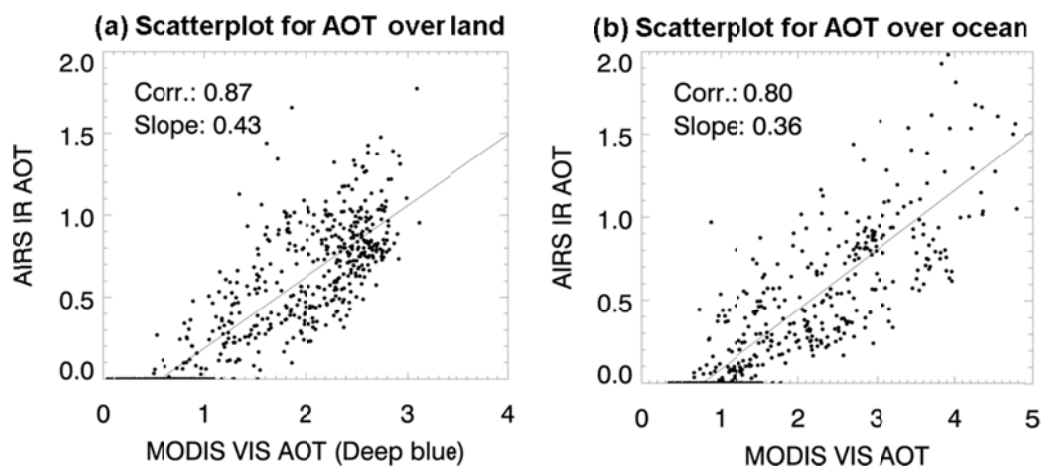


Figure 45. Same as Figure 38, except for use of the ANN-retrieved initial-guess field.

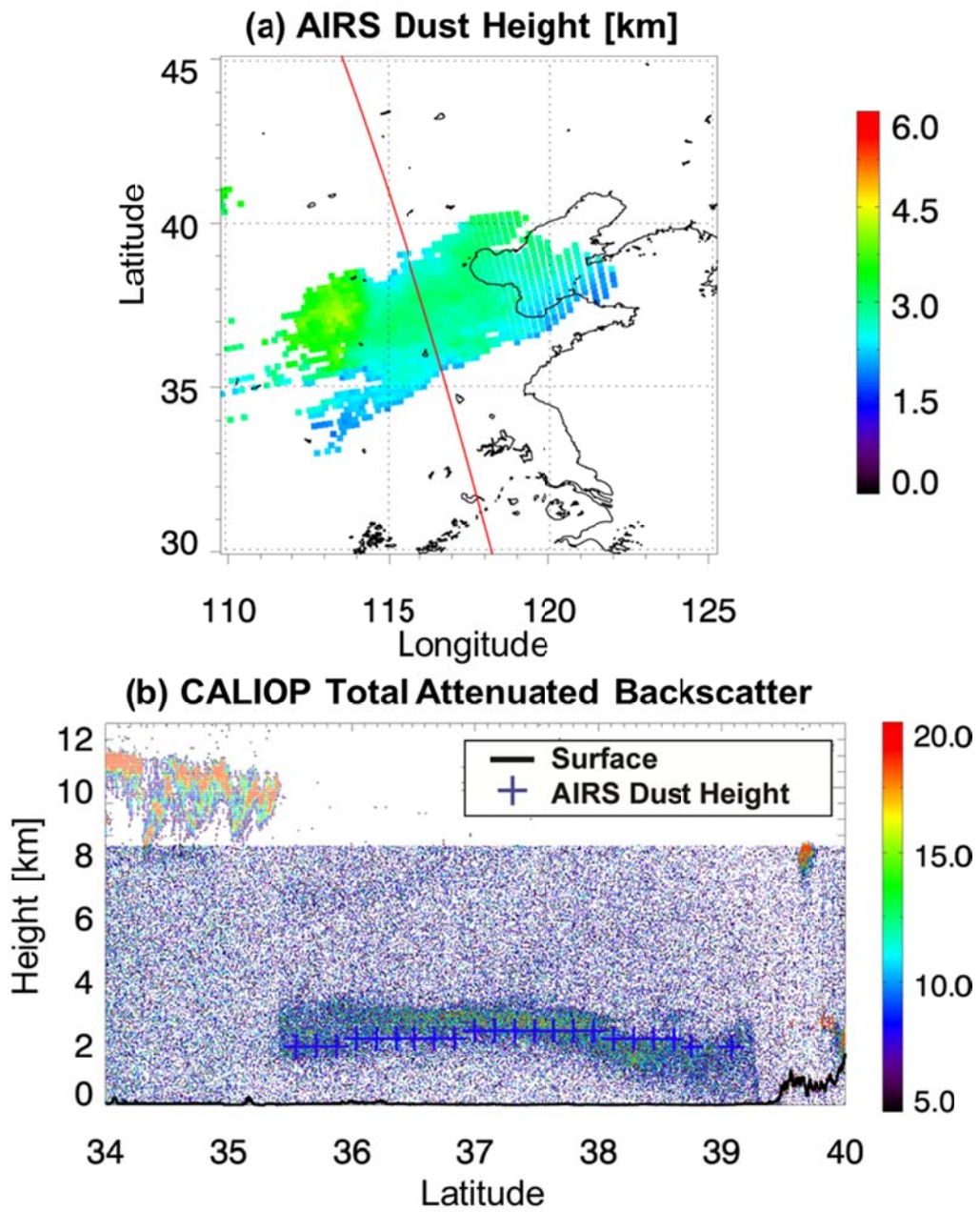


Figure 46. Same as Figure 39, except for use of the ANN-retrieved initial-guess field.

#### **6.4.8 Statistical summary**

It is noted that two-dimensional dust retrievals for Asian dust from AIRS measurements were generally in good agreement with MODIS AOTs and CALIPSO dust heights. Associated statistics are summarized in Table 5: the correlation coefficients in the range of 0.76–0.96 indicate the AIRS-retrieved IR AOT shows a strong relationship with the MODIS-derived VIS AOT. Slopes of linear regressions are in the range of 0.31–0.44 over land, and 0.13–0.36 over ocean, and they generally lie within the confines of previous studies.

As shown in Equation (2), the slope is the ratio between the VIS and IR extinction coefficients, because AOT is the product of the extinction coefficient and the total number of particles. Since a spectral extinction coefficient depends on the chemical composition of a dust particle, the variation of the slope may indicate diverse dust compositions across dust-source regions. The dust case on April 24, 2009 presented a relatively higher slope of 0.43 and 0.44 over land, whereas the case on April 23, 2009 had slopes of 0.31 and 0.33, similar to the values in other cases. These different slopes may be considered changes in dust composition during its downstream transportation. The large difference between slopes for land and ocean are partly due to the well-known physical discontinuity of MODIS algorithms for land and ocean, and to the limitation of retrieval algorithm over ocean. Use of more accurate initial-guess field, as discussed above, could reduce the discrepancy between AIRS AOTs over land and ocean.

Table 5. Correlation coefficient (R), linear regression slopes and offsets for AIRS IR AOT and collocated MODIS AOT.

Date	Land			Ocean		
	R	Slope	Offset	R	Slope	Offset
Feb. 29, 2008	0.96	0.38	-0.07	-	-	-
Mar. 1, 2008	0.91	0.34	-0.20	0.77	0.13	-0.13
May 11, 2011	0.81	0.43	-0.06	-	-	-
Apr. 23, 2009	0.76	0.31	0.06	-	-	-
Apr. 24, 2009	0.89	0.44	-0.26	0.86	0.24	-0.17
Apr. 23, 2009 ( <i>ANN</i> <sup>a</sup> )	0.72	0.33	0.05	-	-	-
Apr. 24, 2009 ( <i>ANN</i> )	0.87	0.43	-0.25	0.80	0.36	-0.28

a: *ANN* means that dust properties are retrieved with an initial-guess field using the ANN model retrievals.

## 7. Summary and conclusions

Taking advantage of the high spectral resolution of the hyperspectral IR instruments, the AOT and height of Asian dust were retrieved by applying ANN and physical variational methods to AIRS measurements. To examine the possible use of the hyperspectral IR measurements for dust retrieval, an ANN algorithm retrieving the AOT and  $z_{\text{dust}}$  of Asian dust from AIRS hyperspectral IR measurements has been developed. In doing that, two training data sets were prepared: 1) a set for dust AOT, based on collocated AIRS TBs (130, 31, 44, and 29 channels for the WIN, CO<sub>2</sub>, WV, and O<sub>3</sub> bands, respectively) with MODIS AOTs at 550 nm and 2) a set for  $z_{\text{dust}}$ , based on collocated AIRS TBs used for the AOT training with CALIPSO  $z_{\text{dust}}$ . Values of  $z_{\text{sfc}}$  and  $1/\mu$  associated with satellite viewing geometry were also added to the collocated data sets. From the various sensitivity tests relating AIRS TBs to either AOT or  $z_{\text{dust}}$  in the ANN model, it was found that WIN channel TBs in the AIRS measurements are far more important in predicting either AOT or  $z_{\text{dust}}$ . However, substantial contributions can be made by TBs in CO<sub>2</sub> channels to  $z_{\text{dust}}$  retrievals. Based on sensitivity test results, ANN models for AOT and  $z_{\text{dust}}$  retrievals were established with TBs using a total of 234 channels,  $z_{\text{sfc}}$ , and  $1/\mu$  as inputs.

To assess the performance of the ANN model we developed for AOT retrieval, AOTs retrieved from AIRS measurements were compared with MODIS-derived AOTs over a period different from that used for training. The pixel-level AOT comparison showed a correlation coefficient of 0.84, mean bias of 0.03, and RMSE of 0.37, suggesting that the ANN-derived AOTs are

comparable to MODIS AOTs. The comparison of pixel-level  $z_{\text{dust}}$  retrieved from AIRS measurements also showed good agreement with the collocated CALIPSO  $z_{\text{dust}}$ , with a correlation coefficient of 0.79, mean bias of about -0.02 km, and RMSE of 0.54 km. Two-dimensional dust retrievals for two dust events over Chinese desert regions showed good agreement with collocated MODIS AOT and CALIPSO  $z_{\text{dust}}$ , demonstrating that the algorithm developed in this study can be used for dust monitoring.

By extending the results obtained from the ANN approach to the development of a physically-based variational method for dust retrieval, IR radiative transfer modeling was improved. For that, optical and physical properties for Asian dust from sky radiometer measurements, various refractive indices, and spatially and temporally varying surface spectral emissivities were included in a radiative transfer model. The size distributions for Asian dust were estimated from multi-year sky radiometer measurements at the Dunhuang site in the east of Chinese Taklimakan Desert. Spectral surface emissivities were specified with the UW/CIMSS emissivity atlas in order to better describe the surface contribution to the TOA radiance. For a given size distribution and specified surface emissivity over the East Asian region, the impact of three different IR refractive indices for the dust (OPAC mineral aerosol, dust-like aerosol observed by Volz, and quartz from HITRAN) on the simulated AIRS radiances have been studied for the dust conditions prescribed by CALIPSO retrievals. The simulations were compared to AIRS TBs in the IR window regions.

The results indicate that the specification of surface emissivity using geographically and monthly-varying UW/CIMSS data significantly improved the accuracy of simulated IR TBs. Hence, an accurate description of land-surface emissivity is considered a prerequisite for the remote sensing of dust from IR spectral measurements. We also found that Asian dust can be more accurately simulated by using the Volz refractive index, in addition to realistic Asian dust-size distributions and UW/CIMSS surface emissivity data. We suggested that radiative transfer modeling could be improved with best estimates of the optical properties of the dust and surface emissivity, which are now considered necessary for optimal retrieval of dust properties using hyperspectral IR measurements from space.

Based on the improved dust modeling, AOTs at an 10.4  $\mu\text{m}$  wavelength and at dust-effective heights were estimated from AIRS TB measurements using a 1DVAR algorithm. AIRS TBs measured at eleven channels at window and  $\text{CO}_2$  absorption bands were selected as inputs because the synergetic use of the WIN and  $\text{CO}_2$  channels were identified as most significant channels describing TOA radiative signature associated with dust height. For the dust retrievals, the atmospheric and surface states were assumed to be known, and those states were obtained from the regional forecasting model outputs.

As cases two dust outbreaks in the Gobi Desert and two dust plumes in downstream areas were chosen, and the 1DVAR algorithm was applied. The comparison of obtained results with MODIS-derived AOTs at the VIS band (550 nm) and with the CALIOP attenuated backscatters demonstrated that

AIRS-retrieved AOTs agree well with those of the deep-blue based MODIS results, with correlation coefficients in the range of 0.81–0.96 for three dust cases over land (February 29, 2008; March 1, 2008; April 24, 2009; May 11, 2011). However, the dust outbreak on April 23, 2009 showed a relatively low correlation coefficient of 0.76, indicating less-accurate AOT retrievals over the high-terrain area. The discrepancies may be in part induced by less accurate surface or atmospheric state over high terrains, which remained constant in the retrieval process. Correlation coefficients of 0.77 and 0.86 for the linear regressions of AOTs over ocean also presented good agreement between AIRS IR AOTs and MODIS VIS AOTs.

Ratios of AIRS AOTs to MODIS-derived AOTs were in the range of 0.34–0.44 over land, and of 0.13–0.24 over ocean. The ratios shown in this study are similar to or slightly larger than the values in previous studies (0.05–0.43). The reason for this is not clear, but it might be in part due to different optical properties amongst the dusts in the Gobi, Sahara, and Taklimakan Deserts. Nonetheless, the significant difference in slopes between land and ocean manifests the discontinuity created by the MODIS deep blue algorithm and ocean algorithm.

To validate the AIRS retrievals of the dust height, results for April 23, 2009 and April 24, 2009 were compared with collocated CALIOP-measured attenuated backscatters. It was shown that the AIRS-retrieved dust effect heights were in reasonable range, comparing the CALIOP backscatters. However, dust heights were overestimated over the highly complex terrain area,

as shown in the ANN model results over the same area. In addition, the algorithm tends to yield incorrect dust heights when multiple layers exist, because of single layer assumption made for the retrieval processes.

In order to further examine the effect of an initial-guess on the retrieval performance, AOTs and effective dust height obtained from the ANN-models were used as an initial-guess field into the physically based retrieval algorithm. The April 23 and 24, 2009 dust cases were selected and the retrieved dust properties were compared with those from the use of the constant initial-guess field. In comparison, correlations between AIRS and MODIS AOTs slightly got lower. The lower correlation coefficients are mainly due to the reflection of relatively high ANN AOT which produces the overestimations in AIRS IR AOT over the cloud contaminated pixels, which are not surprising. On the other hand, though the correlation coefficients are slightly lower, the use of ANN-retrieved initial-guess increased magnitude of the AOTs over ocean on April 24, and thus the discontinuity between land and ocean AOTs is nearly disappeared. Moreover, it is obvious that the performance of  $z_{\text{dust}}$  retrieval was improved for both April 23 and 24 dust cases. Therefore, more accurate cloud screening method and sophisticated quality control of initial-guesses could reduce the unreasonable AOTs, and consequently improvement can be made with the use of more realistic initial-guess fields.

The retrieval capability of AOTs and two-dimensional effective heights for both day and night from IR hyperspectral sounder measurements, as demonstrated in this study, can surely enhance our ability to monitor the

evolutionary features of Asian dust. By the same token, our forecasting skill can be improved by incorporating dust information into forecasting models through the assimilation system. Future work can be directed at how those retrievals can be incorporated. Furthermore, from a long-term point of view, synergistic use of IR hyperspectral sounders aboard multi-platforms (such as IASI and CrIS), in combination with geostationary satellites, should bring in much more efficient tools for tracking down dust storms.

## References

- Ackerman, S. A. (1989), Using the radiative temperature difference at 3.7 and 11  $\mu\text{m}$  to tract dust outbreaks, *Remote Sens. Environ.*, 27(2), 129–133, doi:10.1016/0034-4257(89)90012-6.
- Ackerman, S. A. (1997), Remote sensing aerosols using satellite infrared observations, *J. Geophys. Res.*, 102(D14), 17069–17079, doi:10.1029/96jd03066.
- Aoki, T., T. Y. Tanaka, A. Uchiyama, M. Chiba, M. Mikami, S. Yabuki, and J. R. Key (2005), Sensitivity experiments of direct radiative forcing caused by mineral dust simulated with a chemical transport model, *J. Meteorol. Soc. Jpn.*, 83(0), 315–331, doi:10.2151/jmsj.83A.315.
- Aumann, H. H., et al. (2003), AIRS/AMSU/HSB on the Aqua mission: Design, science objectives, data products, and processing systems, *IEEE Geosci. Remote Sens. Lett.*, 41(2), 253–264, doi:10.1109/TGRS.2002.808356.
- Baldrige, A. M., S. J. Hook, C. I. Grove, and G. Rivera (2009), The ASTER spectral library version 2.0, *Remote Sens. Environ.*, 113(4), 711–715, doi:10.1016/j.rse.2008.11.007.
- Bishop, C. M. (1995), *Neural networks for pattern recognition*, 504 pp., Oxford University Press.
- Bloom, H. (2001), The Cross-Track Infrared Sounder (CrIS): A sensor for operational meteorological remote sensing, paper presented at International Geoscience and Remote Sensing Symposium (IGARSS), Optical Society of America, Sydney, Australia.

- Blumstein, D., et al. (2004), IASI instrument: Technical overview and measured performances, paper presented at Proc. SPIE, Denver, CO, USA.
- Borbás, E. E., R. O. Knuteson, S. W. Seemann, E. Weisz, L. Moy, and H.-L. Huang (2007), A high spectral resolution global land surface infrared emissivity database, paper presented at Joint 2007 EUMETSAT Meteorological Satellite Conference and the 15th Satellite Meteorology & Oceanography Conference of the American Meteorological Society, Amsterdam, The Netherlands, 24–28 September 2007.
- Brierley, P., and B. Batty (1999), Data mining with neural networks-an applied example in understanding electricity consumption patterns, *Knowledge Discovery and Data Mining*, 240–303.
- Brindley, H. E., and J. E. Russell (2006), Improving GERB scene identification using SEVIRI: Infrared dust detection strategy, *Remote Sens. Environ.*, *104*(4), 426–446.
- Chahine, M. T., et al. (2006), AIRS: Improving weather forecasting and providing new data on greenhouse gases, *Bull. Amer. Meteorol. Soc.*, *87*(7), 911–926, doi:10.1175/bams-87-7-911.
- Chou, M.-D., K.-T. Lee, S.-C. Tsay, and Q. Fu (1999), Parameterization for Cloud Longwave Scattering for Use in Atmospheric Models, *J. Climate*, *12*(1), 159–169, doi:10.1175/1520-0442(1999)012<0159:pfclsf>2.0.co;2.
- Claquin, T., M. Schulz, and Y. J. Balkanski (1999), Modeling the mineralogy of atmospheric dust sources, *J. Geophys. Res.*, *104*(D18), 22243–22256, doi:10.1029/1999jd900416.

- d'Almeida, G. A. (1989), Desert aerosol: characteristics and effects on climate, in *Palaeoclimatology and Paleometeorology: Modern and Past Patterns of Global Atmospheric Transport*, edited by M. Leinen and M. Sarnthein, pp. 311–338, Kluwer Academic Publishers, Dordrecht.
- Darmenov, A., and I. N. Sokolik (2005), Identifying the regional thermal-IR radiative signature of mineral dust with MODIS, *Geophys. Res. Lett.*, 32(16), L16803, doi:10.1029/2005gl023092.
- Dee, D. P., et al. (2011), The ERA-Interim reanalysis: configuration and performance of the data assimilation system, *Q. J. R. Meteorol. Soc.*, 137(656), 553–597, doi:10.1002/qj.828.
- DeSouza-Machado, S. G., et al. (2010), Infrared retrievals of dust using AIRS: Comparisons of optical depths and heights derived for a North African dust storm to other collocated EOS A-Train and surface observations, *J. Geophys. Res.*, 115(D15), D15201, doi:10.1029/2009jd012842.
- Dubovik, O., B. Holben, T. F. Eck, A. Smirnov, Y. J. Kaufman, M. D. King, D. Tanré, and I. Slutsker (2002), Variability of absorption and optical properties of key aerosol types observed in worldwide locations, *J. Atmos. Sci.*, 59(3), 590–608, doi:10.1175/1520-0469(2002)059<0590:VOAAOP>2.0.CO;2.
- Dudhia, J., D. Y. R. Grill, D. Guo, K. Hausen, and W. Manning (1998), *PSU/NCAR Mesoscale Modeling System Tutorial Class Notes (MM5 Modeling System Version 2)*.
- Freeman, J., and D. Skapura (1991), *Neural networks, algorithms, applications, and programming techniques*, Addison-Wesley Publishing Company,

Reading, Massachusetts, USA.

- Glumb, R. J., F. L. Williams, N. Funk, F. Chateaufneuf, A. Roney, and R. Allard (2003), Cross-track infrared sounder (CrIS) development status, paper presented at Proceedings of SPIE Int. Soc. Opt. Eng.
- Grell, G. A., J. Dudhia, and D. R. Stauffer (1994), A description of the fifth-generation Penn State/NCAR Mesoscale Model (MM5), Technical Note, 117 pp, NCAR.
- Gu, Y., W. I. Rose, and G. J. S. Bluth (2003), Retrieval of mass and sizes of particles in sandstorms using two MODIS IR bands: A case study of April 7, 2001 sandstorm in China, *Geophys. Res. Lett.*, *30*(15), 1805, doi:10.1029/2003gl017405.
- Hess, M., P. Koepke, and I. Schult (1998), Optical properties of aerosols and clouds: The software package OPAC, *Bull. Amer. Meteorol. Soc.*, *79*(5), 831–844, doi:10.1175/1520-0477(1998)079<0831:OPOAAC>2.0.CO;2.
- Holben, B. N., et al. (2001), An emerging ground-based aerosol climatology: Aerosol optical depth from AERONET, *J. Geophys. Res.*, *106*(D11), 12067–12097, doi:10.1029/2001JD900014.
- Hsu, N. C., J. R. Herman, and C. Weaver (2000), Determination of radiative forcing of Saharan dust using combined TOMS and ERBE data, *J. Geophys. Res.*, *105*(D16), 20649–20661, doi:10.1029/2000jd900150.
- Hsu, N. C., S. C. Tsay, M. D. King, and J. R. Herman (2004), Aerosol properties over bright-reflecting source regions, *IEEE Trans. Geosci. Remote Sensing*, *42*(3), 557–569, doi:10.1109/TGRS.2004.824067.

- Hudson, P. K., E. R. Gibson, M. A. Young, P. D. Kleiber, and V. H. Grassian (2008), Coupled infrared extinction and size distribution measurements for several clay components of mineral dust aerosol, *J. Geophys. Res.*, *113*(D1), D01201, doi:10.1029/2007JD008791.
- Jeong, G. Y. (2008), Bulk and single-particle mineralogy of Asian dust and a comparison with its source soils, *J. Geophys. Res.*, *113*(D2), D02208, doi:10.1029/2007jd008606.
- Köpke, P., M. Hess, I. Schult, and E. P. Shettle (1997), Global Aerosol Data Set, MPI Meteorologie Hamburg Report, 44 pp, Hamburg.
- Kim, D.-H., B.-J. Sohn, T. Nakajima, T. Takamura, T. Takemura, B.-C. Choi, and S.-C. Yoon (2004), Aerosol optical properties over east Asia determined from ground-based sky radiation measurements, *J. Geophys. Res.*, *109*(D2), D02209, doi:10.1029/2003jd003387.
- Kim, J. (2008), Transport routes and source regions of Asian dust observed in Korea during the past 40 years (1965–2004), *Atmos. Environ.*, *42*(19), 4778–4789, doi:10.1016/j.atmosenv.2008.01.040.
- Kim, S.-W., S.-C. Yoon, A. Jefferson, J.-G. Won, E. G. Dutton, J. A. Ogren, and T. L. Anderson (2004), Observation of enhanced water vapor in Asian dust layer and its effect on atmospheric radiative heating rates, *Geophys. Res. Lett.*, *31*(18), L18113, doi:10.1029/2004gl020024.
- Kleiber, P. D., V. H. Grassian, M. A. Young, and P. K. Hudson (2009), T-matrix studies of aerosol particle shape effects on IR resonance spectral line profiles and comparison with an experiment, *J. Geophys. Res.*, *114*(D21), D21209, doi:10.1029/2009JD012710.

- Krasnopolsky, V. M., and H. Schiller (2003), Some neural network applications in environmental sciences. Part I: forward and inverse problems in geophysical remote measurements, *Neural Networks*, *16*(3-4), 321–334, doi:10.1016/S0893-6080(03)00027-3.
- Kurosaki, Y., and M. Mikami (2003), Recent frequent dust events and their relation to surface wind in East Asia, *Geophys. Res. Lett.*, *30*(14), 1736, doi:10.1029/2003gl017261.
- Lee, E. H., and B. J. Sohn (2011), Recent increasing trend in dust frequency over Mongolia and Inner Mongolia regions and its association with climate and surface condition change, *Atmos. Environ.*, *45*(27), 4611–4616, doi:10.1016/j.atmosenv.2011.05.065.
- Lee, S.-S., B. J. Sohn, D.-S. Shin, H. Fukushima, and T. Nakajima (2002), Optical characteristics of the Asian dust aerosol from sky radiation measurements in Spring 1998, *Korean J. Atmos. Sci.*, *5*, 161–170.
- Lee, S.-S., and B. J. Sohn (2012), Nighttime AOT for Asian dusts MODIS IR measurements: An Artificial Neural Network approach, *J. Meteorol. Soc. Jpn.*, *90*(2), 163–177, doi:10.2151/jmsj.2012-201.
- Legrand, M., A. Plana-Fattori, and C. N'doumé (2001), Satellite detection of dust using the IR imagery of Meteosat 1. Infrared difference dust index, *J. Geophys. Res.*, *106*(D16), 18251–18274, doi:10.1029/2000jd900749.
- Levin, Z., J. H. Joseph, and Y. Mekler (1980), Properties of Sharav (Khamsin) dust-Comparison of optical and direct sampling data, *J. Atmos. Sci.*, *37*, 882–891.

- Levy, R. C., L. A. Remer, D. Tanr, Y. J. Kaufman, C. Ichoku, B. N. Holben, J. M. Livingston, P. B. Russell, and H. Maring (2003), Evaluation of the Moderate-Resolution Imaging Spectroradiometer (MODIS) retrievals of dust aerosol over the ocean during PRIDE, *J. Geophys. Res.*, *108*(D19), 8594, doi:10.1029/2002jd002460.
- Li, J., P. Zhang, T. J. Schmit, J. Schmetz, and W. P. Menzel (2007), Technical note: Quantitative monitoring of a Saharan dust event with SEVIRI on Meteosat-8, *Int. J. Remote Sens.*, *28*(10), 2181–2186, doi:10.1080/01431160600975337.
- Li, Z., et al. (2007), Preface to special section on East Asian Studies of Tropospheric Aerosols: An International Regional Experiment (EAST-AIRE), *J. Geophys. Res.*, *112*(d22), D22S00, doi:10.1029/2007JD008853.
- Mas, J. F., and J. J. Flores (2008), The application of artificial neural networks to the analysis of remotely sensed data, *Int. J. Remote Sens.*, *29*(3), 617–663, doi:10.1080/01431160701352154.
- Matricardi, M. (2005), The inclusion of aerosols and clouds in RTIASI, the ECMWF fast radiative transfer model for the infrared atmospheric sounding interferometer, 53 pp, European Centre for Medium-Range Weather Forecasts.
- Merchant, C. J., O. Embury, P. Le Borgne, and B. Bellec (2006), Saharan dust in nighttime thermal imagery: Detection and reduction of related biases in retrieved sea surface temperature, *Remote Sens. Environ.*, *104*(1), 15–30, doi:10.1016/j.rse.2006.03.00.

- Mikami, M., et al. (2006), Aeolian dust experiment on climate impact: An overview of Japan–China joint project ADEC, *Glob. Planet. Change*, 52(1), 142–172, doi:10.1016/j.gloplacha.2006.03.001.
- Myhre, G., A. Grini, J. M. Haywood, F. Stordal, B. Chatenet, D. Tanré, J. K. Sundet, and I. S. A. Isaksen (2003), Modeling the radiative impact of mineral dust during the Saharan Dust Experiment (SHADE) campaign, *J. Geophys. Res.*, 108(D18), 8579, doi:10.1029/2002jd002566.
- Nakajima, T., G. Tonna, R. Rao, P. Boi, Y. Kaufman, and B. Holben (1996), Use of sky brightness measurements from ground for remote sensing of particulate polydispersions, *Appl. Opt.*, 35(15), 2672–2686, doi:10.1364/AO.35.002672.
- Nakajima, T., et al. (2007), Overview of the Atmospheric Brown Cloud East Asian Regional Experiment 2005 and a study of the aerosol direct radiative forcing in east Asia, *J. Geophys. Res.*, 112(D24S91), D24S91, doi:10.1029/2007JD009009.
- Park, H.-S., and B. J. Sohn (2010), Recent trends in changes of vegetation over East Asia coupled with temperature and rainfall variations, *J. Geophys. Res.*, 115(D14), D14101, doi:10.1029/2009jd012752.
- Patterson, E. M., and D. A. Gillette (1977), Commonalities in measured size distributions for aerosols having a soil-derived component, *J. Geophys. Res.*, 82(15), 2074–2082, doi:10.1029/JC082i015p02074.
- Peyridieu, S., A. Chédin, D. Tanré, V. Capelle, C. Pierangelo, N. Lamquin, and R. Armante (2010), Saharan dust infrared optical depth and altitude retrieved from AIRS: a focus over North Atlantic – comparison to

- MODIS and CALIPSO, *Atmos. Chem. Phys.*, 10(4), 1953–1967, doi:10.5194/acp-10-1953-2010.
- Pierangelo, C., A. Chédin, S. Heilliette, N. Jacquinet-Husson, and R. Armante (2004), Dust altitude and infrared optical depth from AIRS, *Atmos. Chem. Phys.*, 4(7), 1813–1822, doi:10.5194/acp-4-1813-2004.
- Prata, A. J. (1989), Observations of volcanic ash clouds in the 10–12  $\mu\text{m}$  window using AVHRR/2 data, *Int. J. Remote Sens.*, 10(4-5), 751–761, doi:10.1080/01431168908903916.
- Ramanathan, V., and P. J. Crutzen (2003), New directions: Atmospheric brown "Clouds", *Atmos. Environ.*, 37, 4033–4035, doi:10.1016/S1352-2310(03)00536-3.
- Remer, L. A., et al. (2005), The MODIS aerosol algorithm, products, and validation, *J. Atmos. Sci.*, 62(4), 947–973, doi:10.1175/JAS3385.1.
- Reuter, D., J. Susskind, Andrew Pursch (1988) First-guess dependence of a physically based set of temperature–humidity retrievals from HIRS2/MSU data., *J. Atmos. Oceanic Technol.*, 5, 70–83, doi: [http://dx.doi.org/10.1175/1520-0426\(1988\)005<0070:FGDOAP>2.0.CO;2](http://dx.doi.org/10.1175/1520-0426(1988)005<0070:FGDOAP>2.0.CO;2)
- Rodgers, C. D. (1976), Retrieval of atmospheric temperature and composition from remote measurements of thermal radiation, *Rev. Geophys.*, 14(4), 609–624, doi:10.1029/RG014i004p00609.
- Rothman, L. S., et al. (2009), The HITRAN 2008 molecular spectroscopic database, *J. Quant. Spectrosc. Radiat. Transf.*, 110(9–10), 533–572,

doi:10.1016/j.jqsrt.2009.02.013.

- Rumelhart, D. E., J. L. McClelland, and P. D. P. R. Group (1986), *Parallel Distributed Processing. Explorations in the Microstructure of Cognition. Volume 1: Foundations*, 564 pp., MIT Press, Cambridge, Massachusetts.
- Salisbury, J. W., and D. M. D'Aria (1992), Emissivity of terrestrial materials in the 8–14  $\mu\text{m}$  atmospheric window, *Remote Sens. Environ.*, *42*(2), 83–106, doi:10.1016/0034-4257(92)90092-x.
- Salisbury, J. W., and D. M. D'Aria (1994), Emissivity of terrestrial materials in the 3–5  $\mu\text{m}$  atmospheric window, *Remote Sens. Environ.*, *47*(3), 345–361, doi:10.1016/0034-4257(94)90102-3.
- Saunders, R., M. Matricardi, and P. Brunel (1999), An improved fast radiative transfer model for assimilation of satellite radiance observations, *Q. J. Roy. Meteorol. Soc.*, *125*(556), 1407–1425, doi:10.1002/qj.1999.49712555615.
- Saunders, R., M. Matricardi, A. Geer, P. Rayer, O. Embury, and C. Merchant (2010), RTTOV-9 science and validation report, 75 pp, EUMETSAT, Darmstadt, Germany.
- Schütz, L. (1979), Sahara dust transport over the North Atlantic Ocean - Model calculations and measurements, in *Saharan Dust: Mobilization, Transport and Deposition*, edited by C. Morales, pp. 267–277, John Wiley & Sons, New York.
- Seemann, S. W., E. E. Borbas, R. O. Knuteson, G. R. Stephenson, and H. L. Huang (2008), Development of a global infrared land surface emissivity

- database for application to clear sky sounding retrievals from multispectral satellite radiance measurements, *J. Appl. Meteorol. Climatol.*, 47(1), 108–123, doi:doi:10.1175/2007jamc1590.1.
- Sherlock, V., and R. Saunders (1999), ISEM-6: Infrared surface emissivity model for RTTOV-6, 17 pp, Exeter, U. K.
- Shettle, E. P., and R. W. Fenn (1979), Models for the aerosols of the lower atmosphere and the effects of humidity variations on their optical properties, Rep., 94 pp, Hanscom Air Force Base, MA.
- Siméoni, D., C. Singer, and G. Chalon (1997), Infrared atmospheric sounding interferometer, *Acta Astronaut.*, 40(2–8), 113–118, doi:10.1016/S0094-5765(97)00098-2.
- Sinyuk, A., O. Torres, and O. Dubovik (2003), Combined use of satellite and surface observations to infer the imaginary part of refractive index of Saharan dust, *Geophys. Res. Lett.*, 30(2), 1081, doi:10.1029/2002GL016189.
- Sohn, B. J., H.-W. Chun, H.-J. Song, Y.-C. Noh, and S.-M. Lee, S. S. Lee, and Y. S. Chun (2013), Physical explanation of the weakened brightness temperature difference signal over the Yellow Sea during a dust event: case study for March 15-16, 2009, *Asia-Pac. J. Atmos. Sci.*, (accepted).
- Sokolik, I. N., O. B. Toon, and R. W. Bergstrom (1998), Modeling the radiative characteristics of airborne mineral aerosols at infrared wavelengths, *J. Geophys. Res.*, 103(D8), 8813–8826.
- Sokolik, I. N. (2002), The spectral radiative signature of wind-blown mineral

- dust: Implications for remote sensing in the thermal IR region, *Geophys. Res. Lett.*, 29(24), 2154, doi:10.1029/2002gl015910.
- Stephens, G. L., et al. (2002), The Cloudsat mission and the A-Train, *Bull. Amer. Meteorol. Soc.*, 83(12), 1771–1790, doi:10.1175/bams-83-12-1771.
- Torres, O., P. K. Bhartia, J. R. Herman, Z. Ahmad, and J. Gleason (1998), Derivation of aerosol properties from satellite measurements of backscattered ultraviolet radiation: Theoretical basis, *J. Geophys. Res.*, 103(D14), 17099–17110, doi:10.1029/98JD00900.
- Volz, F. E. (1972), Infrared refractive index of atmospheric aerosol substances, *Appl. Opt.*, 11(4), 755–759.
- Volz, F. E. (1973), Infrared optical constants of ammonium sulfate, Sahara dust, volcanic pumice, and flyash, *Appl. Opt.*, 12(3), 564–568.
- Wald, A. E., Y. J. Kaufman, D. Tanré, and B. C. Gao (1998), Daytime and nighttime detection of mineral dust over desert using infrared spectral contrast, *J. Geophys. Res.*, 103(D24), 32307–32313, doi:10.1029/98jd01454.
- Winker, D. M., W. H. Hunt, and M. J. McGill (2007), Initial performance assessment of CALIOP, *Geophys. Res. Lett.*, 34(19), L19803, doi:10.1029/2007gl030135.
- Yang, P., Q. Feng, G. Hong, G. W. Kattawar, W. J. Wiscombe, M. I. Mishchenko, O. Dubovik, I. Laszlo, and I. N. Sokolik (2007), Modeling of the scattering and radiative properties of nonspherical dust-like aerosols, *J. Aerosol Sci.*, 38(10), 995–1014,

doi:10.1016/j.jaerosci.2007.07.001.

- Yao, Z., J. Li, H.-J. Han, A. H. Huang, and B. J. Sohn (2012), Asian dust height and infrared optical depth retrievals from hyperspectral longwave infrared radiances, *J. Geophys. Res.*, (revised).
- Zhang, D. F., A. S. Zakey, X. J. Gao, F. Giorgi, and F. Solmon (2009), Simulation of dust aerosol and its regional feedbacks over East Asia using a regional climate model, *Atmos. Chem. Phys.*, 9(4), 1095–1110, doi:10.5194/acp-9-1095-2009.
- Zhang, P., N.-M. Lu, X.-Q. Hu, and C.-H. Dong (2006), Identification and physical retrieval of dust storm using three MODIS thermal IR channels, *Glob. Planet. Change*, 52(1-4), 197–206, doi:10.1016/j.gloplacha.2006.02.014.
- Zhao, T. X. P., S. Ackerman, and W. Guo (2010), Dust and smoke detection for multi-channel imagers, *Remote Sens.*, 2(10), 2347–2368, doi:10.3390/rs2102347.

## 국문초록

위성에서 관측한 적외 초분광 자료를 이용하여 동아시아 지역에서 발생, 이동하는 황사의 광학적 두께와 고도를 산출하였다. 본격적인 산출에 앞서 적외 초분광 자료로부터 얼마나 정확히 황사를 산출할 수 있는지 확인하기 위해 통계적 산출 방법 중 하나인 인공신경망 모델을 도입하여 AIRS의 단위픽셀 당 황사의 광학 두께와 고도를 산출하고 그 정확도를 알아보았다. 이를 위해 AIRS의 234개 채널에서 관측한 밝기 온도와 지표의 고도, 위성 천정각 정보를 입력 자료로 사용하였고 출력 자료는 황사의 550 nm에서의 광학 두께와 고도로 정의하였다. 인공신경망 모델은 통계적 방법으로서 훈련을 위한 자료가 필요한데 본 연구에서는 MODIS의 에어로솔 광학 두께와 CALIPSO의 고도자료를 입력자료와 짝을 지어 훈련 자료를 생산하였다. 훈련된 인공신경망 모델을 이용한 산출 결과를 MODIS, CALIPSO 에어로솔 자료와 비교해 보면 황사 광학두께의 상관계수는 0.84, 평균오차는 0.03이고 황사 고도의 상관계수는 0.79, 평균오차는 -0.01 km로서 적외 초분광 센서로부터 얻은 황사의 변수는 MODIS의 광학 두께와 CALIPSO의 고도에 비견할만하다고 할 수 있다.

인공신경망 모델로 확인한 적외 초분광 자료의 적용 가능성을 고려했을 때 물리적 산출 알고리즘 개발이 충분히 가능할 것으로 예상할 수 있다. 이를 위해 RTTOV라는 복사전달 모델을 사용하였고 새로운 황사 입자의 크기 분포와 굴절률, 지표면 방출율 자료를 이용하여 복사전달모델을 개선하였다. 개선한 복사전달모델을 기반으로 하는 1DVAR개념의 물리적 산출 알고리즘을 통해 황사의 광학 두께와 고도를 다양한 황사 사례에 대해 산출하였고 이를 MODIS 에어로솔 광학 두께, CALIPSO 황사 고도와 비교하였다. 이 때 적외창 영역과 CO<sub>2</sub> 흡수 영역의 11개 채널을 산출에 사용했다. 광학두께를 비교했을 때 0.72-0.96의 상관계수를 보여 산출된 광학 두께가 MODIS의 것과 잘 일치함을 알 수 있었다. 또한 고도 역시 CALIOP Level 1B 자료와 비교했을 때 합리적인 범위 내에서 산출되었고 특히 통계적 방법으로 부터 얻은 황사 자료를 초기값으로 사용했을 때 개선 효과가 있었다. 결과적으로 본 연구는 황사의 광학 두께와 고도가 적외 초분광 자료로부터 산출될 수 있으며 그 정확도는 MODIS와 CALIPSO의 에어로솔 자료와 비견될 수 있음을 보였다. 이러한 적외 초분광 자료로 얻는 황사 산출물은 넓은 AIRS 관측 구획 내 모든 픽셀에서 낮과 밤

제한 없이 산출할 수 있다는 장점이 있으며 이러한 적외 초분광 관측 자료의 장점은 보다 정확한 황사 감시 뿐 아니라 자료동화 과정을 통한 황사 예보 개선에 큰 역할을 할 수 있을 것으로 예상된다.

**주요어:** 황사, 적외 초분광, AIRS, MODIS, CALIPSO, 에어로솔 광학 두께, 황사 고도, 인공 신경망, 복사전달모델, RTTOV, 물리적 산출 알고리즘

**학번:** 2004-20598